# Microstructural Evolution of the Heat-affected Zone in 9%Cr Steels

Master Thesis of

Dilek Halici

Institute for Chemistry and Technology of Materials

and

Institute for Materials Science and Welding

*Supervisors*

Ao.Univ.-Prof. Dipl.-Ing. Dr.techn. Klaus Reichmann

Univ.-Prof. Dipl.-Ing. Dr. techn. Peter Mayr

Dipl.-Ing. Dr.techn. Bernhard Sonderegger

Graz University of Technology


Graz, 2011

## EIDESSTATTLICHE ERKLÄRUNG

Ich erkläre an Eides statt, dass ich die vorliegende Arbeit selbstständig verfasst, andere als die angegebenen Quellen/Hilfsmittel nicht benutzt, und die den benutzten Quellen wörtlich und inhaltlich entnommene Stellen als solche kenntlich gemacht habe.

Graz, am …… ……..

(Unterschrift)

## STATUTORY DECLARATION

I declare that I have authored this thesis independently, that I have not used other than the declared sources / resources, and that I have explicitly marked all material which has been quoted either literally or by content from the used sources.

…… ……..

date (signature)

# Acknowledgements

I would like to express my sincere thanks to my supervisors Professor Reichmann, Professor Mayr and Doctor Sonderegger for their encouragement.

Acknowledgement also goes to Professor Sommitsch at the Graz University of Technology, who has given me the opportunity to realise this present study.

I would like to thank Doctor Mendez-Martin for her support in logistical matters at the laboratory and in the metallographic investigations, Professor Mautner for his support in X-ray diffraction technique and discussing the results, and Professor Resel for his support and willingness to discuss X-ray diffraction technique, Magister Poetz, master of science, who made it possible to carry out scanning electron microscopy measurements at Varta Micro Innovation, Graz, Doctor Pein for her help with the software MATLAB and all of the colleagues at the IWS, and finally, I would like to thank my family and friends for their patience and support.

# Abstract

9-12% chromium steels with tempered martensitic microstructure are favored materials for creep exposed parts in fuel-fired thermal power plants. Welded components, which are characterised by the welding fusion line, and the heat-affected zone (HAZ), are used for the aforementioned facilities. The welding in turn causes an altering of the heat-affected zone, and this brings about a change in their mechanical properties. The objective of the present study therefore is to analyse the microstructural evolution of the heat-affected zone (HAZ) in these 9% chromium steels (modified 9Cr-1Mo and9Cr-3W-3Co-VNbBN) during thermal treatments.

By using in-situ X-ray diffraction (XRD) with synchrotron radiation at the Advanced Photon Source (APS) at Argonne National Laboratory, USA, conjunctively with a physical weld simulation, an investigation has been carried out on the phase transformations and on the precipitate's behaviour in the martensitic microstructure during thermal treatments. In addition to the mentioned techniques, other appropriate methods such as metallography characterisation and dilatometry have been employed. The use of optical microscopy (OM) allows analysis of the base material and the heat-affected zone's microstructure at varying temperatures. Additionally, a quenching dilatometer has been used to simulate these same thermal cycles as in the XRD, which enables to compare the results of these two methods. A closer look into the microstructure of the quenched samples has been carried out by metallographic investigations. A further suitable method involves scanning electron microscopy (SEM), which has been applied exclusively for the imaging of these base materials.

# Kurzfassung

9-12% Chromstähle mit einer angelassenen martensitischen Mikrostruktur sind bevorzugte Materialien für Anlagenteile brennstoffbeheizter thermischer Kraftwerke. Schweißen kann zu Gefügeveränderung innerhalb der Wärmeeinflusszone führen. Dies hat eine Verschlechterung der mechanischen Eigenschaften der Materialien zur Folge. Zum besseren Verständnis der Gefügeveränderung wird im Rahmen dieser Arbeit die mikrostrukturelle Entwicklung der Wärmeeinflusszone (WEZ) in 9% Chromstähle (modifizierter 9Cr-1Mo und9Cr3W3CoVNbBN) während der thermischen Behandlungen analysiert.

Der Einsatz von in-situ Röntgenstrukturanalyse mit energiereicher Synchrotronstrahlung, die im Argonne National Laboratory in den Vereinigten Staaten durchgeführt wurde, ermöglicht die Analyse der Phasentransformationen und des Ausscheidungsverhaltens in der martensitischen Mikrostruktur während der thermischen Behandlungen. Weiters wurden Charakterisierungsmethoden wie die Metallographie und Dilatometrie verwendet. Der Einsatz von Lichtmikroskopie (LM) ermöglicht die Analyse des Basismaterials im Anlieferungszustand und der Mikrostruktur der Wärmeeinflusszone bei unterschiedlichen Temperaturen. Um die die äquivalenten thermischen Zyklen zu simulieren, wie in der Röntgendiffraktometrie, wurde ein Abschreckdilatometer eingesetzt. Eine weitere angemessene Methode ist die Rasterelektronenmikroskopie (REM), die ausschließlich für die Charakterisierung des Basismaterials eingesetzt wurde.

# Contents

# List of Symbols and Abbreviations

## General

| | |
|---|---|
| A | indenter are ($mm^2$) |
| APS | Advanced Photon Source |
| BN | boron nitrides |
| COST | Cooperation for Science and Technology |
| d | arithmetical average of the indenter diagonals (mm) |
| EDS | Energy-dispersive X-ray spectroscopy |
| F | test load (N) |
| HV | Vickers hardness |
| IWS | Institute for Materials Science and Welding, TU Graz |
| LBII | Lichtenegger BloechII |
| LLNL | Lawrence Livermore National Laboratory |
| NIMS | National Institute for Materials Science, Tsukuba, Japan |
| OM | optical microscopy |
| SEM | scanning electron microscope |
| SIC | silicon carbide |
| TEM | transmission electron microscope |

## Phase transformations

| | |
|---|---|
| $A_{C1}$ | temperature of the onset of austenite formation on heating |
| $A_{C2}$ | Curie point |
| $A_{C3}$ | end temperature of the austenite formation |
| bcc | body-centred cubic |
| bct | body-centred tetragonal |
| fcc | face-centred cubic |
| $M_F$ | martensite finish temperature |
| $M_S$ | martensite start temperature |
| α | alpha-ferrite |
| γ | austenite |
| δ | delta ferrite |

**Welding**

| | |
|---|---|
| CGHAZ | coarse-grained heat-affected zone |
| FGHAZ | fine-grained heat-affected zone |
| HAZ | heat-affected zone |
| ICHAZ | Inter-critical heat-affected zone |
| PWHT | post-weld heat treatment |
| SCHAZ | subcritical zone |
| $t_{8/5}$ | cooling time between 800°C and 500°C |

**X-ray diffraction**

| | |
|---|---|
| Å | Ångstrom |
| FWHM | full width at half maximum |
| SRXRD | spatially-dissolved X-ray diffraction |
| TRXRD | time-resolved X-ray diffraction |

# 1 Introduction

Since rising $CO_2$ concentrations in the atmosphere have been noticed over a long time, the industrialised countries search for options to decrease the $CO_2$ emission. In order to follow this goal, many nations have agreed to the 1997 Kyoto protocol. Unfortunately, using $CO_2$-neutral energy sources such as renewable resources can only cover a small part of the world energy demand. One effective attempt to meet the demands is to increase the live stream efficiency in fossil fuel-fired thermal power plants, leading to lower fuel consumption and lower emissions. To achieve an improvement in the thermal efficiency the steam temperature and the pressure have to be increased [1]. The demand for higher temperatures relates to the exposability of materials with high creep resistance [2]. For achieving these requirements, tempered martensitic 9-12% chromium steels alloyed with molybdenum, tungsten, niobium and vanadium [2] are favored materials for creep exposed parts in thermal power plants [3]. 9-12% Cr steels fulfil advantageous properties such as high creep strength, low heat conductivity, resistance to steam oxidation. Another advantage of these steels is the low coefficient of thermal expansion [4]. The high creep strength is achieved by martensitic microstructure, which consists of high dislocation density, fine subgrain structure and finely distributed precipitates. Martensitic chromium steels reach their properties to the optimization of their chemical composition, heat treatment and microstructure [5]. Other steel grades cannot fulfil all requirements. Austenitic steels, for instance, feature poor thermal cycling behaviour and therefore application for thick walled parts in power plants is not advantageous. Moreover, 9-12% Cr steels have moderate costs in comparison to Ni- or Co-based superalloys or austenitic steels [6].

Currently, thermal power plants have efficiencies around 42% with steam temperatures of 600°C and pressures of 250-300 bar. In future the steam power plants should be capable to achieve steam temperatures up to 625-650°C and thermal efficiencies of around 45% [1]. Obviously for the fulfillment of all above mentioned requirements an advancement of martensitic 9-12% Cr steels is still necessary. Therefore, three promising candidates of materials for future power plants have been investigated in this work. Since most of the properties are related to the precipitation behaviour, the investigations focussed on precipitates. In the next section, the objective of the work is presented.

# 2 Objectives

The objective of the present study is to analyse the microstructure of the heat-affected zone (HAZ) in 9% martensitic chromium steels (modified 9Cr-1Mo and9Cr-3W-3Co-VNbBN) after the welding cycle and the post-weld heat treatment.

The main focus of the work is a qualitative analysis of the precipitates behavior in these 9% Cr steels, which are the most substantial creep strengthening contributors. The investigation of these phases cover the onset of formation and dissolution temperatures in 9% Cr steels. In order to understand these changes in the heat-affected zone during thermal treatments different modern techniques are used. By applying in-situ XRD with high synchrotron energy, the phase transformations during monitored thermal treatments with controlled heating and cooling rates of several steels have been observed.
Additionally, a quenching dilatometer has been used to simulate these same thermal cycles as in the XRD, which enables to compare the results of these two methods. A deeper look into the microstructure of the quenched samples has been carried out by metallographic investigations.

# 3 Literature Review

## 3.1 Microstructure of 9-12% Cr Steels

The specimens in this work have been quenched and tempered 9-12% Cr martensitic steels. For this reason, general aspects of the microstructure are reviewed in this section.

The carbon in these steels is responsible for the martensitic microstructure as well as the formation of carbides. The high chromium content is important for oxidation resistance [7]. Alloying elements such as Mo, W, V, Nb and N are added to these steels and enable the solid solution strengthening [4]. Boron is added to these steels to stabilise the martensitic microstructure, but the special task is to stabilise $M_{23}C_6$ precipitates at grain and lath boundaries. The enriched Boron reduces the coarsening rate of $M_{23}C_6$. In addition minor elements such as Si, S contribute to the oxidation resistance. Further details on the contributions of the alloying elements to the properties of the 9-12% Cr steels are reviewed in literature references [6,8,9].

The applied heat treatment of martensitic Cr steels consists of a normalising treatment in the austenite regime (temperature range between 1040°C-1100°C) and several tempering procedures. The applied tempering temperatures are between 650°C and 780°C, which depends on the required properties [4,9]. To dissolve the precipitates the normalising has been performed above the $Ac_1$ temperature to receive a fully austenitic microstructure [9].
Despite the correct choice of austenitising parameters delta ferrite can remain after austenisation. The presence of delta ferrite introduces a reduction of toughness, ductility, creep rupture strength, low cycle fatigue, creep fatigue strength and oxidation resistance [9]. Therefore the formation of delta ferrite should be prevented [10]. The solution to remove retained delta ferrite is a balanced alloying composition and an adequate heat treatment [9].

During cooling austenite transforms into martensite. Oversaturated martensite is the ideal starting microstructure for high creep resistance due to high dislocation density, narrow martensite laths and an uniform distribution of carbon atoms. The high Cr content in 9-12% Cr steels enables that air cooling is adequate for a complete martensitic transformation [11]. The high Cr content retards the diffusion of carbon and thereby phase formations such as α-ferrite, perlite and precipitation of carbides are prevented.

In Figure 1a, prior austenite grain boundaries are shown, which consist of packets and blocks. However the microstructure in this state consists of a martensitic lath boundary structure and a high density of dislocations. After austenisation a tempering treatment below the $A_{C1}$ temperature has been performed to avoid the reformation of austenite, to increase the ductility and strength at low temperatures [1,12]. The tempering leads to a lower dislocation density and formation of dislocation substructure.

The appearance of secondary phases during tempering depends on the chemical composition of the applied materials. Most prominent precipitates are $M_{23}C_6$ and/or MX, which are main contributors to the creep strength. In the as-received state (after austenitisation and tempering) the Cr-carbides $M_{23}C_6$ feature a size range of 50-100 nm. At elevated temperatures during service these precipitates tend to coarsening. The MX carbonitrides exhibit a size about 20-50 nm in the as-received condition and are smaller. MX also show a lower tendency to coarsening compared to $M_{23}C_6$. These precipitates are located within the sub grains and on sub boundaries. In Figure 1b, the microstructure in the as-received state is shown, which consists of prior austenite grain boundaries, martensitic lath structures, sub grain boundaries and finely dispersed precipitates [4].

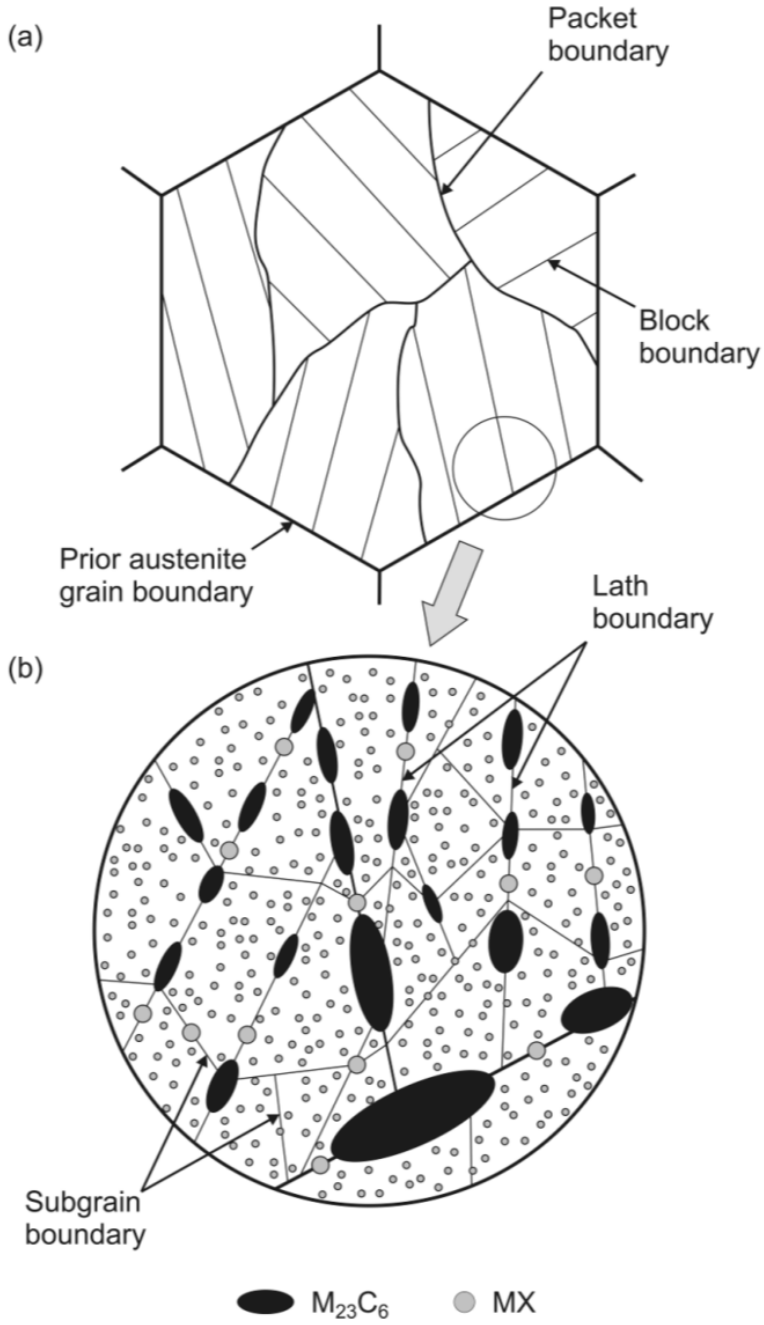


**Figure 1: Martensitic microstructure of 9-12% Cr steels [4].**

### 3.1.1 Precipitates in 9-12% Cr Steels

The 9-12% Cr steels owe their creep strength to the several types of precipitates, which can form either during the final normalising, heat treatment, or during subsequent creep [3].
In service, ageing of the microstructure can be observed, changing the microstructure. On this basis it should be pointed out that not all precipitates contribute to the creep strength to the same extent. Therefore, the next paragraphs summarise the properties of the most important precipitate types in 9-12% Cr steels. Figure 2 shows an overview of the most common precipitates in 9-12% martensitic Cr steels.

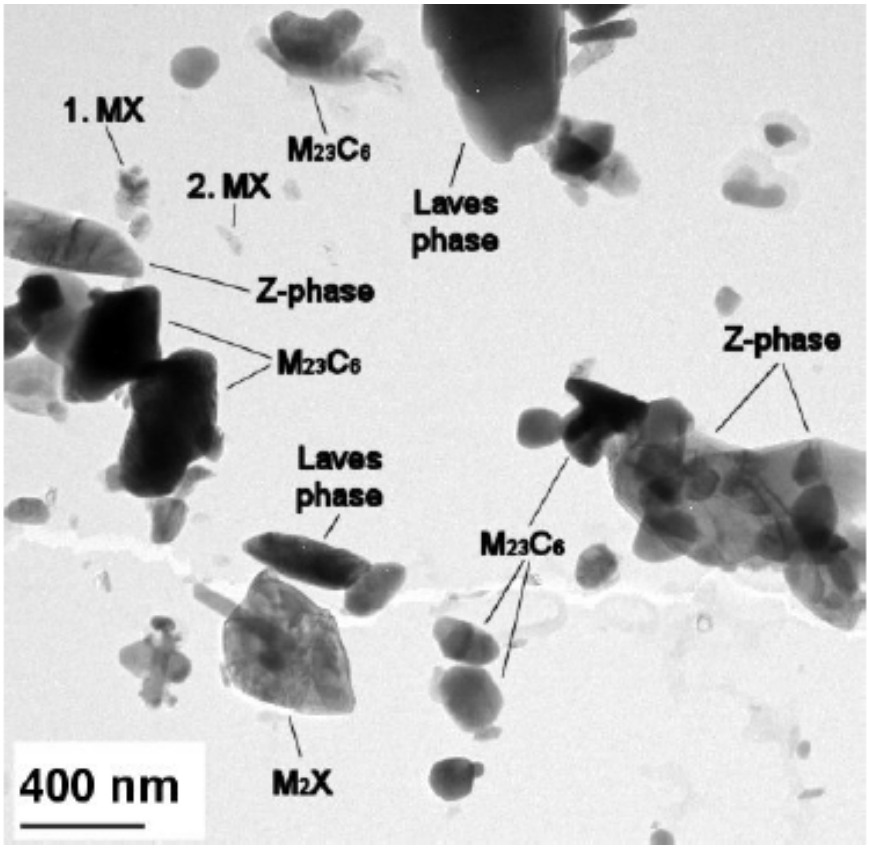


**Figure 2: Most common precipitates in 9-12%Cr steels [6].**

**$M_{23}C_6$**

$M_{23}C_6$ [(Fe, Cr, Mo, W)$_{23}C_6$] is a Cr-rich carbide. This secondary phase is observed in steels with high chromium content. $M_{23}C_6$ consists mainly of Cr and C, additional elements such as Fe, Mo, W and B also contribute. The chromium carbides form mainly along former austenite grain boundaries and martensite lath boundaries. $M_{23}C_6$ are feature a size of roughly 100 nm after tempering, after which it is the predominant precipitate [6,12]. During creep service it is observed that $M_{23}C_6$ tend to coarsen, which leads to a deterioration in creep resistance. However boron addition reduce the coarsening rate of the $M_{23}C_6$ with the formation of $M_{23}(C,B)_6$ [12]. The data on the crystal system is summarised in Table 1.

**$M_2X$**

$M_2X$ are observed in steels with high N content, where they are thermodynamically stable. It's known that MX and $M_2X$ precipitate form on the same sites and therefore it is supposed that $M_2X$ interfere with MX precipitation [3].

**MX**

MX in 9-12% Cr steels are V and Nb rich carbonitrides (Nb(C,N)) or (V(C,N)). The MX precipitates are small and densely distributed particles. Therefore they are one of the major contributors to the creep strength [3,13].

**Laves Phase**

The intermetallic Laves Phase of the type (Fe,Cr,Si)$_2$(Mo,W) is present in Mo or W steels. Precipitates of this phase also contain little amounts of Cr and Si. The Laves Phase features a hexagonal crystal structure. The nucleation of Laves Phase is not during tempering, but it forms during creep service exposure. These intermetallic precipitates, which are not stable at high temperatures, need long times for nucleation and growth. During growth it becomes larger than most other particles. Laves Phases with W nucleate faster, becoming smaller and more finely distributed compared to the Mo Laves phase [3]. At temperatures below 650°C, mainly Mo Laves Phase particles form, whereas W-based Laves Phase particles are prominent from 650°C up to about 750°C [12].

## Z Phase

*Original Z-phase (CrNbN)*

1950 Binder observed Z-phase in Nb alloyed austenitic steels. The Z-phase shows quick precipitation as small finely rod-like particles. In austenitic steels Z-phase dissolves as high as 1250°C, depending on the composition of the austenitic alloy [3].

*Modified Z-phase (Cr(V,Nb)N)*

In 1985, Andren et al. identified particles with Z-phase composition in 18Cr-12Ni-VNbN austenitic steel after isothermal annealing at 750°C up to 1170 h [3]. However half of the Nb content in these particles was replaced by V and thus showing a composition of Cr(V,Nb)N. In 1996, Strang and Vodarek showed that Z-phase in 11-12%CrMoVNbN steels cause breakdowns in long-term creep strength. Their investigations suggested that Z-phase precipitate appear as large particles, which induce the breakdown in creep strength. After long researches Strang and Vodarek found that the Z-phase dissolves the beneficial MX particles. The dissolution of MX particles causes a significant decrease in the creep strength. The new developed steels with 9-12% Cr content promised creep behaviour in short term tests, but after long exposure times the strength dropped dramatically. This behaviour motivated a number of publications of Danielsen and Hald, with the focus on the behaviour of Z Phase containing 9–12% Cr steels [3,13,14,15,16]. However the Z phase (Cr. V/Nb and N) is the most thermodynamically stable nitride in many 9-12% Cr steels [3,6,15].

Table 1 summarises phases prominent in 9-12% Cr steels, including their crystal systems and lattice parameters [6].

**Table 1: Crystal system and lattice parameter of the phases in 9-12% Cr steels [6].**

| Phase | Element | Crystal system | Point group | Lattice parameter [Å] | | |
|---|---|---|---|---|---|---|
| | | | | a | b | c |
| ***Matrix*** | | | | | | |
| Austenite | Fe, Cr | fcc | 225: Fm3m | 3.59 | 3.59 | 3.59 |
| Martensite | Fe, Cr, C | tetr. | 139: I4/mmm | 2.86 | 2.86 | 2.91 |
| Ferrite | Fe. Cr | bcc | 229:Im-3m | 2.87 | 2.87 | 2.87 |
| ***MX*** | | | | | | |
| VN | (V,Nb)(N,C) | fcc | 225: Fm3m | 4.139 | 4.139 | 4.139 |
| VC | (V,Nb)(N,C) | fcc | 225: Fm3m | 4.134 | 4.134 | 4.134 |
| NbC | (V,Nb)(N,C) | fcc | 225: Fm3m | 4.462 | 4.462 | 4.462 |
| $M_aX_b$ | | | | | | |
| $Cr_2N$ | | hex | | 4.760 | 4.760 | 4.444 |
| $Mo_2C$ | $Mo_2C$ | orthoromb. | 60:Pbcn | 4.735 | 6.025 | 5.21 |
| | | hex | 194:$P6_3/mmc$ | 3.011 | 3.011 | 4.771 |
| $M_6X$ | $(Fe,Cr,Mo)_6(C,N)$ | fcc | 227: Fd-3m | 11.062 | 11.062 | 11.062 |
| $M_7C_3$ | $(Fe,Cr,Mo)_7C$ | orthoromb. | 62: Pnma | 4.526 | 7.010 | 12.142 |
| $M_3C$ | $(Fe,Cr)_3C$ | orthoromb. | 62: Pnma | 5.089 | 6.743 | 4.524 |
| $M_{23}C_6$ | $(Fe,Cr,Mo,W)_{23}C_6$ | fcc | 225: Fm3m | 10.621 | 10.621 | 10.621 |
| ***Boride*** | | | | | | |
| $M_3B_2$ | $(Mo,Nb,Fe,Cr)_3B_2$ | tetr. | 127:P4/mbm | 5.7835 | 5.783 | 3.134 |
| BN | BN | trig. | 164 : P3m1 | 2.510 | 2.510 | 6.69 |
| | | hex | 187: P-6m2 | 2.504 | 2.504 | 6.661 |
| | | cub. | 216: F-43m | 3.615 | 3.615 | 3.615 |
| | | orthorhomb. | 69:Fmmm | 2.500 | 4.340 | 3.350 |
| ***Others*** | | | | | | |
| AlN | AlN | hex | 186: $P6_3/mc$ | 3.111 | 3.111 | 4.978 |
| Laves-Phase | $(Fe,Cr,Si)_2(Mo,W)$ | hex | 194: $P6_3/mmc$ | 4.745 | 4.745 | 7.734 |
| Mod. Z-Phase | Cr(Nb,V)N | tetr. | P4/nmn | 2.860 | 2.860 | 7.390 |
| Z-Phase | CrNbN | tetr. | P4/nmn | 3.040 | 3.040 | 7.390 |

### 3.1.2 Creep Strengthening

The high creep strength of 9-12% Cr steels finds its reasons in different mechanisms: solid solution hardening, precipitate or dispersion hardening, boundary and sub-boundary hardening and dislocation hardening [4]. Due to the high stability of the microstructure of the 9-12% Cr steels, the creep resistance remains high over a long exposure time. The microstructure stability during creep stress depends on [17]:

- relatively slow growth of $M_{23}C_6$
  Boron causes increasing creep strength due to stabilisation of $M_{23}C_6$. The boron atoms diffuse in the $M_{23}C_6$ carbides, resulting in the formation of $M_{23}(C,B)_6$.
- slow degradation of the dislocation density due to obstacles of finely distributed precipitates such as V(C,N)
- very low depletion of solid solution hardening elements (Mo,W) in the matrix
- retarded process of recovery (formation and growth of sub-grains) due to the stable $M_{23}C_6$ carbides

The most significant strengthening mechanism is the precipitate or dispersion hardening in 9-12% Cr steels [14]. Therefore, the next sub-chapter lays special attention on the precipitate or dispersion hardening.

#### 3.1.2.1 Precipitates or Dispersion Hardening

In our case, precipitation strengthening or dispersion strengthening is the most effective creep strengthening mechanism. By placing an obstacle to the movement of dislocations high creep strength is achieved. In comparison to solid solution strengthening (creation of strain fields) precipitates strengthening is related to the distribution of a secondary phase in the material [3]. To obtain precipitate hardening in creep resistant steels, Cr carbides such as $M_{23}C_6$, $M_6C$, $M_7C_3$, MX, $M_2X$, the intermetallic Laves phases $Fe_2(Mo,W)$ and the MN nitrides (V,Nb)N are required [10,11]. “M” denotes a metal atom, “X” denotes carbon and/or nitrogen [10]. In order to receive optimal precipitates properties (ideal particle size distribution and volume distribution) adequate heat treatment, starting microstructure and optimised chemical composition is necessary [17,18].

### 3.1.3 Heat-affected Zone

The welded components show that creep or creep fatigue damage appear during long exposure times in the heat-affected zone (HAZ) [19,20]. The heat-affected zone shows a large spectrum of different microstructures across this zone [19]. The HAZ microstructure is marked by the peak temperature of the welding cycle and the cooling rate (temperature range between 800 and 500°C) [19]. The heat-affected zone is divided into various subzones such as coarse-grain zone (CGHAZ), fine-grain zone (FGHAZ), intercritical zone (ICHAZ) and subcritical zone (SCHAZ) [21]. Figure 3 shows the sub-zones of the HAZ at the several peak temperatures.

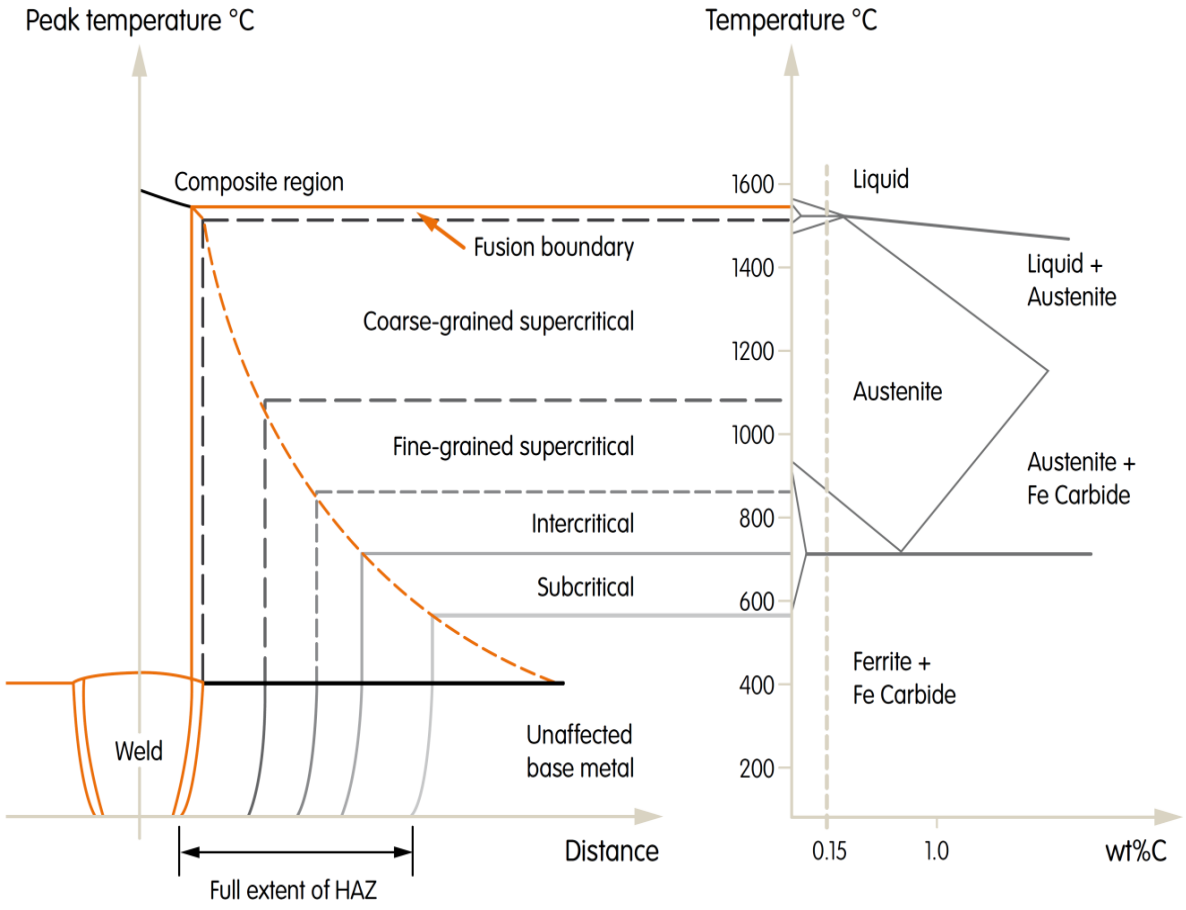


**Figure 3: Illustration of the sub-zones of the heat-affected zone [22].**

**Coarse-grained HAZ ($Tp>>A_{C3}$)**

Coarse-grained HAZ (CGHAZ) is the region closest to the fusion boundary. The CGHAZ, also referred to as "grain grow region", forms at temperatures above the $A_{C3}$ transformation temperature, where austenite is the stable matrix phase [23]. At these high temperatures precipitates stabilising the grain dissolve and thus grain growth is observed. During cooling, austenite transforms into martensite and CGHAZ features coarsened microstructure [21].

**Grain-refined zone ($Tp > A_{C3}$)**

At lower peak temperatures of about 1100°C (slightly above $A_{C3}$) the fine grain heat-affected zone (FGHAZ) forms. Due to the low peak temperature the precipitates are not completely dissolved and therefore austenite grain growth is hindered. However, precipitates such as $M_{23}C_6$ and Laves phase coarsen quicker in the fine-grained HAZ than in the base material during creep. After cooling to room temperature a martensitic microstructure is visible [21]. By applying longer exposure times and lower stress levels creep cracking is visible in the fine grained heat-affected zone of the weld treated component [24,25].

**Intercritical HAZ ($A_{C1} < T_P < A_{C3}$)**

The peak temperature of the inter-critical heat-affected zone (ICHAZ) is between the temperature range $A_{C1}$ and $A_{C3}$ [26]. New austenite grains form at austenite grain boundaries or martensite lath boundaries. During the welding cycle the untransformed tempered martensitic microstructure is tempered for a second time. After cooling the microstructure of the intercritical HAZ features newly formed martensite and tempered original microstructure. This region shows small grain sizes and lowest hardness values. The intercritical HAZ can also be related to Type IV cracking [21].

**Over-tempered region**

There is no microstructure altering if the peak temperature is below $A_{C1}$. In contrast to the post weld heat treated base material the original microstructure is locally tempered [21].

**Zone of unchanged base material**

Up to about 700°C there are no changes in the microstructure of the base material [21].

## 3.2 In-situ Observation of Phase Transformations with Synchrotron XRD

Conventional methods such as calorimetry and dilatometry are not capable to determine the phase transformations during welding directly [27]. However advanced in-situ X-ray diffraction with high synchrotron radiation technique enables the direct observation of microstructure evolution during welding in real time [28,29]. The high energy synchrotron radiation is more intense than conventional X-rays [30]. As a consequence, the method allows high brightness [31] and sub-mm resolution [30]. Synchrotron-based methods (spatially resolved (SRXRD) and time resolved (TRXRD) X-ray diffraction) have been developed by J.W. Elmer[1] at Lawrence Livermore National Laboratory (LLNL). The spatially resolved X-ray diffraction allows receiving diffraction patterns in real time during welding by means of a sub-mm sized X-ray beam. To acquire the X-ray diffraction pattern at discreet locations many scans start in the weld fusion zone, move across the heat-affected zone (HAZ) and the scanning ends in the base material. The received in-situ SRXRD pattern shows the phase transformations in the HAZ during steady state of the welding process. The experimental set-up of SRXRD to observe phase transformations during welding and the same setup is used for TRXRD, but placed on a stationary bar (Figure 4) [28].

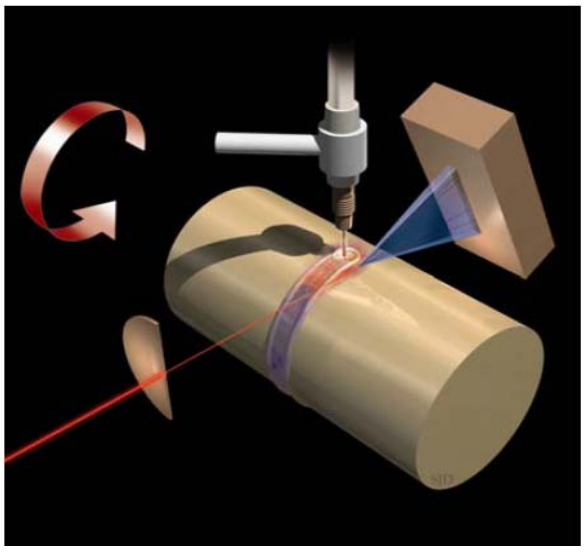

**Figure 4: Experimental procedure of SRXRD to observe phase transformations during welding by applying synchrotron radiation [21].**

[1]JOHN W. ELMER is Group Leader, Materials Joining, Materials Science and Technology Div., Lawrence Livermore National Laboratory, Livermore, Calif.

In-situ time resolved X-ray diffraction method (TRXRD) enables observing phase transformations during rapid weld heating and cooling conditions. Moreover, relative phase volume fractions can be determined from the obtained data and the peak widths as a function of the heating and cooling time are shown [21]. The real time XRD patterns are obtained for very short time intervals during welding and at a single location during a transient spot weld. In both techniques the beam size is sub-mm. TRXRD and SRXRD are both used for a large spectrum of materials such as alloys including steels and weld filler materials [28]. Both techniques suffer from a poor control of the welding procedure temperature and a direct measurement of the temperature is not practicable. Nevertheless, the coupling of XRD measurements with a thermal-fluids numerical simulation allows determining the temperatures of the microstructure. By applying this method, heating rates, cooling- and phase transformation temperatures can be identified. To control phase transformations under controlled conditions a special experimental set-up is developed (Figure 5). The XRD measurements are carried out during rapid heating and cooling of specimens by applying direct resistance heating and water cooled grips. Furthermore thermocouples are spot welded to the back side of the sample to monitor the temperatures of the material [21].

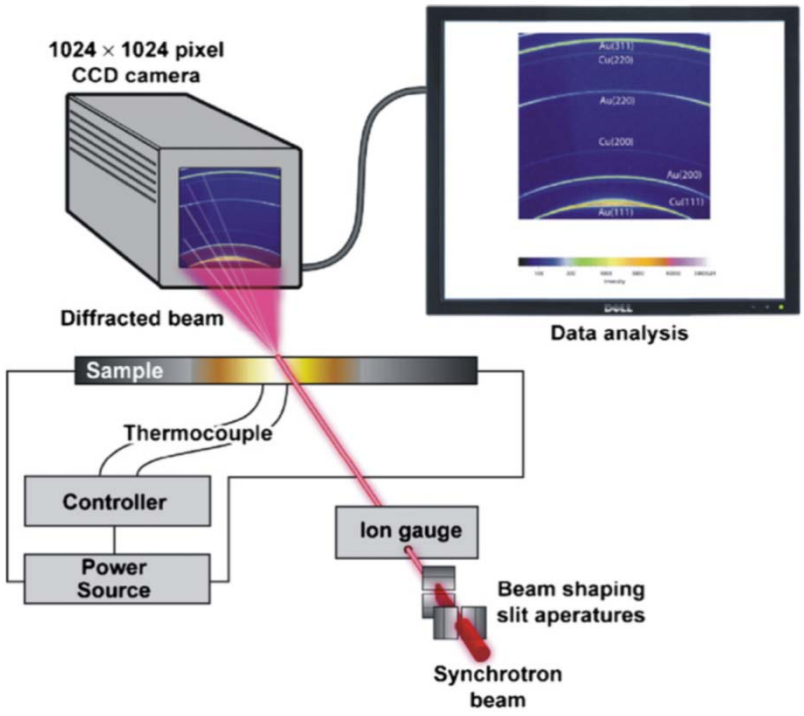


**Figure 5: Experimental set-up for in-situ observations of phase transformation under controlled heating and cooling conditions [21].**

# 4 Experimental Investigation

As shown in chapter 3.1.2 of the literature section, precipitates can induce excellent creep properties. One particular weak point in components is the heat-affected zone of weldments. Therefore the precipitates in the heat-affected zone microstructure have been analysed during thermal treatments. Moreover, the beginning of formation and dissolution temperatures of precipitates in 9 wt. % chromium martensitic steels are of special importance. The following presents the used 9% Cr steels and the methods of experimental research.

## 4.1 Investigated Materials

This chapter focuses on the specific materials involved, and the methods which have been applied in order to carry out the experiment for satisfactory results.

The examined test alloys are:

- modified 9Cr-1Mo steel designated as CB2A-Heat 145
- 9Cr-3W-3Co-VNbBN steel: Heat 1 (NPM1) and Heat 4 (NPM4)

CB2A-Heat 145 is a cast material and has been developed in cooperation with the European research activity COST (European Cooperation in Science and Technology) [21,32]. CB2A, which is part of a 100 kg test melt, was produced by voestalpine Foundry Linz, Austria. Further information on the development with the COST program can be found in the doctoral thesis "*Evolution of microstructure and mechanical properties of the heat-affected zone in B-containing 9% chromium steels",* by Mayr [21].

Heat 1 (NPM1) and Heat 4 (NPM4) are melts of 9Cr3W3CoVNb steel. The development of the two specific heats is based on analysis data from the National Institute for Materials Science (NIMS) in Japan. The 9Cr3W3CoVNb steels with controlled boron and nitrogen have been produced by the Institute for Materials Science and Welding (IWS) at the Graz University of Technology.

By using in-situ X-ray diffraction (XRD) with synchrotron radiation, conjunctively with a physical weld simulation, the precipitate's behaviour in the microstructure during thermal treatment has been analysed. An investigation has been carried out on the heat-affected zone's microstructure at varying temperatures by optical microscopy (OM). Further scanning electron microscopy (SEM) has been used exclusively for the evolution of these base materials.

### 4.1.1 CB2A-Heat 145

The cast material CB2A-Heat 145 has a high carbon content of 0.168 wt. %, boron (92 ppm) and nitrogen (160 ppm), as shown in Table 2. The chemical composition is given in weight percent.

**Table 2: Chemical composition of CB2A - Heat 145 in wt. % [21].**

| | | | | | | | |
|---|---|---|---|---|---|---|---|
| **CB2A (145)** | **C** | **Si** | **Mn** | **P** | **S** | **Al** | **Cr** |
| | 0.168 | 0.23 | 0.22 | 0.008 | 0.004 | 0.003 | 8.85 |
| | **Mo** | **Ni** | **V** | **Nb** | **B** | **N** | |
| | 1.54 | 0.18 | 0.29 | 0.057 | 0.0092 | 0.0160 | |

CB2A-Heat 145 has been heat treated and the parameters of the heat treatment are given in Table 3. Primarily, austenitising at 1100°C for 8 hours followed by air cooling has been performed, followed by a tempering at 730°C for 10 hours, which is followed by subsequent air cooling. The stress is then relieved at 730°C for 24 hours with subsequent air cooling. This final step is the so called post-weld heat treatment (PWHT). The main goal of the post-weld heat treatment is to reduce subsequent residual stress after welding, which is an improvement on the mechanical properties of the specimens [21].

**Table 3: Heat treatment conditions of CB2A - Heat 145 [21].**

| | **Heating rate [°C h$^{-1}$]** | **Temperature [°C]** | **Duration [h]** | **Cooling media** |
|---|---|---|---|---|
| **Austenitising** | not available | 1100 | 8 | air |
| **Tempering** | not available | 730 | 10 | air |
| **Stress relieving** | not available | 730 | 24 | air |

### 4.1.2 NPM1

Heat 1 (NPM1) is a 20 kg test melt with controlled addition of boron (120 ppm) and nitrogen (130 ppm) and has been produced by vacuum induction melting (VIM) at the Montanistic University of Leoben. For homogenisation the material has been forged to a final dimension of 50 x 50 mm and a length of 800 mm at Boehler Schmiedetechnik, Kapfenberg in Austria. The forging process was between the temperatures 1150°C (max.) and 950°C (min.). The forging has been followed by a quality heat treatment. The austenitising was at 1150°C for one hour and followed by air cooling. After the austenitising tempering at 770°C for four hours with subsequent air cooling has been performed [21]. In

Table 4 the chemical composition and in Table 5 the quality heat treatment parameters are summarised.

**Table 4: Chemical composition of NPM1 in wt. % [21].**

| | C | Si | Mn | P | S | Al | Cr | V |
|---|---|---|---|---|---|---|---|---|
| **Heat 1** | 0.074 | 0.29 | 0.44 | 0.009 | 0.004 | <0.005 | 9.26 | 0.21 |
| **(NPM1)** | **Nb** | **B** | **Co** | **W** | **N** | **Ni** | **Ti** | |
| | 0.056 | 0.0120 | 2.95 | 2.84 | 0.0130 | 0.06 | <0.005 | |

**Table 5: Quality heat treatment parameters of 9Cr-3W-3Co-VNbBN**

| | Heating rate [°C h$^{-1}$] | Temperature [°C] | Duration [h] | Cooling media |
|---|---|---|---|---|
| **Austenitising** | 250 | 1150 | 1 | air |
| **Tempering** | 250 | 770 | 4 | air |

### 4.1.3 NPM4

Heat 4 (NPM4) is a further development of Heat 1. NPM4, in contrast to NPM1, has low nitrogen content, ranging from 130 to 100 ppm. 100 kg of the NPM4 has been produced by vacuum induction melting, after which the ingot was rolled into 20 mm thick plates. As mentioned in the above sub-chapter, the quality heat treatment conditions for both 9Cr-3W-3Co-VNbBN steels are identical (see Table 5). The chemical composition of NPM4 is given in Table 6.

**Table 6: Chemical composition of NPM4 in wt. % [21].**

| | **C** | **Si** | **Mn** | **P** | **S** | **Al** | **Cr** |
|---|---|---|---|---|---|---|---|
| **Heat 4 (NPM4)** | 0.090 | 0.299 | 0.509 | 0.001 | 0.0030 | 0.0040 | 9.26 |
| | **V** | **Nb** | **B** | **Co** | **W** | **N** | |
| | 0.199 | 0.050 | 0.0114 | 2.880 | 2.92 | 0.01 | |

### 4.1.4 Sample Designation

In this work the microstructure has been investigated at different positions (see Figure 6) and the specimen designations used in this work are described in this chapter. The quality heat treatment is different for the used steels and the specific heat treatment parameters are described in the above chapters (4.1.1 and 4.1.2). All samples have been normalised and tempered before applying the welding cycle (Pos. 1). Position 1 is called the as-received condition of the base material. Position 2 is associated with the as-welded samples. The welding cycle is followed by a subsequent post-weld heat treatment (Pos. 3).

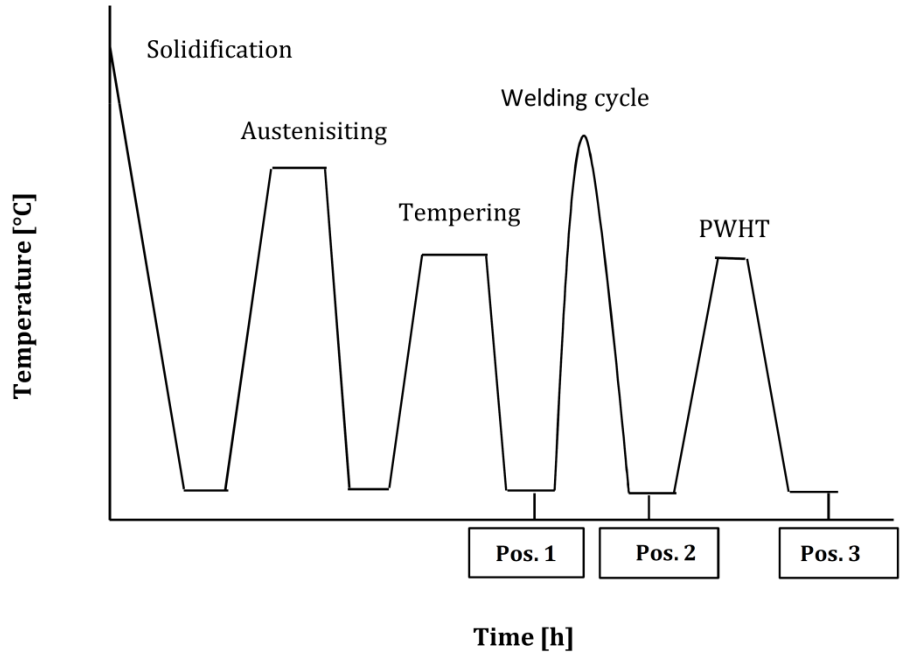


**Figure 6: Qualitative illustration of the heat treatment with characteristic positions.**

In Table 7 the specimen designations at different positions of the thermal treatments are summarised.

**Table 7: Specimen designations at different positions.**

| Positions | Specimen designation |
|---|---|
| **Pos.1** | **as-received condition is the so called base material** |
| **Pos.2** | **as-welded condition** |
| **Pos.3** | **after post-weld heat treatment** |

## 4.2 Dilatometry

Dilatometry allows measuring the thermal length variables as a function of temperature and enables the real time monitoring of the phase transformations in steels during various thermal cycles. During phase transformations the specific volume changes due to the change of the lattice structure and this enables to receive the transformation temperatures. To carry out the practical applications, a Bähr quenching dilatometer DIL-805A/D at the Graz University of Technology has been used. To investigate the microstructure of the 9% Cr steels, the samples have been quenched at several finite thermal cycle temperatures.

*Experimental set-up*

The experimental work with the quenching dilatometer (Bähr DIL-805A/D) focuses on the simulation of equal thermal cycles, as in XRD. The dilatometer samples which used are solids.

- NPM1 dilatometer samples have a length of 10 mm and an outer diameter of 4 mm.
- NPM4 specimens are characterised by a length of 10 mm and an outer diameter of 5 mm.
- CB2A specimen exhibits a length of at least 10 mm, but the CB2A has not cylindrical a shape in contrast to the dilatometer samples of 9Cr-3W-3Co-VNbBN steels, as shown in Figure 7. The reason is that there was no material left of CB2A.


**Figure 7: Applied dilatometer samples of the CB2A -Heat 145 material.**

First of all, the dilatometer samples have been placed between to quartz tubes and the measurements have been carried out in a vacuum chamber. The heating has been performed by an inductive coil, and the cooling through the injection of the inert gas argon. The measurement of temperature changes have been monitored by a spot-welded thermocouple at the centre of the specimen. The applied thermocouple is type S, and is able to withstand temperatures of up to 1600°C. A characteristic feature of this quenching dilatometer is the availability of high heating (max. 4000 K $min^{-1}$) and cooling rates (max. 2500 K $min^{-1}$) [33].

### 4.2.1 Applied Thermal Cycles

To analyse the microstructure of the three 9% chromium steels by means of metallography, the same thermal cycles in XRD have been simulated with the quenching dilatometer. The completed welding cycle of CB2A (A8) has been simulated by a constant heating rate of 100 K $s^{-1}$ to a peak temperature of 1300°C for 3s, followed by a subsequent cooling from 800°C to 500°C ($t_{8/5}$) in a cooling time of 43 s. Two of the completed welding cycles are followed by a post-weld heat treatment (PWHT). The post-weld heat treatment conditions are equal for the 9% Cr steels. During post-weld heat treatment, the specimens have been heated to 730°C and remain at this temperature for 2 hours. All experiments have been performed at heating- and cooling rate of 1.52 K $s^{-1}$. Table 8 shows a summary of the experimental parameters of the completed welding cycle's specimens and the post-weld heat treatment. The completed welding cycles with controlled heating and cooling rates have been marked by stars.

**Table 8: Summary of the experimental parameters of the completed welding cycles by using dilatometry.**

| Specimen | $T_P$ [°C] | Heating rate [K $s^{-1}$] | Holding time [s] | Cooling | Description |
|---|---|---|---|---|---|
| CB2A (A8.1300)* | 1300 | 100 | 3 | $t_{8/5}$ = 43 s | Welding cycle |
| CB2A (A8.730)* | 730 | 1.52 | 7200 | 1.52 K $s^{-1}$ | PWHT |
| CB2A (A2.1300)* | 1300 | 10 | 3 | 10 K $s^{-1}$ | Slow welding cycle |
| NPM1 (N2.1050)* | 1050 | 100 | 3 | $t_{8/5}$ = 43 s | Welding cycle |
| NPM1 (N2.730)* | 730 | 1.52 | 7200 | 1.52 K $s^{-1}$ | PWHT |
| NPM1 (N4.1300)* | 1300 | 10 | 3 | 10 K $s^{-1}$ | Slow welding cycle |
| NPM4 (M1.1300)* | 1300 | 10 | 2 | 10 K $s^{-1}$ | Slow welding cycle |

* complete welding cycles with controlled heating and cooling rates

The quenching temperatures for the welding cycles during heating are listed in Table 9 and for the subsequent PWHT after the welding cycle are shown in Table 10.

**Table 9: Quenching temperatures on heating of the welding cycles for all steels.**

| Specimen | Heating rate [K $s^{-1}$] | Quenching temperature on heating [°C] |
|---|---|---|
| CB2A (A8.925) | 100 | 925 |
| CB2A (A8.1000) | 100 | 1000 |
| CB2A (A8.1100) | 100 | 1100 |
| CB2A (A8.1165) | 100 | 1165 |
| CB2A (A8.1196) | 100 | 1196 |
| CB2A (A8.1250) | 100 | 1250 |
| CB2A (A8.1300) | 100 | 1300 |
| CB2A (A2.925) | 10 | 925 |
| CB2A (A2.1046) | 10 | 1046 |
| CB2A (A2.1076) | 10 | 1076 |
| CB2A (A2.1165) | 10 | 1165 |
| CB2A (A2.1196) | 10 | 1196 |
| CB2A (A2.1300) | 10 | 1300 |
| NPM1 (N2.950) | 100 | 950 |
| NPM1 (N2.980) | 100 | 980 |
| NPM1 (N2.1050) | 100 | 1050 |
| NPM1 (N4.1046) | 10 | 1046 |
| NPM1 (N4.1076) | 10 | 1076 |
| NPM1 (N4.1166) | 10 | 1166 |
| NPM1 (N4.1300) | 10 | 1300 |
| NPM4 (M1.900) | 10 | 900 |
| NPM4 (M1.1000) | 10 | 1000 |
| NPM4 (M1.1100) | 10 | 1100 |
| NPM4 (M1.1200) | 10 | 1200 |
| NPM4 (M1.1300) | 10 | 1300 |

Specimens without star marking are quenched, as shown in Table 9 and 10.

**Table 10: Quenching temperatures on heating of the PWHT after welding cycle for all steels.**

| Specimen | Heating rate [K $s^{-1}$] | Quenching temperature on heating [°C] |
|---|---|---|
| CB2A (A8.500) | 1.52 | 500 |
| CB2A (A8.550) | 1.52 | 550 |
| CB2A (A8.580) | 1.52 | 580 |
| CB2A (A8.600) | 1.52 | 600 |
| CB2A (A8.650) | 1.52 | 650 |
| CB2A (A8.700) | 1.52 | 700 |
| CB2A (A8.730) | 1.52 | 730 |
| NPM1 (N2.517) | 1.52 | 517 |
| NPM1 (N2.566) | 1.52 | 566 |
| NPM1 (N2.650) | 1.52 | 650 |
| NPM1 (N2.730) | 1.52 | 730 |

### 4.2.2 Study of Phase Transformation Temperatures

Based on dilatometry data, an investigation of the phase transformation temperatures $A_{C1}$, $A_{C2}$, $A_{C3}$, $M_S$ and $M_F$ during thermal treatments is possible. The relative expansion of the material is shown as a function of its temperature. To establish transformation points, a tangent has been applied to the linear part of the dilatometer curve, and when a deviation from the tangent by the linear part occurs, this is the transformation temperature.

## 4.3 Metallographic Investigations

### 4.3.1 Specimen Preparation

Evaluation of the material microstructure has been completed by metallography. The metallographic trial preparation sequence consists of cutting, embedding, planar grinding, polishing, etching, microscopic investigation and micro-hardness measurement.

The cutting of the specimens has been followed by its embedding in DuroFast (hot mounting epoxy resin) or in Multi Fast Black. The planar grinding has been performed by means of SIC paper and the Struers grinding machine. The process of grinding starts using silicon carbide (SiC) paper with grit 120 down to fine grit 4000. The samples have been washed with alcohol and distilled water between every grinding and every stage of the procedure.

The sample surface has been then prepared by polishing with 1 and 3 μm diamond suspension (Buehler METADI). The martensitic lath structure, the prior austenite grain boundaries, delta ferrite and precipitates have been revealed by using the colour etchant modified Lichtenegger-BloechII (LBII).

The polished samples have been immersed in the LBII solution for the duration of between 10 to 15 seconds, and the etched surfaces appear dark yellow to orange. A re-etching has been occasionally carried out for a better contrast of the microstructure. The modified LBII consists of 100 ml hot distilled water (50°C), 0.75 g ammonium hydrogen difluoride ($(NH_4)HF_2$) and 0.90 g potassium disulfide ($K_2S_2O_5$). Applying this etching procedure enables observation of the microstructure by different microscopy methods such as light optical microscopy and scanning electron microscopy.

### 4.3.2 Optical Microscopy

Qualitative characterisation of the microstructure with different magnifications has been performed using optical microscopy. The inverse light microscope used is from Carl Zeiss with ZEISS AxioVision Software and the Axio Observer Z1m is fully motorised [34]. For the analysis with microscopy the prepared samples have been etched with LBII (see 4.3.1).
The microstructural investigation by optical microscopy focus on precipitations in the martensitic lath structure and prior austenite grain boundaries. The metallographic investigation of different thermal cycles have been analysed the temperature range of the formation and dissolution of the precipitations of the chromium steels. For the analysing of precipitates, martensitic lath and delta ferrite at high magnifications (x625, x1250) have been used for the reason of the microstructure being extremely minute. Additionally, the resolution capability of this optical microscope with wavelength of 0.6656 µm is taken into consideration, as it is necessary to realise the limitations of its detection. Table 11 shows objective resolutions at various magnifications.

**Table 11: Objective resolution capability of the used optical microscope at the Institute for Materials Science and Welding.**

| Objective | Numerical aperture | Objective resolution [µm] |
|---|---|---|
| 100x/0.9HD | 0.9 | 0.37 |
| 50x/0.8HD | 0.8 | 0.42 |
| 20x/0.5HD | 0.5 | 0.67 |
| 10x/0.25HD | 0.25 | 1.33 |
| 5x/0.13HD DIC0 | 0.13 | 2.56 |
| 2.5x/0.06HD | 0.06 | 5.55 |

### 4.3.3 Scanning Electron Microscopy

One of the most universally used analysis techniques is that of scanning electron microscopy. The focus in this work is on secondary electron imaging of the examined base materials of the 9 wt. % Cr steels. The SEM measurements at room temperature have been carried out with a TESCAN VEGA 3 SEM at the Varta Micro Innovation in Graz. To produce the electrons, a heated tungsten cathode has been applied; the secondary electron detector is of Everhart-Thornley type. The SEM used has been distinguished by its accelerating voltage range of between 200 V to 30kV, a working distance of 5.00 mm – 15.00 mm and a resolution of 3 nm at 30 kV [35]. Figure 8 shows an SEM image of a CB2A sample at quenching temperature with the dilatometer at 580°C during post-weld heat treatment. Before the PWHT, a welding cycle has been performed with a peak temperature of 1300°C and heating rate 100 K $s^{-1}$.

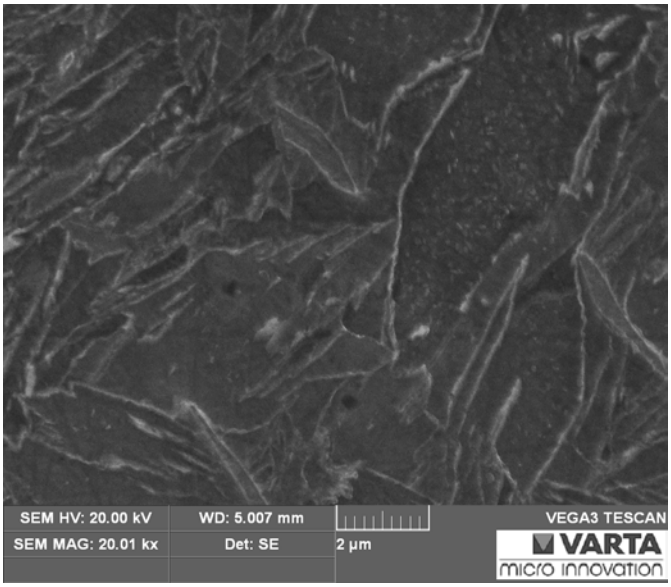


**Figure 8: SEM micrograph of CB2A heating up to 580°C after a welding process with heating rate of 100 K $s^{-1}$.**

### 4.3.4 Micro Hardness

In the present study, micro hardness measurements by applying the Vickers diamond indenter have been used to investigate the altered microstructure of thermally treated specimens. The martensitic laths and the delta ferrite have been analysed in particular.

$$HV = 0.102\frac{F}{A} = 0.102\frac{2F\,sin(136°\frac{1}{2})}{d^2} \approx 0{,}1891\frac{F}{d^2} \qquad (1.1\ [36])$$

| | |
|---|---|
| *HV* | *Vickers hardness* |
| *F* | *test load (N)* |
| *A* | *indenter area (mm²)* |
| *d* | *arithmetical average of the indenter diagonals (mm)* |

The remaining indenter is measured through the diagonals and the hardness is the average of the diagonals after the equation in 1.1 [36]. The measurement of hardness have been performed using a PAAR MHT-4 micro hardness tester with a video measuring system under a 0.01 kg (HV0.01) weight for 10 s. The experiments are carried out at room temperature.

## 4.4 Synchrotron in-situ X-ray Diffraction

In-situ X-ray diffraction with high energy synchrotron radiation is required to directly observe the phase transformations [37] in martensitic chromium steels during thermal cycles. The aim of this work to evaluate the data of the in-situ XRD experiments and to focus on the formation and dissolution of chromium carbide precipitations in martensitic chromium steels. The in-situ synchrotron X-ray diffraction measurements have been performed by Professor Peter Mayr at the Advanced Photon Source (APS) at Argonne National Laboratory, USA. Figure 9 shows an overview of the APS in Argonne. The X-ray diffraction measurements in welding cycles and their subsequent post weld heat treatments have been carried out under controlled heating and cooling conditions. The subsequent experimental conditions are taken from the doctoral thesis "Evolution of microstructure and mechanical properties of the heat-affected zone in B-containing 9% chromium steels" by Professor Peter Mayr [21].

**Figure 9: Overview of the Advanced Photon Source (APS) at Argonne National [21].**

### 4.4.1 Experimental Set-up

In-situ X-ray diffraction experiments have been carried out on the UNICAT beam line BM-33-C with a beam of 30keV energy originating from a ring current of 100 mA. The beam has been regulated through a dynamically bent Si crystal and collimator slits to a size of 1 mm wide by 0.25 mm high. The investigated samples for in-situ XRD have been investigated from the different base materials of the 9 wt. % chromium steels. The specimens are 100 mm long, 4.75 mm wide and 2 mm thick. The surface finish of the trials has been polished to 1 µm, where the X-ray beam impinges at an incidence angle of 5°. The smallest penetration depth of 23 µm is available through the 528 µm X-ray absorption length. In Figure 10 the experimental set-up process for the applied in-situ measurements is shown [21].

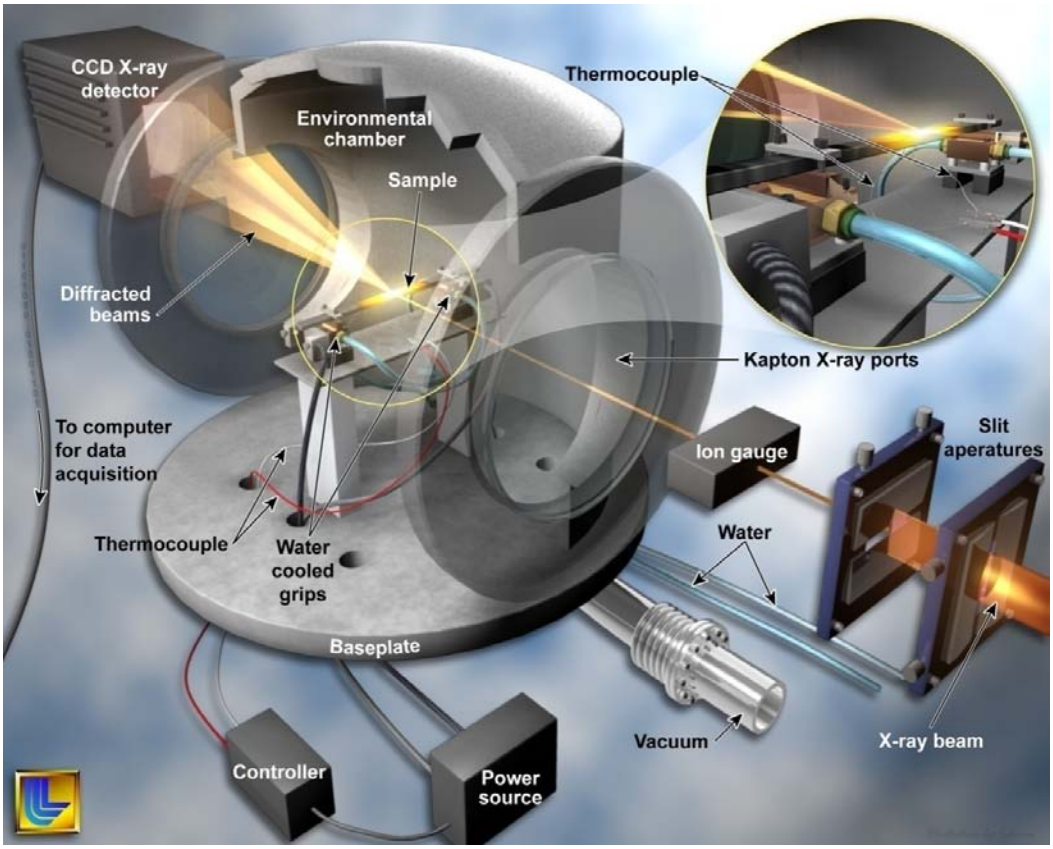


**Figure 10: Experimental set-up process for the synchrotron in-situ XRD measurements [21].**

The direct resistance heating of the trials has been used for fast heating, and water cooled grips for the rapid cooling of specimens. To control and register the temperature of the specimens, a type-S thermocouple (Pt/Pt-10% wt. % Rh) in use with a Eurotherm 818 temperature controller has been deployed. On the underside of the sample, the thermocouple has been spot welded directly below the X-Ray impingement point. To monitor the AC current passing through the sample, a Eurotherm 818 temperature controller, as well as an Eurotherm 425A power thyristor and a Trindl RT300 transformer have been deployed. With the heating power supply, temperatures of around 1400°C have been reached. Such temperatures can be achieved as the heating power supply is able to output 300A at 6V [21].

To avoid any oxidation and atmospheric contamination during the thermal cycles, the experiments have been performed inside a vacuum chamber. The collection of diffracted beams has been performed by a charge-coupled device (CCD) detector, which has been placed 330 mm behind the sample. The CCD detector has been produced by Roper Scientific (A99k401, RS/Photometrics). The specifications of the CCD detector are 6.1 x 6.1 $cm^2$ with an array of 1024x1024 pixels. The CCD detector stands at a distance of 60 μm from the sample. The registering of diffraction patterns has been applied on a scintillating screen, of which is connected to the CCD array detector by way of a fibre optic bundle [21].

The detector monitors X-ray data by integrating diffracted beams over a one second exposure. It takes two seconds for this to transfer to the computer. A complete diffraction pattern is available approximately every 3 seconds. The Fit-2D software allows the converting of diffraction rings (Debye arcs) in a diffraction plot, the diffracted beam intensity over d-spacing in Ångstrom [21].

### 4.4.2 Diffraction Pattern Analysis

The use of the FIT2D software enables the integration of X-ray diffraction rings to obtain a two dimensional diffraction pattern, with beam intensity over d-spacing. Detailed process information of this step is given in the doctoral thesis by Mayr [21]. This study presents a semi-automated curve fitting routine, which has been developed in Igor Pro® (created by S. S Babu), used to analyse phase transformations (version 5.0.) By applying this macro software the FWHM value, the d-spacing, integrated peak intensity and peak area of the fitted peak are obtained [21].

This method measures the integrated intensity of the peaks in diffraction pattern using Gaussian peak profile fitting functions. Igor Pro combines the time duration and temperature of the pattern with its corresponding diffraction data, as shown in Figure 11. Additionally, Igor pro calculates any variations of intensity in the synchrotron beam. The varying intensities of the peaks have been normalised with consideration to the measured maximum peak intensity in that pattern

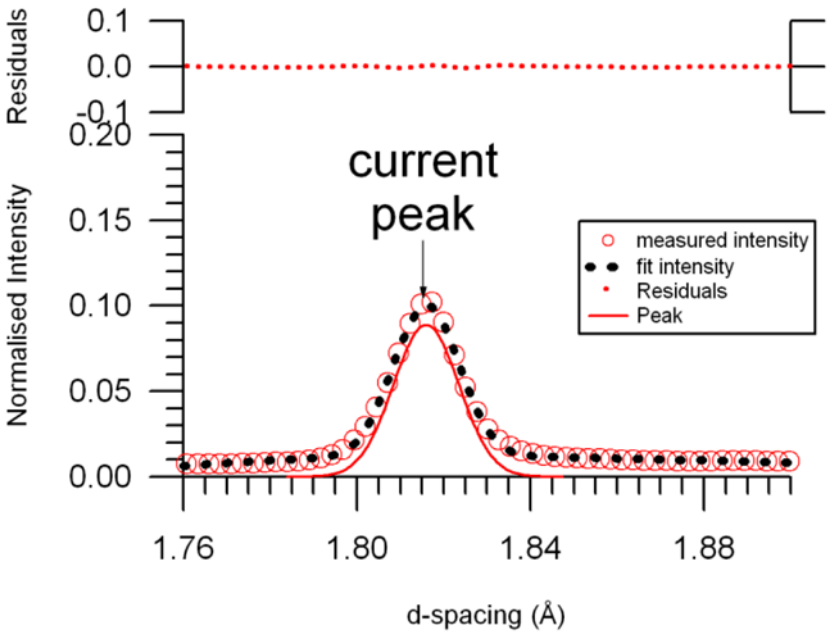


**Figure 11: Fitted peak intensity by gauss function using software Igor Pro [21].**

### 4.4.3 Applied Thermal Cycles

This section presents the applied thermal cycles with different peak temperatures by utilising in-situ XRD and dilatometry. The elaborated welding cycle in XRD is compared with the dilatometer created welding cycle of the CB2A (A8) specimen. Figure 12 shows a time-temperature function of CB2A – Heat 145, with a peak temperature of 1300°C heating rate (100 K $s^{-1}$) and cooling time of 43 s. All samples have been normalised and tempered before the welding cycle. These aforementioned welding cycles has been followed by a subsequent post-weld heat treatment, heating the specimen to 730°C, with a holding period of 2 hours and slow cooling to room temperature.

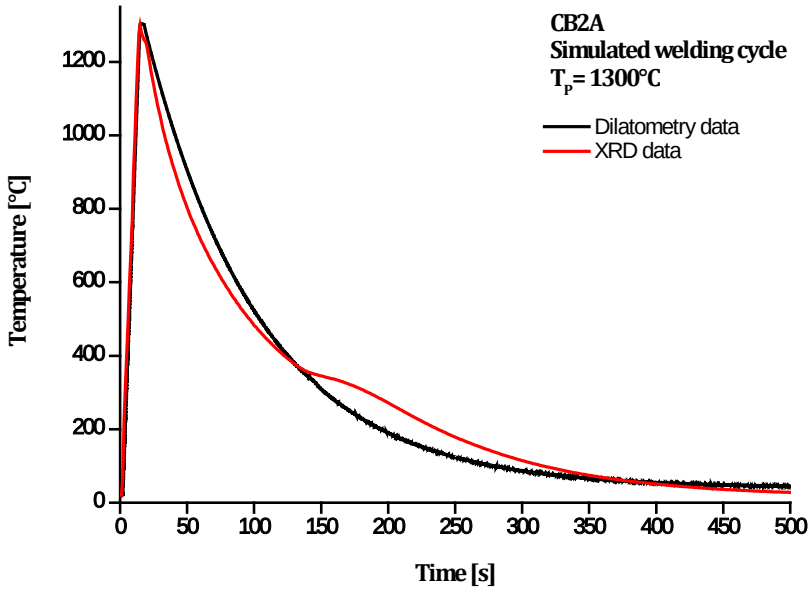


**Figure 12: Simulated welding cycles of CB2A by XRD and dilatometry.**

In Table 12 shows the experimental conditions of the in-situ XRD with synchrotron radiation for all steels summarised. On the whole, two types of welding cycles have been simulated; one with a fast heating rate of 100 K $s^{-1}$, and the other at 10 K $s^{-1}$. The welding cycles have been followed with a subsequent PWHT at a slow heating rate, after which a 730°C for two hours has been maintained.

**Table 12: Summary of experimental parameters of all performed thermal cycles by in-situ XRD.**

| Material | Peak temperature [°C] | Heating rate [K $s^{-1}$] | Holding time [s] | Cooling | Target |
|---|---|---|---|---|---|
| CB2A (A8.1300)* | 1300 | 100 | 3 | $t_{8/5}$ = 43 s | Welding cycle |
| CB2A (A8.730)* | 730 | slow | 7200 | - | PWHT |
| CB2A (A2.1300)* | 1300 | 10 | 3 | 10 K $s^{-1}$ | Slow welding cycle |
| NPM1 (N2.1050)* | 1050 | 100 | 3 | $t_{8/5}$ = 43 s | Welding cycle |
| NPM1 (N2.730)* | 730 | slow | 7200 | - | PWHT |
| NPM1 (N4.930)* | 930 | 100 | 3 | $t_{8/5}$ = 43 s | Welding cycle |
| NPM1 (N4.730)* | 730 | slow | 7200 | - | PWHT |
| NPM1 (N5.1300)* | 1300 | 10 | 3 | 10 K $s^{-1}$ | Slow welding cycle |
| NPM4 (M1.1300)* | 1300 | 10 | 2 | free cooling | |
| NPM4 (M1.1100)* | 1100 | 10 | 2 | free cooling | |

# 5 Results and Discussion

## 5.1 Base Material Characterisation

### 5.1.1 Optical Microscopy

As shown in Figure 13, the micrographs have been taken under the highest possible magnification to illustrate the precipitates' behaviour within the microstructure. The results obtained by light-optical microscopy prove that all three base materials (CB2A, NPM1, and NPM4) exhibit a somewhat similar microstructure consisting of tempered martensite after performing normalisation and tempering. Further optical micrographs of the base material are shown in the Appendix A. In the as-received state, the 9% Cr steels exhibit a martensite microstructure characterised by lath bundles. The morphology of the martensite microstructure depends on the carbon content. In steels with low carbon content less than 0.6 wt. %, the morphology of martensite can be lath-like; when carbon content is higher, it is plate-like martensite (>0.6 wt. %) [38,39]. Observation of the martensite laths using optical microscopy does not enable a detailed image as the laths are too small.
The microstructure reveals finely dispersed chromium carbide precipitates along the martensitic lath boundaries and the prior austenite grain boundaries. The resolution of the optical microscopy allows detection of large (>500 nm) $M_{23}C_6$ Cr carbide precipitates that occur only after tempering. The detection of precipitates with a small size (<500 nm) is not achievable with this optical microscope due to its low resolution.

Additionally, the micrographs show a homogenous microstructure coving the entire etched area. In all three of the chromium martensitic steels in the as-received state, δ-ferrite is not apparent. The qualitative analysis of residual austenite by means of an optical microscope is not a practical solution, as the microscopes resolution is too low. The in-situ XRD enables detection and identification of retained austenite. The resolution capability by using light-optical microscopy is described in the practical part of the work in this thesis.

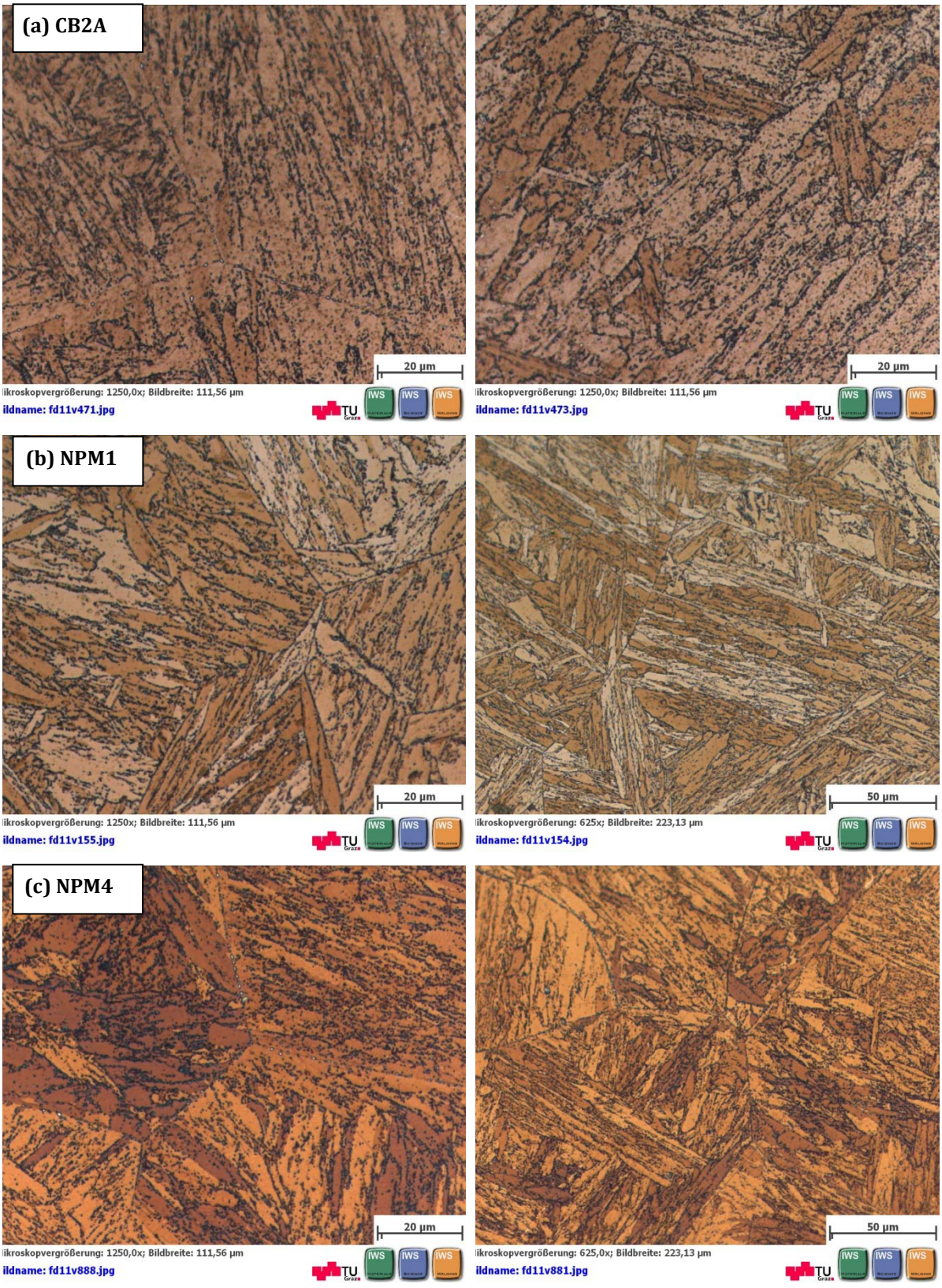


**Figure 13: Optical micrographs in the as-received state of (a) CB2A, (b) NPM1 and (c) NPM4 with precipitates along the martensitic lath boundaries and prior austenite grain boundaries.**

### 5.1.2 Scanning Electron Microscopy

The scanning electron micrographs (SEM) at a magnification of 5000 shows that the base material of all three steels consists of chromium carbide precipitates along the martensitic lath boundaries and the prior austenite grain boundaries (see Figure 14).

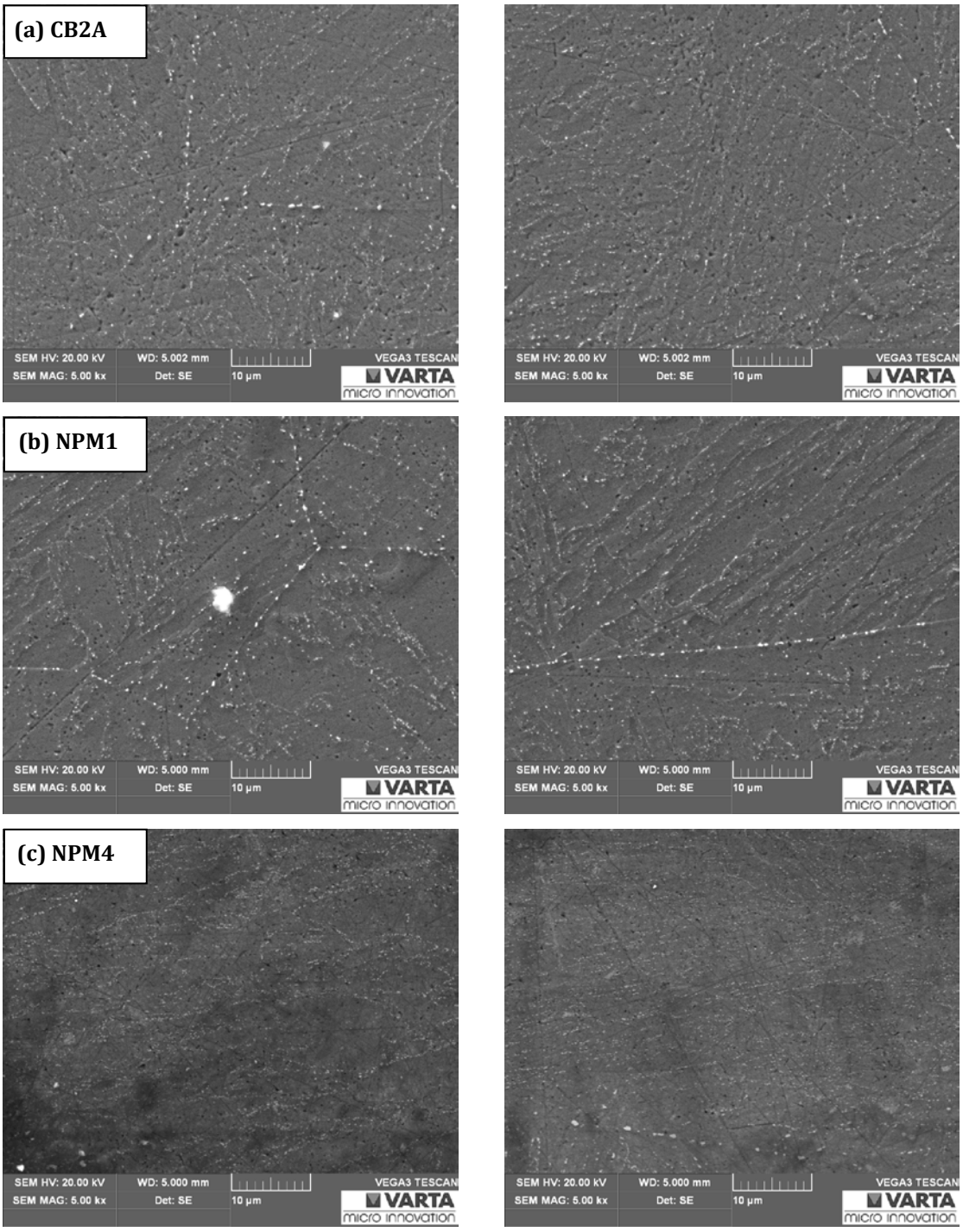


**Figure 14 : SEM micrographs in the as-received state of (a) CB2A, (b) NPM1 and (c) NPM4 with precipitates located at the martensitic lath boundaries and prior austenite grain boundaries.**

### 5.1.3 Micro Hardness

Micro hardness measurements have been performed to determine mechanical properties through various phases of the base material. The micro hardness tests have been carried out on austenite grain boundaries and martensitic lath boundaries. Further hardness micrographs of the base material in the as-received condition are shown in the Appendix. Modified 9Cr-1Mo (CB2A–Heat 145) in the as-received state with the tempered martensitic microstructure is characterised by an average hardness of 265 HV0.010. Furthermore, the result of the micro hardness in the forged base material of NPM1 has been measured around 269 HV0.010. The NPM4 base material equates to a hardness level of 287 HV0.010. Figure 15 details the Vickers hardness measurement values in the as-received state of CB2A, NPM1 and NPM4. The hardness measurements of various martensitic chromium steels show results within the same hardness range.

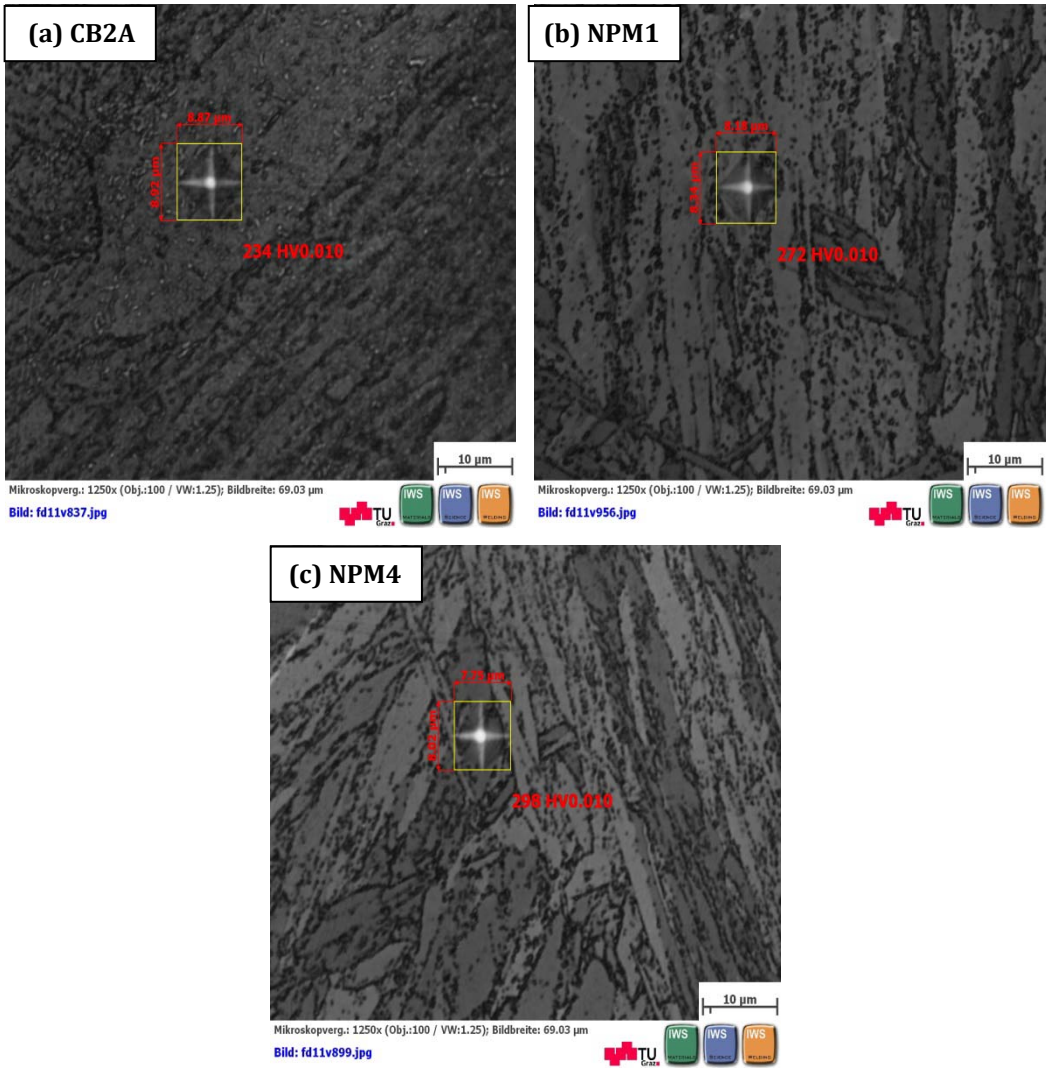


**Figure 15: Obtained hardness micrographs in the as-received condition of (a) CB2A, (b) NPM1 and (c) NPM4.**

### 5.1.4 In-situ Synchrotron X-ray Diffraction

In-situ X-ray diffraction with high energy synchrotron radiation enables the direct observation of phase transformations during thermal treatments. In this chapter, the qualitative evaluation of crystallographic phases of the 9% Cr steels of the matrix as well as the secondary phases has been calculated. In the following sub-chapters, the obtained XRD results of the matrix and precipitates analysis in the as-received state are summarised.

#### 5.1.4.1 Qualitative Study of the Matrix

The X-ray diffraction results obtained show that the predominant phases in the base material microstructure are body-centred cubic that demonstrate a tempered martensite. The bcc peaks are characterised by lattice planes α(200), α(211) and α(111).

X-Ray diffraction technique does not enable a clear distinction between ferrite (α and δ) and martensite, as the lattice constants of body-centred cubic, and body-centred tetragonal are too similar [40]. Based on the chemical composition and the obtained optical micrographs, it is clear that the material is tempered martensite.

The residual austenite with γ(111), γ(200), γ(220) peaks is identified as a further phase in certain base materials; some samples only show bcc peaks. Small amounts of austenite are caused by an incomplete martensite formation. The presence of $M_{23}C_6$ in all three base materials is verified by in-situ XRD, as described in the next sub-chapter.

Figure 16 shows the intensity of the phases' peaks as a function of d-spacing in Ångstrom on the example of NPM1 (a), bcc ferrite peaks, and (b), on a larger scale, the fcc peaks of residual austenite can be identified.

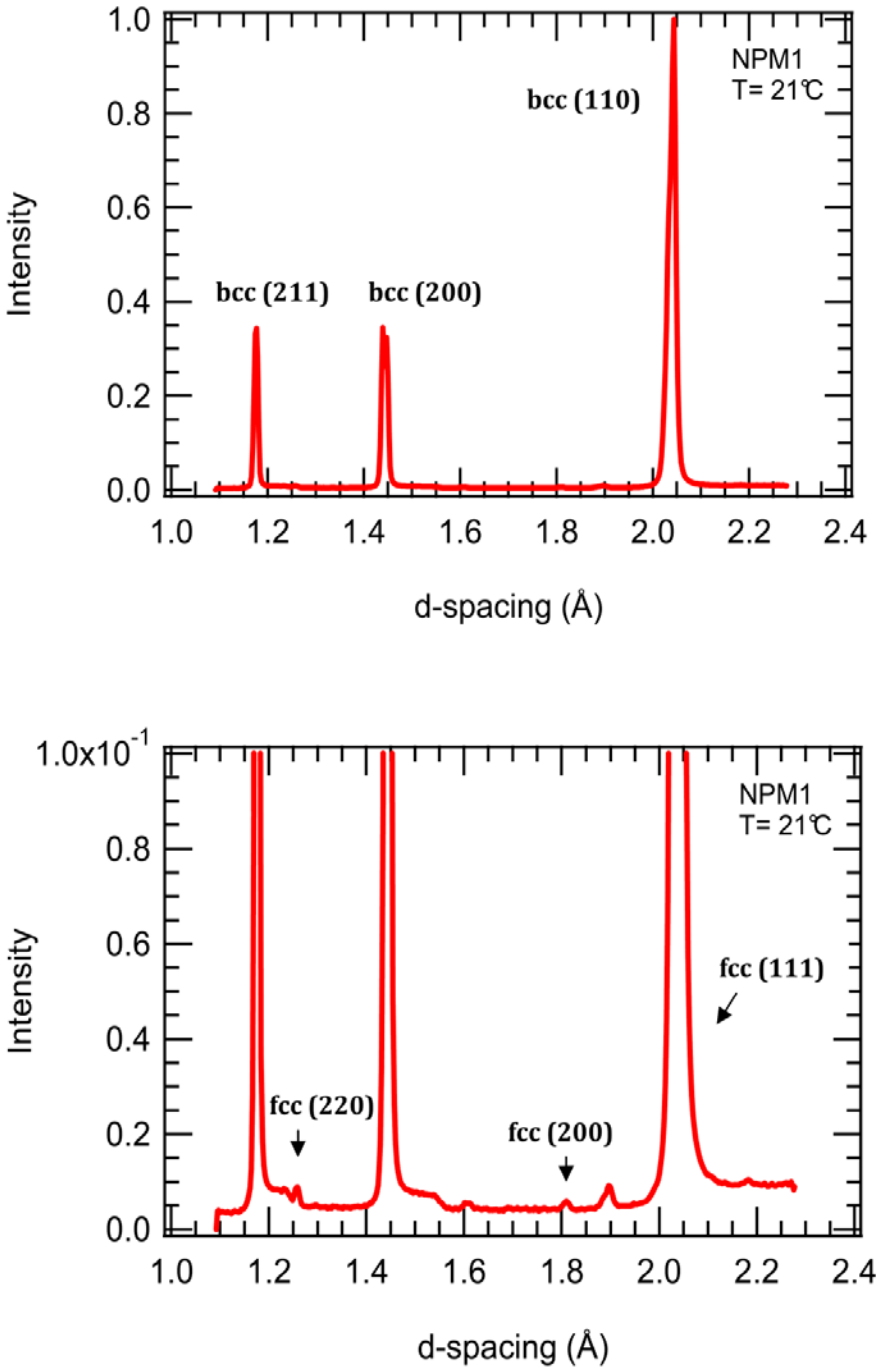


**Figure 16: The resulting X-ray diffraction pattern of the base material of NPM1; (a) the identified body-centred cubic ferrite peaks and (b) the face-centred cubic austenite peaks.**

### 5.1.4.2 Qualitative Analysis of the Secondary Phases

The as-welded CB2A material, (i.e. heating rate 100 K $s^{-1}$, cooling time of $t_{8/5}$= 43 s, $T_p$= 1300°C) has been followed by a post-weld heat treatment at 730°C for 2 hours. In Figure 17, a diffraction pattern of $Cr_{23}C_6$, in comparison to the XRD pattern of the post weld heat treated CB2A, are schematically illustrated.

During welding, with a peak temperature of 1300°C, the Cr carbides are not stable at high temperatures and dissolution occurs. The welding process has been followed by a post-weld heat treatment to the heat-affected zone. The PWHT heat treatment temperature is below $A_{C1}$ of the material which leads to a re-precipitation of oversaturated alloying elements in the solid solution.
To determine the secondary phases, it is therefore necessary to compare the XRD pattern of CB2A after PWHT to the $Cr_{23}C_6$ reference pattern. In Figure 17, the X-ray intensity is shown as a function of d-spacing in Ångstrom. After the post weld heat treatment, the face-centred cubic peaks are clearly revealed as Cr carbides $M_{23}C_6$. The identified peaks are fcc(660), fcc(711), fcc(622), fcc(440) and fcc(422) and their lattice planes are listed in Table 13 .

**Table 13: Summary of the obtained $M_{23}C_6$ precipitates inclusive the d-spacing and the lattice planes.**

| Precipitates | Crystal structure | d-spacing [Å] | Lattice plane |
|---|---|---|---|
| $M_{23}C_6$ | fcc | 1.27 | 6 6 0 |
| | fcc | 1.51 | 7 1 1 |
| | fcc | 1.64 | 6 2 2 |
| | fcc | 1.91 | 4 4 0 |
| | fcc | 2.22 | 4 2 2 |

All peaks, however, cannot be determined, as many $Cr_{23}C_6$ peaks overlap with the steel matrix. Based on the illustrated graph, the $Cr_{23}C_6$ reference pattern [41] is in good accordance with the post-weld heat treated CB2A XRD pattern. The $Cr_{23}C_6$ pattern, in contrast to the CB2A spectrum, is shifted systematically. This is as a result of several factors.

Firstly, the reference pattern belongs to $Cr_{23}C_6$, but the identified peaks pertain to the $M_{23}C_6$ [$(Fe, Cr, Mo, W)_{23}C_6$]. Secondly, $M_{23}C_6$ consists mainly of Cr and C with additional contribution from elements such as Fe, Mo, W and B. The Cr element may be substituted with elements such as Fe, Mo and W. The chemical composition of the 9% Cr steel CB2A doesn't contain tungsten even when the element Fe is present. It is known that iron exhibits a higher atom radius in comparison to the Cr and it is due to this fact that statistical shifting of the reference pattern can be observed.

A further variable is a fluctuation in the intensity of the $M_{23}C_6$, which differs from the reference pattern of $Cr_{23}C_6$. Nevertheless, an identification of the $M_{23}C_6$ peaks with the lattice planes is achievable. These differences in intensity could be attributed to the conditions of measurement, in particular the measuring variables. The obtained $Cr_{23}C_6$ is measured under equilibrium conditions and the variations in location and intensity are visible.

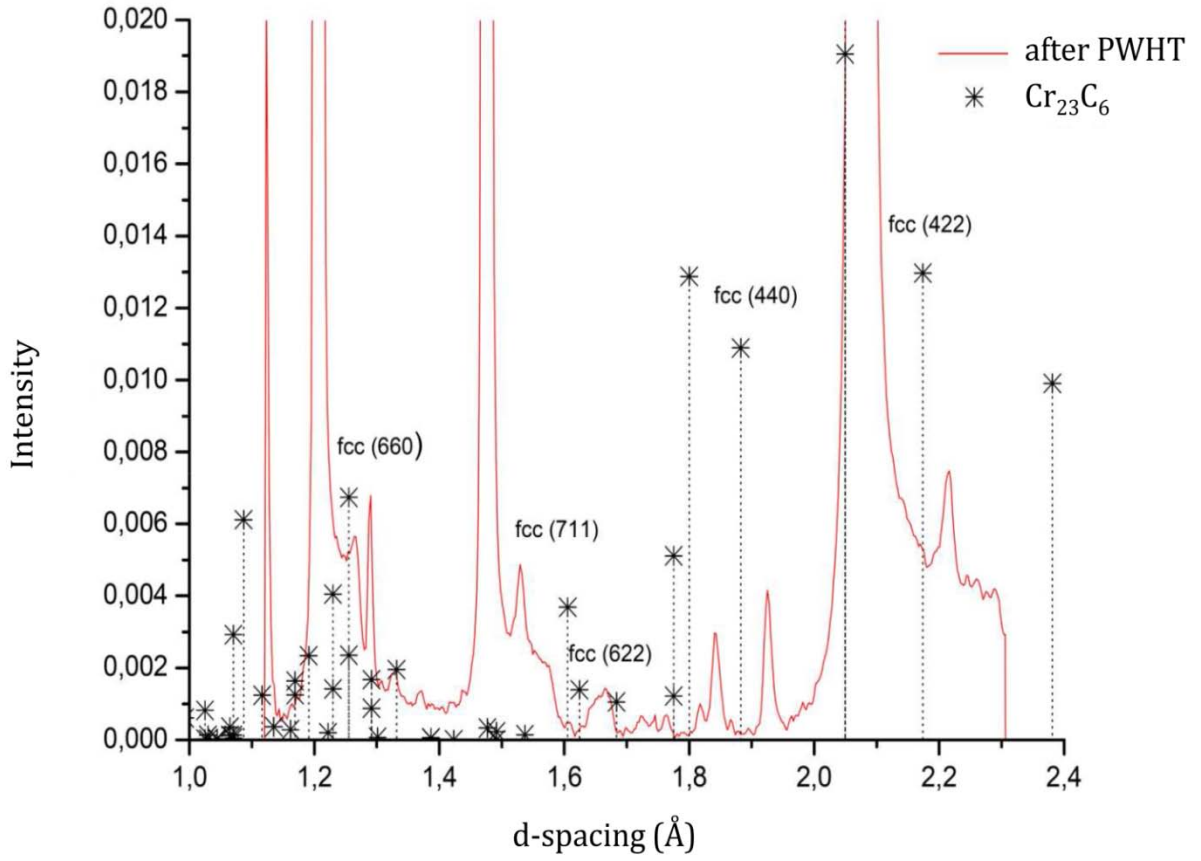


**Figure 17: The X-ray diffraction pattern of CB2A after PWHT, along with the reference pattern of $Cr_{23}C_6$.**

### 5.1.5 Conclusions

The base material of all three 9% Cr steels reveals a similar tempered martensitic microstructure with finely dispersed precipitates along the prior austenite grain boundaries and the martensite lath boundaries. The investigated base materials show a homogenous microstructure over the entire etched area. The presence of Cr rich $M_{23}C_6$ in the as-received state is verified by used modern techniques such as light-optical microscopy, scanning electron microscopy and in-situ X-ray diffraction with synchrotron radiation.

The obtained in-situ XRD patterns show that the detected face-centred cubic peaks are assigned to the $M_{23}C_6$ Cr carbides, which occurs after tempering. The identified $M_{23}C_6$ peaks are fcc(660), fcc(711), fcc(622), fcc(440) and fcc(422). Furthermore, the use of optical microscopy also allows the detection of precipitates, however with the known resolution, it is obvious that the detected large precipitates (>500 nm) after tempering are chromium carbides $M_{23}C_6$. Using optical microscopy, it is difficult to describe the morphology and density number of the $M_{23}C_6$ in the steels. In the as-received condition, the $M_{23}C_6$ are located at the prior austenite grain boundaries and martensite lath boundaries.
The fine dispersion of $M_{23}C_6$ in the base materials of the three 9% Cr steels are also verified by means of scanning electron microscopy. Additionally, the micro hardness of the base materials are investigated, and all three low carbon steels show results in the same range.

In Mayr's publication [42], by means of electron microscopy, the NPM1 base materials consist not only of $M_{23}C_6$, but also the MX (V,Nb)(N,C) carbonitrides. The detected MX exhibits a diameter larger than 100 nm and the carbides present a diameter between 150 and 250 nm. Further SEM and EDS indicate that Heat 1 (NPM1) has small BN (<1 µm) (see Figure 18), but in Heat 4 (NPM4) no BN could be detected [42].

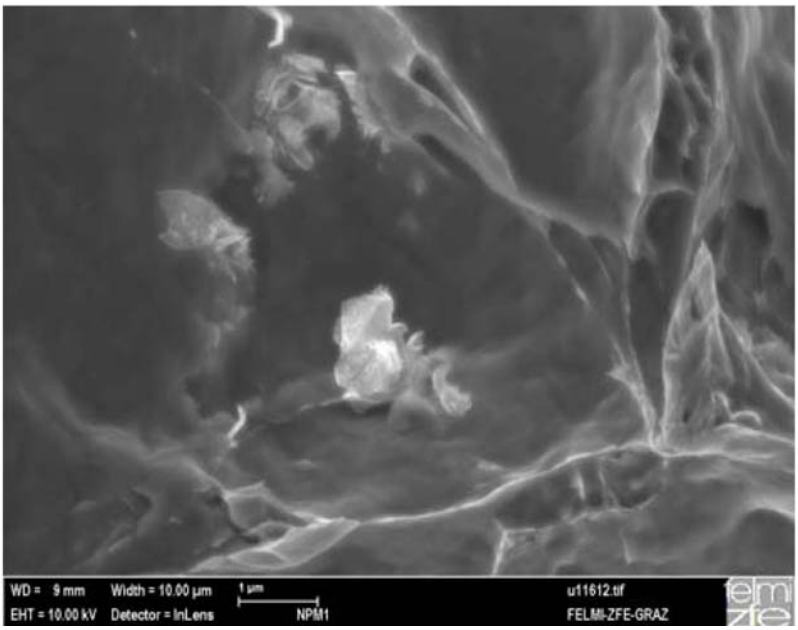


**Figure 18: EDS micrograph of NPM1 base material with small (<1µm) BN [42].**

If the modified 9Cr-1Mo steel and the 9Cr-3W-3Co-VNbBN steels would have the same tempering conditions, the conclusion that high carbon content allowing high Cr carbide formation could be verified. When the tempering temperature as well as time is different, it is difficult to verify the conclusion. Further analysis of the precipitates population using optical microscopy is very difficult.

The obtained results of in-situ X-ray diffraction show that little amount of austenite remains in the microstructure of the three base materials. With the use of optical microscopy however, this could not be verified. According to the doctoral thesis from Mayr, the 1% low volume fraction of austenite in the CB2A base material is shown [21]. The volume fraction of austenite depends on its composition, austenitising temperature, quenching rate, final quenching temperature and stress state. A high amount of retained austenite can lead to lower elastic limits, reduced hardness, a lower high cycle fatigue life and dimensional instability [43]. The presence of delta ferrite in the as-received condition cannot be detected in either method, as delta ferrite is only observed by heating the materials to higher temperatures.

## 5.2 Microstructure of the Heat-affected Zone

The investigation of the heat-affected zone (HAZ) microstructure during thermal treatments is important for the understanding of the material's properties. Phase transformations of the three 9% Cr steels during welding have been analysed by means of in-situ X-ray diffraction and dilatometry. The altered heat-affected zone microstructure has been investigated by optical microscopy. In addition, the micro hardness measurements have been carried out on the steels at room temperature. The results of micro hardness are shown as average measurements. This chapter aims to show representative X-ray diffraction patterns and optical micrographs of quenched samples. Special attention has been paid to the dissolution of precipitates during welding and their formation during post-weld heat treatment.

The following overview outlines the used technical methods for the investigation of the HAZ microstructure:

- dilatometry: determination of phase transformation temperatures on heating and cooling during completed thermal welding cycles
- optical microscopy: investigation into the martensitic microstructure, prior austenite grain boundaries, delta ferrite morphology and Cr carbides (in particular the formation and dissolution) during thermal welding cycles and their subsequent PWHT
- micro hardness: determination of the micro hardness on quenched samples at several temperatures of the thermal cycles in the as-welded state and after subsequent PWHT
- in-situ X-ray diffraction with synchrotron radiation: investigation into the phase transformation temperatures of the matrix and secondary phases (formation and dissolution temperatures of the precipitates)

## 5.2.1 Dilatometry

### 5.2.1.1 Phase Transformation Behaviour

The phase transformation behaviors of CB2A, NPM1 and NPM4 have been evaluated by means of dilatometry. To visualise the microstructure of the heat-affected zone (HAZ), it is necessary to investigate the start and end temperatures of the phase transformations. The following sub-chapter documents the obtained phase transformation temperatures of the simulated welding cycles in the three 9% Cr steels. By dilatometry, the equal welding cycles (as in XRD) have been simulated, as well as the equal peak temperatures, heating and cooling rates.

**CB2A-Heat 145**

A typical result of the welding cycle in the material CB2A with a peak temperature at 1300°C, a heating rate 100 K $s^{-1}$ and a cooling time of 43 s between 800°C and 500°C is revealed. The relative expansion [%] of the sample against temperature is shown in Figure 19. The dilatometer curve is divided into heating and cooling parts. The heating dilatometry curve provides information about $A_{C1}$, $A_{C2}$ and $A_{C3}$. As the material cools, the phase transformation temperatures of $M_S$ and $M_F$ can be determined. The martensite start temperature means that face-centred cubic austenite starts to transform into body-centred tetragonal martensite and it is completed at the martensite's final temperature.

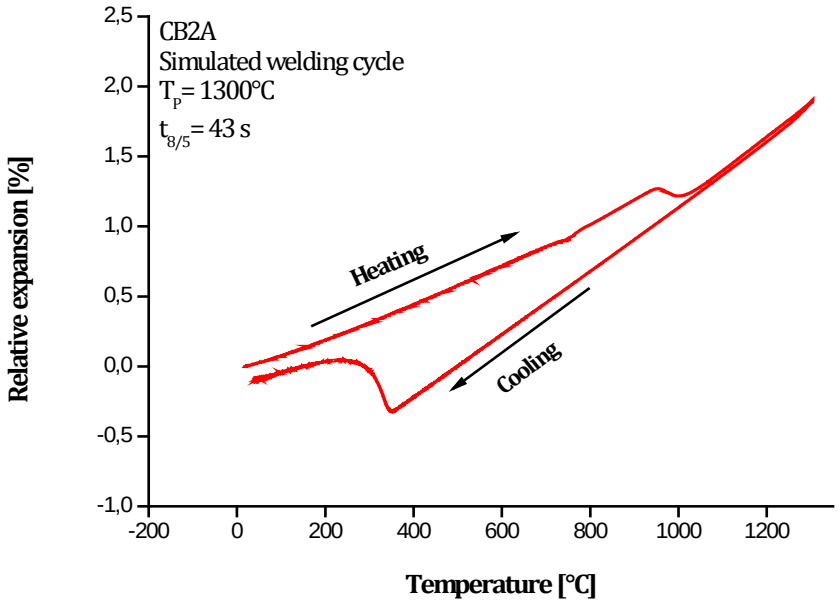


**Figure 19: Simulated welding cycle of CB2A with a heating rate of 100 K $s^{-1}$.**

The first phase transformation occurs at the change of the ferromagnetic sample to paramagnetic (the Curie temperature). The Curie point is at 750°C for CB2A with a heating rate of 100 K $s^{-1}$.

The body-centred tetragonal tempered martensite microstructure is stable up to temperatures below 930°C (the $A_{C1}$ point) and $A_{C1}$ instigates the start temperature of the transformation into face-centred cubic austenite. The transformation of martensite features volume change. This is related to the contraction on the heating dilatometry curve. The sample is fully austenitised at 1052°C ($A_{C3}$). Figure 20 illustrates the determined phase transformation temperatures of a simulated welding cycle of CB2A on heating by using dilatometry.

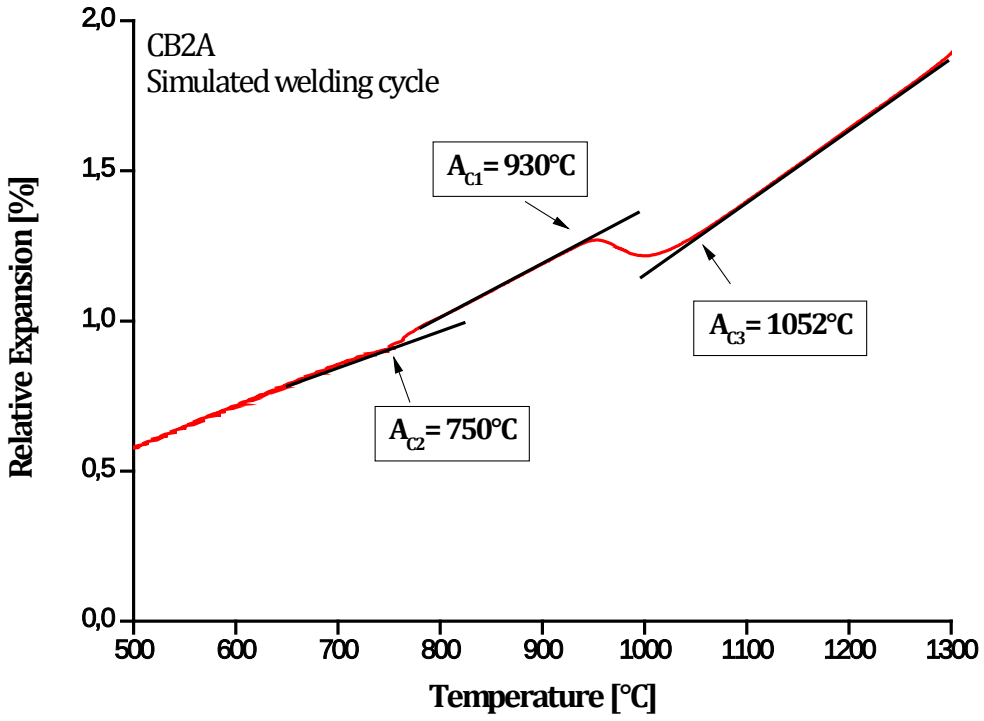


**Figure 20: Phase transformation temperatures on heating of the simulated welding cycle with a heating rate 100 K $s^{-1}$ and a peak temperature of 1300°C of CB2A by dilatometry.**

On air cooling, the transformation of the face-centred cubic austenite into the body-centred tetragonal martensite is observed. The completed simulated welding cycle of CB2A, with a heating rate of 100 K $s^{-1}$, reveals that the beginning of martensite transformation Ms is at 368°C and the martensite finish temperature is around 164°C. At the concluding temperature of the martensite, the whole amount of austenite would normally transform into martensite, but in practice small volume fractions of austenite remain.

Figure 21 presents the determined phase transformation temperatures of the cooling curve of the simulated welding cycle of CB2A, with a cooling time between 800°C and 500°C.

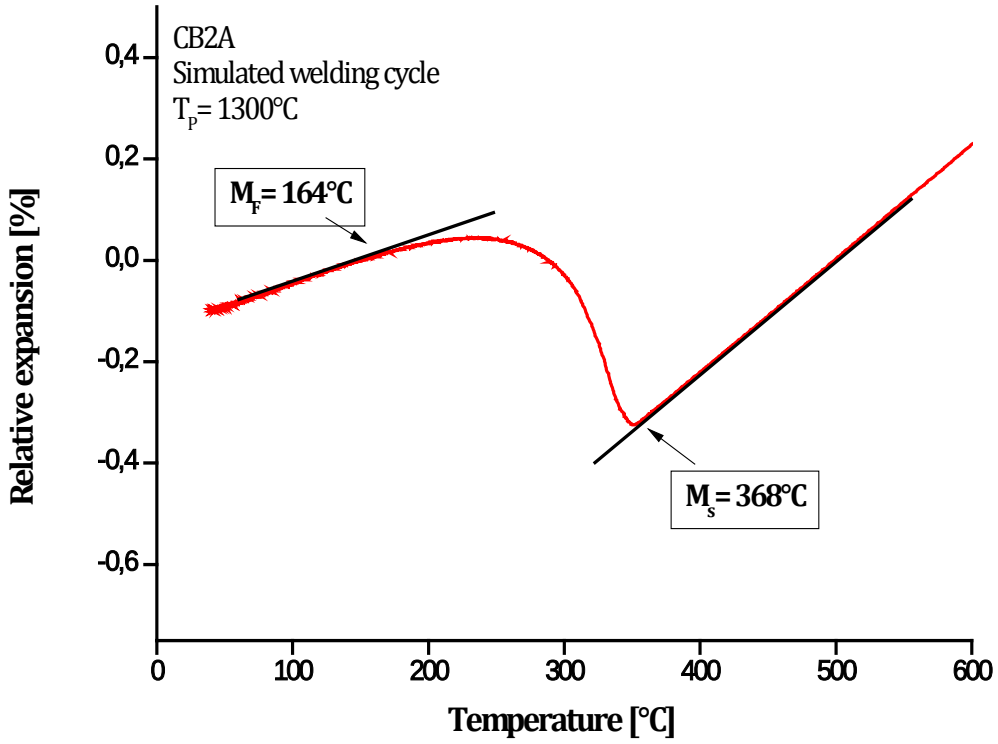


**Figure 21: Phase transformation temperatures on cooling of the simulated welding cycle with a cooling time $t_{8/5}$ = 43 s of CB2A by dilatometry.**

The simulated welding cycle, with a slow heating rate of 10 K $s^{-1}$, peak temperature of 1300°C, cooling rate of 10 K $s^{-1}$ is characterised by $A_{C1}$ (901°C), $A_{C2}$ (735°C) and $A_{C3}$ (1000°C). Additionally, the martensite start temperature is 377°C and the finish temperature 167°C. In contrast to the fast welding cylce are the $A_{C1}$, $A_{C2}$ and $A_{C3}$ lower for the slow welding cycle.

***NPM1***

By applying the welding with high heating rates, it is observed that the phase transformation temperatures are higher in contrast to the slow welding cycle. The fast welding cycle with 100 K $s^{-1}$ to 1050°C peak temperatures is characterised by $A_{C1}$ (933°C), $A_{C2}$ (758°C) and $A_{C3}$ (1015°C). In contrast to the fast welding cycle, the slower welding cycle with heating rate of 10 K $s^{-1}$, peak temperature of 1300°C, a cooling rate of 10 K $s^{-1}$ is characterised by lower phase transformation temperatures, namely $A_{C1}$ (890°C), $A_{C2}$ (750°C) and $A_{C3}$ (995°C).
The martensite start and finish temperatures have the same temperature range for NPM1 and NPM4, which are listed in Table 14.

***NPM4***

NPM4 with a heating rate 10 K $s^{-1}$ to $T_p$= 1300°C and free cooling exhibit the phase transformation temperatures $A_{C1}$ (895°C), $A_{C2}$ (750°C) and $A_{C3}$ (1010°C). On cooling, the martensite start temperature is determined at 410°C and the martensite finish temperature is around 265°C.

### 5.2.1.2 Conclusions

The influence of heating rates on the phase transformation temperatures has been investigated. Higher heating rates during welding increase the phase transformation temperatures $A_{C1,}$ $A_{C2}$ and $A_{C3}$. The phase transformation temperatures of CB2A are higher for the faster heating rate.

Further, the $M_S$ and $M_F$ of NPM1 and NPM4 are higher than CB2A. In the present study, the used cast material CB2A shows a high content of austenite stabiliser carbon (0.168%) in contrast to the other two steels. This leads to supression of the martensite start temperature of CB2A. Moreover, by applying higher temperatures, the grain size increases, the precipitates dissolve which leads to an increase of the alloying element carbon in the observed solution. This interstitial soluted carbon in austenite shifts the martensite start and finish temperatures further to lower temperatures [44,45]. The amount of carbon and alloying elements in the solid solution is not high enough to decreace the martensite start temperatures below 0°C.

The steels of 9Cr-3W-3Co-VNbBN material show that the martensite start and finish temperatures are in the same range, as the carbon content of Heat 1 and Heat 4 is nearly the same. Additionally, it should be mentioned that the cooling time is the same. The martensite finish temperature of NPM1 (N2) is not determined because the measurement time used was to short. NPM4 is characterised by a free cooling in contrary to the other samples. In spite of that, no great variation of the martensite start and finish temperature is observed.

In Table 14, the determined phase transformation temperatures of heating and cooling over the whole simulated welding cycles in all tested steels are summarised.

**Table 14: Obtained phase transformation temperatures of all tested 9% Cr steels.**

| Specimen | Heating rate [K $s^{-1}$] | $T_P$ [°C] | $A_{C1}$ [°C] | $A_{C2}$ [°C] | $A_{C3}$ [°C] | $M_S$ [°C] | $M_F$ [°C] |
|---|---|---|---|---|---|---|---|
| CB2A (A8.1300)* | 100 | 1300 | 930 | 750 | 1052 | 368 | 164 |
| CB2A (A2.1300)* | 10 | 1300 | 901 | 735 | 1000 | 377 | 167 |
| NPM1 (N2.1050)* | 100 | 1050 | 933 | 758 | 1015 | 411 | n.d.[3] |
| NPM1 (N4.1300)* | 10 | 1300 | 890 | 750 | 995 | 410 | 250 |
| NPM4 (M1.1300)* | 10 | 1300 | 895 | 750 | 1010 | 410 | 265 |

[3]n.d. ..... not determinable due to the short measurement time

### 5.2.2 Optical Microscopy

Welding causes an altering of the microstructure, and therefore a prerequisite is to understand the changes in the heat-affected zone (HAZ). The microstructural deformation in the material is connected to changes in properties of the welded components, especially in the creep strengthening. Special attention in this chapter is therefore given on the formation and dissolution temperature of precipitates during thermal treatments. These are important creep strengthening contributors. In order to characterise HAZ microstructure of the 9% Cr steels, samples have been quenched (heating rate 100 K $s^{-1}$) at several temperatures of thermal treatment cycles using quenching dilatometer. The investigation of the quenched HAZ microstructures has been performed using optical microscopy. The simulated welding cycles by dilatometry are equal to those used by in-situ XRD. The following sub-chapters present the obtained results of the investigated three 9% Cr steels at controlled heating and cooling rates.

#### 5.2.2.1 CB2A-Heat 145

The modified 9Cr-1Mo steel cycles has been analysed by optical microscopy. It is worth noting that optical microscopy has been used to investigate the quenched samples at several temperatures of the thermal treatment cycles.

The completed simulated thermal cycles are as follows:

- fast welding cycle: heating rate of 100 K $s^{-1}$, peak temperature of 1300°C with a holding time of 3s, cooling time between 800°C and 500°C of 43 s
- post-weld heat treatment after the fast welding cycle: slow heating and cooling rate of 1.52 K $s^{-1}$, peak temperature of 730°C with a holding time of 2 hours
- slow welding cycle: a heating and cooling rate of 10 K $s^{-1}$, a peak temperature of 1300°C with a holding time of 3s

*Fast welding cycle with a 100 K $s^{-1}$ heating rate*

The optical micrographs on quenched samples of the simulated welding cycle (i.e. 100 K $s^{-1}$ heating rate, cooling time between 800°C and 500°C 43 s, $T_p$ of 1300°C) showing that the zone of unchanged material is up to ca. 700°C.

The quenched sample at 925°C (Figure 22(a)), just below $A_{C1}$, show that CB2A consists of overtempered martensite. The appearance of an overtempered microstructure is a result of a temperature too low for the transformation of tempered martensite into austenite. The martensite is therefore tempered for a second time. The observed martensite laths are narrower compared to their original base material in the as-received condition. The prior austenite grain boundaries and martensite lath boundaries are decorated with Cr rich $M_{23}C_6$.

By heating to 1000°C and subsequent quenching, a significant change in the precipitates behaviour is observed (see Figure 22(b)). The amount of precipitates is lower compared to the tempered initial base material. In the coarse-grained heat-affected zone (CHGAZ), the complete dissolution process of the $M_{23}C_6$ precipitates between the temperature range 1100°C (slightly above $A_{C3}$, Figure 22(c)) and 1165°C (Figure 22(d)) can be seen. Few Cr carbides $M_{23}C_6$ still remain inside the grains. The complete dissolution of the precipitates causes enrichment of the matrix with the elements Cr and C.

At a quenched temperature of 1100°C, the first signs of delta ferrite are observed, as shown in Figure 22(c). This retained delta ferrite occurs as a bright zone between the martensitic lath blocks and on the prior austenite grain boundaries. The morphology of diffusion-governed delta ferrite is a networked shape. The delta ferrite remains in the material due to the incomplete transformation of delta ferrite into austenite on cooling. If the cooling process is too fast, the ferrite delta doesn't have enough time to transform into austenite. Heating up to higher temperatures show that the volume fraction of delta ferrite is increasing (see Figure 22(d)).

The as-quenched state at 1300°C reveals no visible precipitates in the martensitic microstructure, as shown in Figure 22(e).

The analysis of the final HAZ microstructure in the as-welded condition with a peak temperature of 1300°C and cooling time of 43 s between 800°C and 500°C consists of martensite (virgin) and retained delta ferrite (Figure 22(f)). The detection of submicron retained austenite laths is not possible by optical microscopy as a result of low resolution. Figure 22, shows a sequence of optical micrographs of CB2A which have been quenched at several temperatures at the simulated welding cycle with a heating rate of 100 K $s^{-1}$.

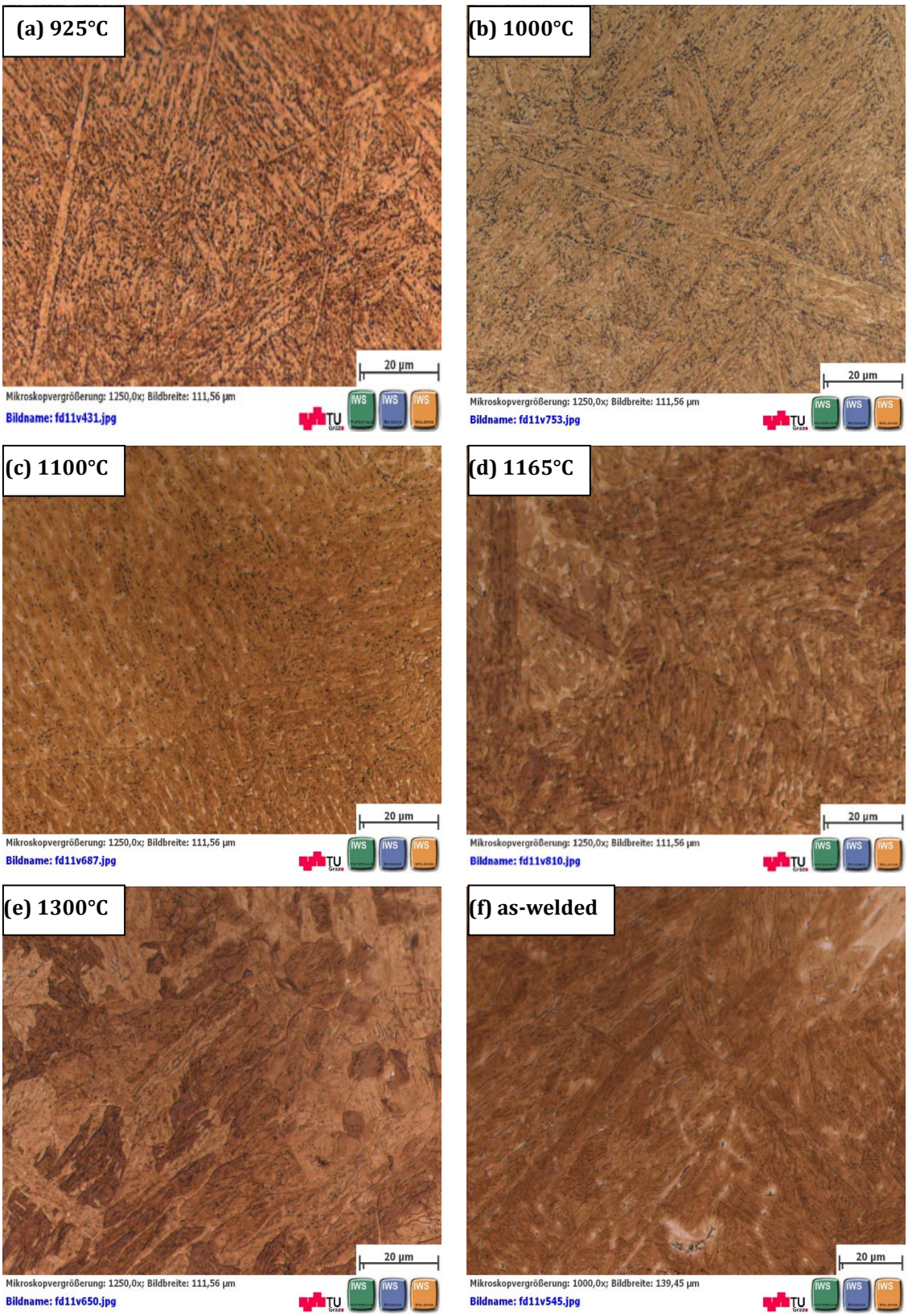


**Figure 22: Quenched optical micrographs on heating of the CB2A-Heat 145 during the simulated welding cycle with 100 K $s^{-1}$ at (a) 925°C, (b) 1000°C, (c) 1100°C, (d) 1165°C, (e) 1300°C and (f) as -welded with $T_p$=1300°C, $t_{8/5}$=43 s.**

*PWHT after fast welding cycle*

The heat-affected zone has been analysed in the as-welded condition in the previous chapter, and in this chapter the above described welding cycle of CB2A with peak temperature of 1300°C and cooling time of 43 s has been followed by a subsequent post weld heat treatment of heating up to 730°C. The focus of this part is on the whole formation process of precipitates during different stages of the post weld heat treatment.

The obtained optical micrographs show that there are no microstructural changes in temperatures of up to 500°C (quenched samples) during the post-weld heat treatment. However, between 500°C and 580°C a re-precipitation of $M_{23}C_6$ in the coarse-grained HAZ ($T_P$=1300°C) begins, as shown in Figure 23(a),(b). The post-weld heat treatment leads to precipitation of the oversaturated alloying elements. The performed heat treatment leads to a diffusion of carbon atoms and the formations of carbides in the matrix begins. These precipitates are located at the prior austenite grain boundaries and the martensite lath boundaries. Few of the chromium carbides re-precipitate inside the grains as well as inside the large delta ferrite grains, which is shown in the as-quenched state at 650°C in Figure 23(c).

The apparent delta ferrite exhibits a network shape and it is clear to determine from the rest of the microstructure in temperatures of up to 650°C. After the complete post-weld treatment, distinction between delta ferrite and the tempered martensitic microstructure is not possible due to its similar appearance in morphology of both, as shown in Figure 23(d).

By applying post weld heat treatment, the size of delta ferrite regimes and the prior austenite grains is the same as the initial base material. The temperature range of PWHT is below $A_{C1}$ and is therefore any phase transformations on heating cannot be observed.
As a result of metallographic investigations, the HAZ of CB2A after post-weld heat treatment exhibits a homogenous tempered martensitic microstructure with $M_{23}C_6$ precipitates along the prior austenite grain boundaries and martensitic lath boundaries. Figure 23 shows the quenched micrographs of CB2A at different temperatures on heating during post weld heat treatment, and one after the post-weld heat treatment.

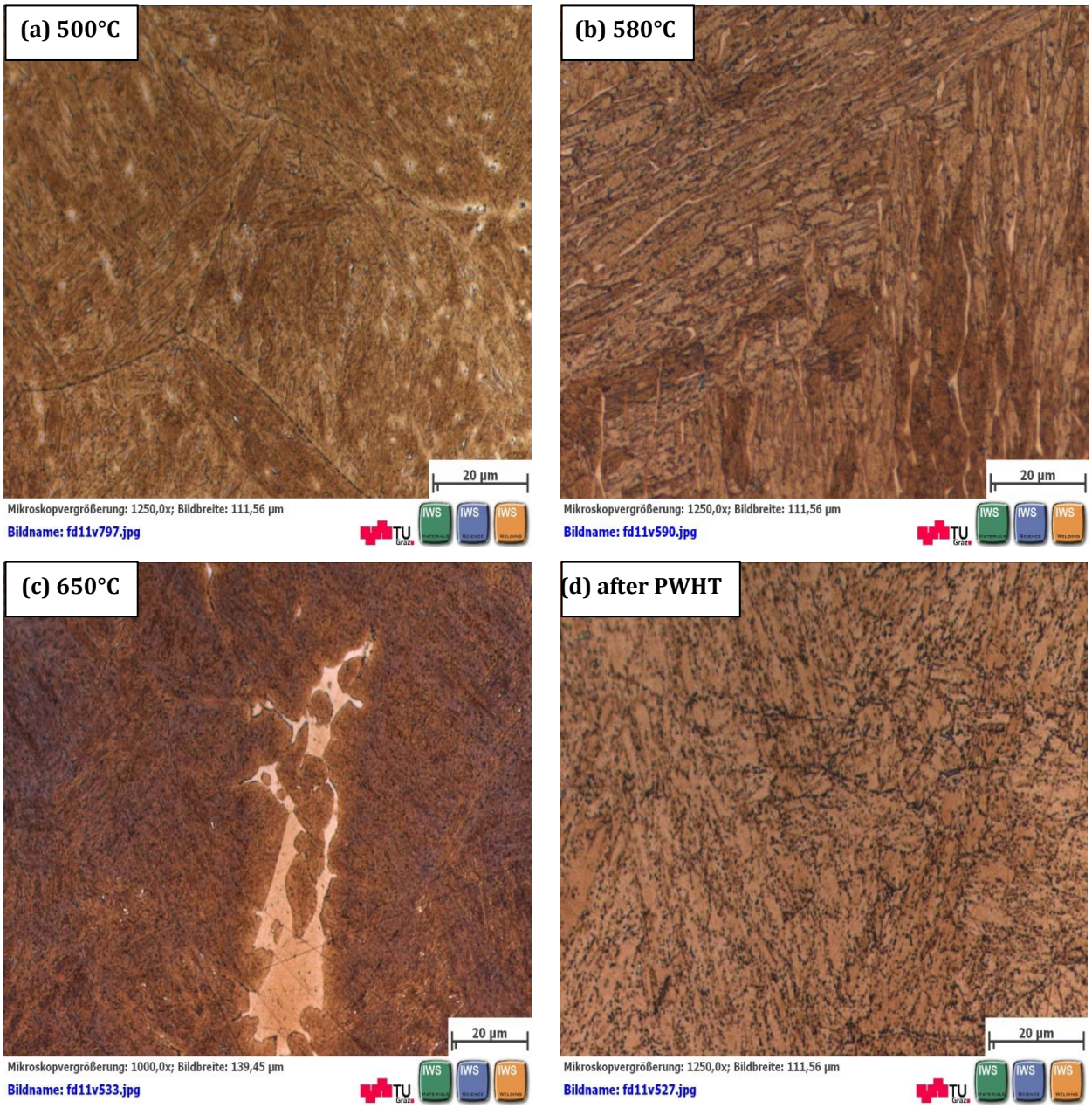


**Figure 23: Optical micrographs of CB2A-Heat 145 quenched at different temperatures on heating during PWHT (a) 500°C, (b) 580°C, (c) 650°C and (d) after complete PWHT.**

*Slow welding cycle with a 10 K $s^{-1}$ heating rate*

In comparison to the above described fast welding cycle, a slow welding cycle has been applied, characterised by a peak temperature of 1300°C, a heating and cooling rate of 10 K $s^{-1}$.

The HAZ simulation up to the peak temperature of 924°C with a heating rate 10 K $s^{-1}$, just above $A_{C1}$ (ICHAZ), shows that the material consists of virgin martensite and overtempered martensite after cooling. By applying a temperature slightly above $A_{C1,}$ a partial transformation of tempered martensite into austenite is observed. The martensitic microstructure is delineated with chromium carbide precipitates at the prior austenite grain boundaries and martensite lath boundaries. The precipitates behaviour changes in the grain-refined zone. The optical micrographs in Figure 24(a),(b) show that the chromium carbide precipitates dissolve in the fine-grained heat-affected zone (FGHAZ) within the temperature range of 1046°C and 1076°C.

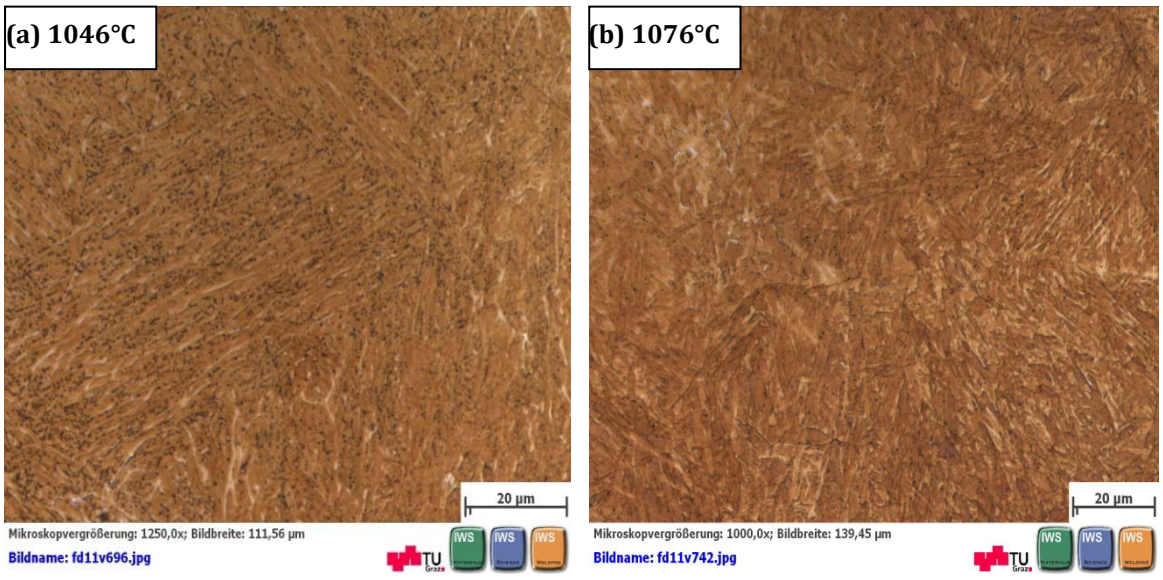


**Figure 24: Quenched optical micrographs of CB2A-Heat145 at (a) 1046°C and (b) 1076°C.**

Additionally, delta ferrite appears for the first time between 1046°C-1076°C, but the volume amount compared to the quenched sample at higher temperatures is relative low. In the as-welded condition with a peak temperature of 1300°C, with heating and cooling rate 10 K $s^{-1}$, the optical micrographs reveal virgin martensite with different amounts of retained delta ferrite, surrounded by lath-shaped martensite. The residual austenite amount is too low to be identified in the obtained micrographs.

### 5.2.2.2 NPM1

The heats used, NPM1 of 9Cr-3W-3Co-VNbBN steel, has been investigated using optical microscopy. It is worth noting that the examination using optical microscopy on the quenched samples has been carried out at several temperatures of the thermal treatment cycles.

The completed simulated thermal cycles are as follows:

*NPM1*

- fast welding cycle: a heating rate of 100 K $s^{-1}$, peak temperature of 1050°C with a holding time of 3s, cooling time between 800°C and 500°C of 43 s
- post-weld heat treatment after the fast welding cycle (Tp= 1050°C): a slow heating and cooling rate of 1.52 K $s^{-1}$, peak temperature of 730°C with a holding time of 2 hours
- slow welding cycle: heating and cooling rate of 10 K $s^{-1}$, peak temperature of 1300°C with a holding time of 3s

*Fast welding cycle with a 100 K $s^{-1}$ heating rate*

The specimen, heated to 980°C and then quenched (between $A_{C1}$ and $A_{C3}$), shows a decrease in the precipitates number density in comparison with the initial base material. As a result, the inter-critical HAZ microstructure consists of virgin martensite and tempered martensite. A comparison of two optical micrographs, one with 980°C and the other with 1050°C reveals that the most precipitates are dissolved within this temperature range (see Figure 25(a),(b)).


**Figure 25: Optical micrographs of NPM1 quenched at (a) 980°C and (b) 1050°C.**

The HAZ microstructure in the as-welded condition with a peak temperature of 1050°C, above $A_{C3}$, then exhibits that the NPM1 consists of martensite. Most of the precipitates are dissolved, but small quantities of precipitates are just visible on the martensite lath boundaries and prior austenite grain boundaries. The metallographic observation shows, as expected, that no delta ferrite is present as the delta formation starts at higher temperatures.

*PWHT after fast welding cycle*

After the welding cycle with a heating rate 100 K $s^{-1}$ up to the peak temperature 1050°C, a post weld heat treatment has been performed on the NPM1 material. The post-weld heat treatment temperature is below the $A_{C1}$ temperature of the material and for 9% Cr steels it is typically 730°C and 2 hours holding time.

Several obtained optical micrographs show that the heat-affected-zone microstructure after the post-weld heat treatment consists of a tempered martensitic microstructure. The low temperature of the post-weld heat treatment allows re-precipitation of the dissolved Cr carbides on the prior austenite grain boundaries and on the martensite lath boundaries. The undissolved precipitates, due to the low peak temperature, coarsen during PWHT and are located primarily at the prior austenite grain boundaries.

Figure 26 (a),(b) shows the comparison of the tempered base material with a fine dispersion of $M_{23}C_6$ to the post-weld heat treated material with coarsened Cr carbides clearly formed on the prior austenite grain boundaries. The grown Cr carbide precipitates are observed particularly on the prior austenite grain boundaries, as the high effective diffusion rate is located on these austenite grain boundaries. This diffusion rate rapidly accelerates the coarsening. The prior austenite grain boundaries are still observable, and changes in the grain size cannot be observed. Additionally, the microstructure morphology, particularly the martensite lath structure after the PWHT, shows no variations in comparison with those in the base material. On the whole, the PWHT doesn't change in grain size. Further micrographs of the post-weld heat treated NPM1 are listed in the Appendix.


**Figure 26: Optical micrographs (a) NPM1 base material and (b) as-welded (Tp= 1050°C) and subsequent completed PWHT.**

*Slow welding cycle with a 10 K $s^{-1}$ heating rate*

In comparison to the above described fast welding cycle, a slow welding cycle is applied, characterised by a peak temperature of 1300°C, a heating and cooling rate of 10 K $s^{-1}$.
Optical micrographs of NPM1 show that a part of the precipitates are dissolved at 1046°C. The complete dissolution of $M_{23}C_6$, however, is achieved at 1076°C in the so called grain-refined zone (FGHAZ). The microstructure of the material at 1076° after quenching to room temperature shows a martensitic microstructure. The grain growth zone (CGHAZ) is observed at higher temperatures, well above the $A_{C3}$ and no precipitates are visible.

The HAZ microstructure in the grain growth zone consists of a virgin martensitic microstructure, with delta ferrite remnants. The delta ferrite phase is observed between the martensitic laths at a highest peak temperature of 1300°C. The morphology of delta ferrite is elongated, as shown in Figure 27. As already mentioned, the detection of residual austenite is not performable. The welding process with $T_p$ of 1300°C causes an untempered lath martensite microstructure.


**Figure 27: Optical micrograph of NPM1 in the as-welded condition with a heating and cooling rate of 10 K $s^{-1}$.**

### 5.2.2.3 NPM4

The received optical micrographs of NPM4 are characterised by a peak temperature of 1300°C, a 10 K $s^{-1}$ heating rate and free cooling to room temperature. Quenching the sample at 900°C (above $A_{C1}$) reveals that the microstructure consists of virgin and overtempered martensite with precipitates along the prior austenite grain boundaries and martensite lath boundaries. On heating, the complete dissolution of $M_{23}C_6$ is reached at 1100°C (see Figure 28(a)). The delta ferrite appears initially as a bright zone between the martensite laths in the quenched sample at 1200°C, as shown in Figure 28(b). After the complete welding cycle with heating rate 10 K $s^{-1}$, peak temperature of 1300°C and free cooling to room temperature the brittle virgin martensite is observable (Figure 28(c)). Further delta ferrite is visible in the as-welded condition, as shown in Figure 28(d). In Figure 28, the quenched optical micrographs of different stages of the simulated welding cycle are shown.

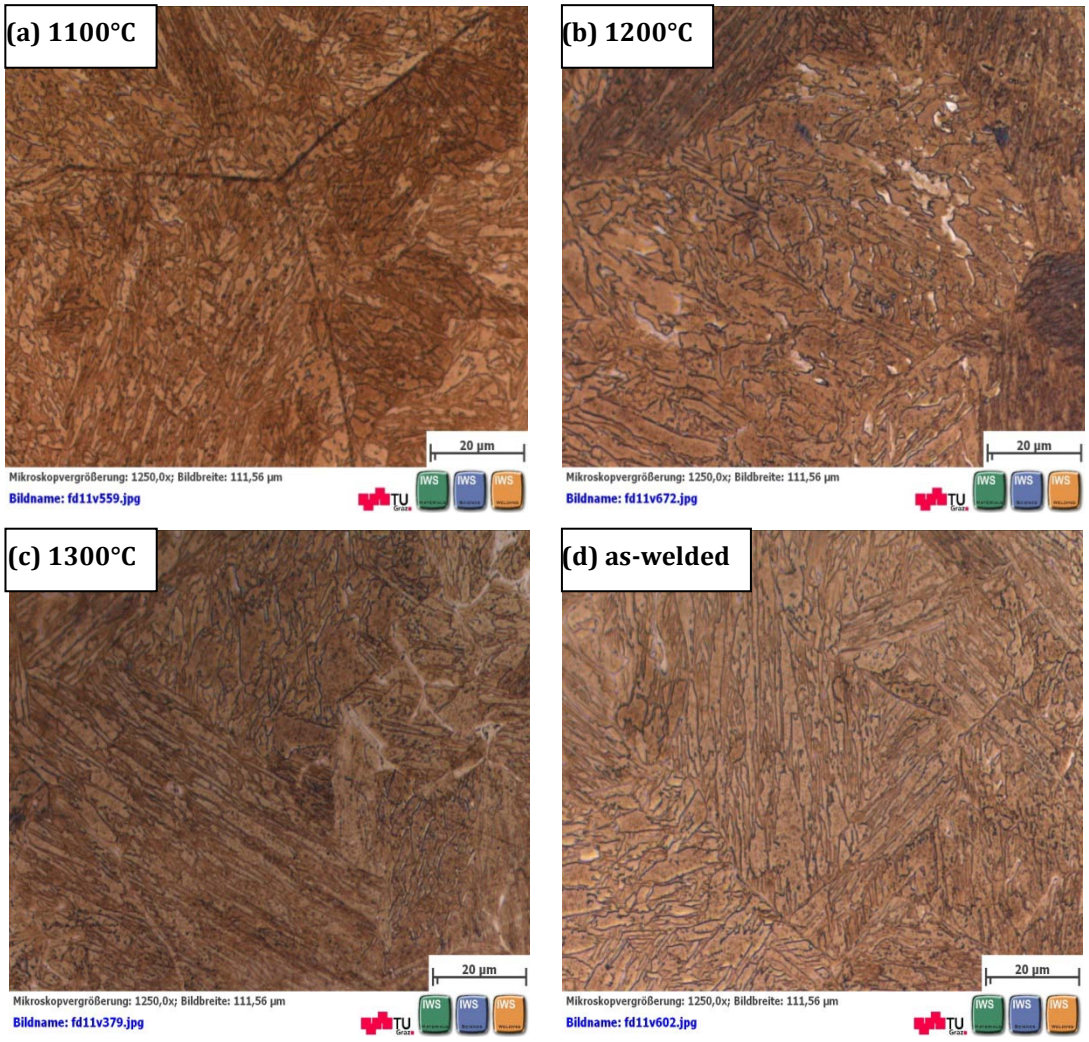


**Figure 28: Optical micrographs of NPM4 quenched at different temperatures (a) 1100°C, (b) 1200°C, (c) 1300°C and (d) as-welded.**

### 5.2.2.4 Conclusions

*Phase transformations*

As mentioned above, the base material in the as-received condition (i.e. after austenisation and the quality heat treatment), the three 9% Cr steels show a tempered martensitic microstructure, with $M_{23}C_6$ precipitates along the prior austenite grain boundaries and the martensite lath boundaries. It is observed that the simulated welding cycles with higher heating rates relative to the slow ones shifts the phase transformation to higher temperatures.

Up to peak temperatures of 700°C, the steels show no changes in the tempered martensitic microstructure in comparison to the initial base material.
Peak temperatures below $A_{C1}$ lead to an overtempered martensite with narrower lath-bundles. Due to the low temperature, no phase transformations are enabled and therefore the martensitic microstructure is tempered for a second time.

By applying peak temperatures between $A_{C1}$ and $A_{C3}$ in the inter-critical heat-affected zone, the steels consist of overtempered martensite and virgin martensite. The heat-affected zone microstructure of the tempered martensite is delineated with $M_{23}C_6$ precipitates at the prior austenite grain boundaries and martensite lath boundaries.

With heating of up to temperatures above $A_{C3}$, virgin martensite microstructure is visible.

By applying temperature ranges in coarse grained HAZ, the delta ferrite phase with a skeletal network-shape is observed as a bright zone between the martensitic lath blocks and on the prior austenite grain boundaries in all three 9% Cr steels. On heating, austenite transforms into delta ferrite at higher temperatures, and if the cooling process is too fast, the delta ferrite does not transform completely into austenite. The volume fraction of delta ferrite increases at higher temperatures on heating.

As shown in Table 15 the welding cycles with higher heating rates shift the diffusion-governed delta ferrite formation to higher temperatures. The identification of the low amount of residual austenite phases in all three steels cannot be verified by the optical microscopy, due to the resolution being too low.

**Table 15: Summary of the start temperatures of delta ferrite formation during welding.**

| Specimen | Heating rate [K $s^{-1}$] | Peak temperature [°C] | Delta ferrite (δ) [°C] |
|---|---|---|---|
| CB2A (A8.1300)* | 100 | 1300 | 1100 |
| CB2A (A2.1300)* | 10 | 1300 | 1046-1076 |
| NPM1 (N4.1300)* | 10 | 1300 | 1300 |
| NPM4 (M1.1300)* | 10 | 1300 | 1200 |

After the post-weld heat treatment, the material shows a homogenous microstructure. The grain size of the prior austenite in particular is the same when compared to the initial base material. Furthermore, the morphology of the martensite lath structure seams equal to the original base material. To determine a clear statement, techniques with higher resolution capabilities should be used in measuring.

*Precipitates behaviour*

In all three 9% Cr steels, the dissolution process of $M_{23}C_6$ during the welding cycles with high peak temperatures is observed. In CB2A and NPM1 with a peak temperature of 1300°C, heating and cooling rates of 10 K $s^{-1}$, total dissolution is achieved between the temperature range 1046°C and 1076°C in the FGHAZ. NPM4 doesn't show any precipitates at 1100°C. In Table 16, the averages values and the association standard deviation of the dissolution temperatures of the Cr carbides $M_{23}C_6$ during welding cycles are summarised. The obtained results show that the dissolution temperatures of the precipitates are dependent on heating rate. CB2A with a high heating rate shows higher dissolution temperatures, in contrast to the slow welding cycle with the same peak temperature, as shown in Table 16. On the basis of these obtained results, the dissolution temperatures of NPM1, NPM4 and modified CB2A with the equal welding conditions are within the same range.

**Table 16: Summary of the average value and standard deviation of dissolution temperatures of $M_{23}C_6$ during welding.**

| Specimen | Heating rate [K $s^{-1}$] | Peak temperature [°C] | Dissolution temperature [°C] |
|---|---|---|---|
| CB2A (A8.1300)* | 100 | 1300 | 1132 ± 46 |
| CB2A (A2.1300)* | 10 | 1300 | 1061 ± 21 |
| NPM1 (N4.1300)* | 10 | 1300 | 1061 ± 21 |
| NPM4 (M1.1300)* | 10 | 1300 | 1050 ± 71 |

The post-weld heat treatment causes a re-precipitation of the dissolved precipitates during welding along the prior austenite grain boundaries and martensite lath boundary. In CB2A, after the fast welding cycle, the $M_{23}C_6$ re-precipitates between 500°C and 580°C on heating during the post-weld heat treatment. The Cr carbides are visible at the austenite grain boundaries and martensite lath boundaries. Delta ferrite is still apparent after the PWHT due to the temperatures being too low to see any transformations of delta ferrite into austenite. By applying low peak temperatures, for instance at 1050°C, the precipitates partly dissolve, and a subsequent PWHT leads to an additional re-precipitation. In addition, during PWHT the undissolved precipitates coarsen mainly on austenite grain boundaries, as a result of the diffusion rate being high. By performing post weld heat treatment, the grain size of the prior austenite grain boundaries or delta ferrite does not change.

### 5.2.3 Micro Hardness of the Heat-affected Zone

#### 5.2.3.1 CB2A-Heat 145

The micro hardness of the virgin martensite in the HAZ, in the as-welded condition with a heating rate of 100 K $s^{-1}$, peak temperature of 1300°C and cooling time of $t_{8/5}$= 43 s in the coarse-grained heat-affected zone, has been determined around 464 HV0.010.

The micro hardness of the slower welding cycle (peak temperature of 1300°C, heating and cooling rate 10 K $s^{-1}$) has been measured around 538 HV0.010. In comparison to the tempered base material of CB2A (265 HV0.010), which is described in chapter 4.3.4, the micro hardness of the virgin martensite is significantly higher. The high micro hardness of virgin martensite, in contrast to the tempered martensitic base material, is a result of high temperatures as the precipitates dissolve and the element carbon diffuses into the matrix leading to harder martensite.

The delta ferrite zone, at a peak temperature of 1300°C, heating and cooling rates of 10 K $s^{-1}$, reveals micro hardness values of around 229 HV0.010, as shown in Figure 29 (a). The delta ferrite micro hardness, in comparison to the virgin martensite, is lower. The high hardness of the martensite is due to a distorted crystal structure with trapped carbon atoms, because carbon contributes significantly to the hardness.

The CB2A material after fast welding (with a heating rate of 100 K $s^{-1}$, to a peak temperature of 1300°C) and subsequent post-weld heat treatment, the microstructure exhibits a tempered martensitic microstructure, with chromium carbides precipitation along the martensitic lath boundaries and prior austenite grain boundaries. The obtained micro hardness results after PWHT show that the hardness value is approximately 329 HV0.010. In contrast to the as-welded material (before PWHT), the hardness values after PWHT are lower. This occurs during post-weld heat treatment when the carbon diffuses out of the martensite structure and forms carbides.

Figure 29 (b),(c) shows the hardness micrographs of the CB2A material in their as-welded condition, with a heating rate of 100 K $s^{-1}$ to a peak temperature of 1300°C and after the post-weld heat treatment.

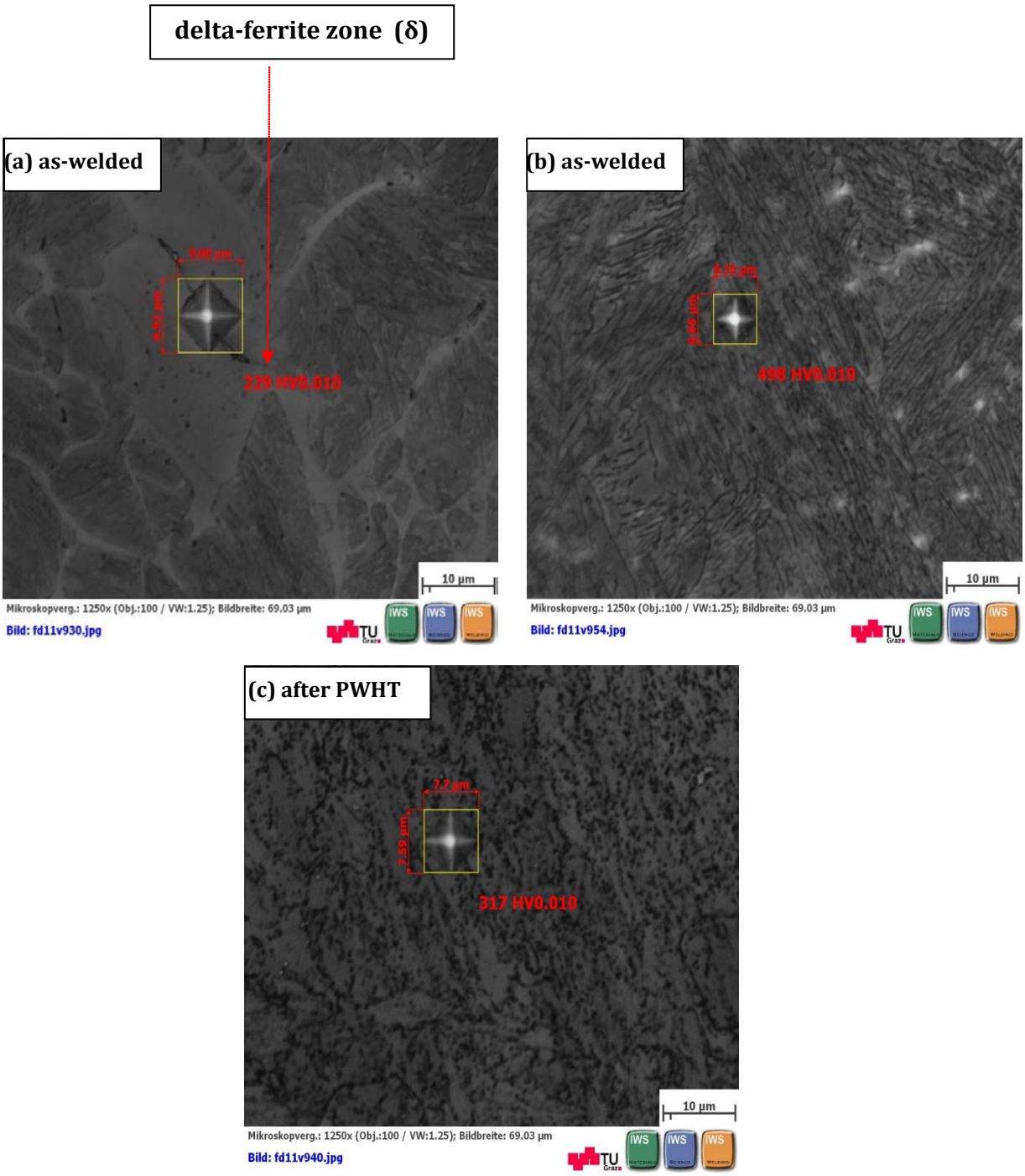


**Figure 29: Hardness micrographs of CB2A-Heat145 (a) delta ferrite zone in the as-welded condition of the slow welding cycle with heating rate of 10 K $s^{-1}$, (b) martensite (virgin) in the as-welded condition with a heating rate of 100 K $s^{-1}$ and (c) after PWHT of the fast welding cycle.**

### 5.2.3.2 NPM1

The obtained results of the micro hardness show that the NPM1, in the as-welded condition with a peak temperature of 1050°C, a heating rate 100 K $s^{-1}$ and cooling time of 43 s, has a hardness value of around 465 HV0.010. The virgin martensite in the coarse grained zone, with a peak temperature of 1300°C and a heating and cooling rate 10 K $s^{-1}$ show a micro hardness of 378 HV0.010. The measurement of the micro hardness of delta ferrite in the HAZ was difficult as the delta ferrite zones were too bright.

After the fast welding cycle, a post-weld heat treatment has been performed and the obtained micro hardness result has been measured around 324 HV0.010. After the post-weld heat treatment, a re-precipitation takes place in the HAZ ($T_p$=1050°C) and this leads to a softening by tempering the HAZ. In comparison to the micro hardness of virgin martensite with both heating rates, the obtained hardness values of the post-weld heat treated HAZ are lower. Figure 30 presents the micro hardness in the as-welded condition and the subsequent PWHT of NPM1.

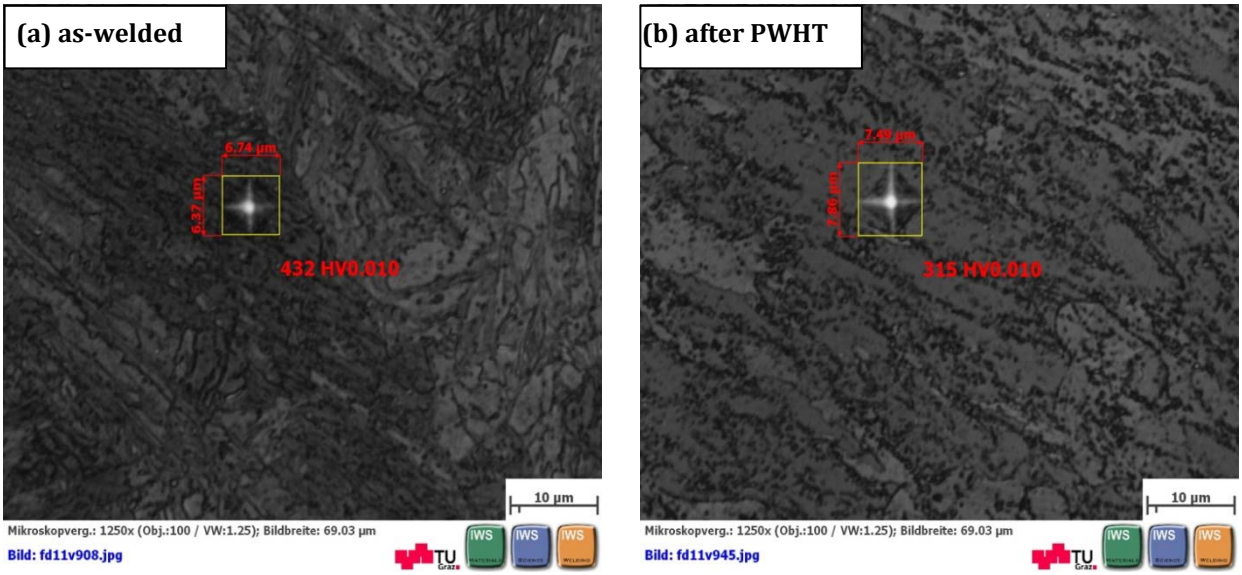


**Figure 30: Hardness micrographs of NPM1 (a) in the as-welded state ($T_p$=1050°C), (b) as-welded state (Tp=1050°C) and subsequent PWHT heating to 730°C.**

### 5.2.3.3 NPM4

The average micro hardness of NPM4 virgin martensite in the grain growth zone ($T_p$= 1300°C) has been measured about 479 HV0.010. The identification of delta ferrite was relatively difficult due to its strong brightness. After this welding cycle, a post-weld heat treatment is not performed and therefore there are no results available for the post-weld treated NPM4. In comparison to the base material, the hardness of the virgin martensite is relatively high due to the same cause for aforementioned CB2A and NPM1 steels. Figure 31 shows the micro hardness of NPM4 in the as-welded condition with a heating rate of 10 K $s^{-1}$, free cooling and peak temperature of 1300°C.

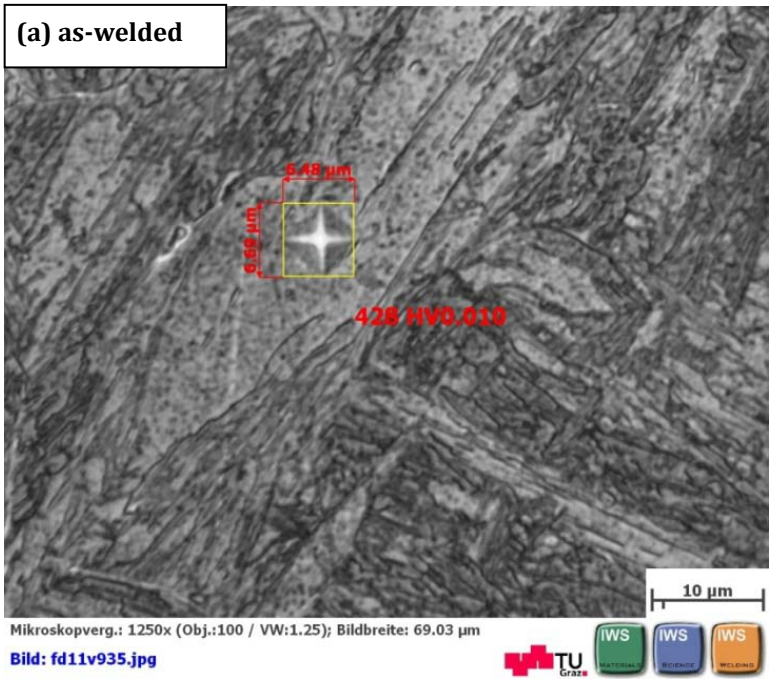


**Figure 31: Hardness micrograph of NPM4 in the as-welded condition .**

### 5.2.3.4 Conclusions

The micro hardness results of the base materials are on the same level for all three 9% Cr steels.
The micro hardness of the heat-affected zone after welding (consisting of virgin martensite) is higher in comparison to the initial base materials in their as-received condition (i.e. normalising and tempering). The as-welded steels yield higher micro hardness results because, at high temperatures, the precipitates dissolve completely. This leads to an increase in carbon content of the martensite. On cooling, the austenite transforms into martensite. The formed martensite traps carbon atoms inside the crystal structure, which cannot disperse, and this leads to the formation of a distorted crystal structure which is then harder. The investigated steels reveals in the coarse grained heat-affected zone ($T_p$= 1300°C) a similar micro hardness.

After the post-weld heat treatment of the HAZ (below the $A_{C1}$ of the material), there is a reducing of the micro hardness values relative to that of the base material. The post-weld heat treatment leads to a diffusion of the trapped carbon atoms and the carbon forms, with further elements in the matrix carbides. Due to the carbon diffusion of the matrix, the martensite exhibits a less distorted structure, and this leads to lower hardness values. By and large, the post-weld heat treatment leads to a softening of the hardness of the heat-affected zone.

Sadrawetz [46] documents that the micro hardness of the 9Cr-3W-3Co-VNbBN steel (NPM1 and NPM4) increase between $A_{C1}$ and $A_{C3.}$ Austenite starts to form at $A_{C1}$, and up to $A_{C3}$ the amount of austenite increases, which leads to higher hardness values. The micro hardness values show no changes above $A_{C3.}$ At high peak temperatures ($T_P$= 1300°C), austenite starts to transform into delta ferrite and this leads to a decrease in hardness.

In Table 17, the micro hardness results are summarised as average and standard deviation in the as-received, as-welded and after post-weld of CB2A-Heat 145, NPM1 and NPM4.

**Table 17: Summary of the micro hardness of 9% Cr steels in their as-received condition, their as-welded state and after PWHT.**

| Specimen | Heating rate [K $s^{-1}$] | $T_P$ [°C] | Base material [HV0.010] | As-welded [HV0.010] | After PWHT [HV0.010] |
|---|---|---|---|---|---|
| CB2A (A8.1300)* | 100 | 1300 | 265 | 464±33 | 329±13 |
| CB2A (A2.1300)* | 10 | 1300 | 265 | 538±55 | n.a.[4] |
| NPM1 (N2.1050)* | 100 | 1050 | 269 | 465±48 | 324±26 |
| NPM1 (N4.1300)* | 10 | 1300 | 269 | 378±34 | n.a.[4] |
| NPM4 (M1.1300)* | 100 | 1300 | 287 | 479±69 | n.a.[4] |

[4]n.a. …….. not available: post-weld heat treatment has not been carried out

### 5.2.4 In-situ X-ray Diffraction

To investigate the influence of thermal treatments of the heat-affected zone in 9-12% Cr steels, in-situ X-ray diffraction is used. By applying in-situ XRD, direct monitoring of phase transformation during thermal cycles has been carried out. Heating rates of 100 K $s^{-1}$ and 10 K $s^{-1}$ have been applied and these simulated welding cycles are equal to those obtained with dilatometry.

#### 5.2.4.1 CB2A-Heat 145

*Fast welding cycle with a heating rate of 100 K $s^{-1}$*

Two welding cycles have been performed, one with a higher heating rate and one with a lower heating rate. This chapter describes the simulated HAZ microstructure with a faster heating rate.

The fast welding cycle is characterised by a peak temperature of 1300°C, a heating rate of 100 K $s^{-1}$ and a cooling time of between 800°C-500°C in 43 s. The obtained in-situ XRD results confirm that CB2A exhibits a tempered martensitic microstructure in its as-received condition. The tempered martensite pattern show primarily body-centred cubic (bcc) peaks and weak face-centred cubic (fcc) peaks of chromium carbides $M_{23}C_6$.

Figure 32 shows the progression of the bcc (111) ferrite or martensite peak and fcc (111) austenite peak during the thermal welding cycle of the material. In the graph, d-spacing against intensity is plotted. This graph gives an overview of the whole phase transformations during welding. The temperature of the material is shown on the right side of the graph. When heating to higher temperatures, it is observed that the d-spacing values of bcc shift to higher d-spacing values due to thermal expansion. By applying the fast welding cycle, the austenisation on heating has been performed rapidly. This rapid austenisation makes it difficult to determine the exact start and end temperature of the austenite formation.

Heating to temperatures close to the peak temperature of 1300°C a dual phase of bcc and fcc peaks are observed. The bcc (111) reappears, corresponding to the delta ferrite formation, but with a heating rate of 100 K $s^{-1}$. During heating with temperatures ranging from 990°C to 1300°C, a complete dissolution of the chromium carbides $M_{23}C_6$ is observed.

During the cooling process, a decrease in the intensity of the delta ferrite peaks is visible, which indicates a transformation of the delta ferrite into austenite. The delta ferrite, however, is not completely transformed, as on larger scale of the XRD patterns, bcc peaks remain. The austenite starts to transform into martensite at approximately 410°C, and the martensite finish temperature is reached at 150°C. The HAZ microstructure of CB2A in the as-welded condition is characterised by martensite (virgin), retained austenite and retained delta ferrite.

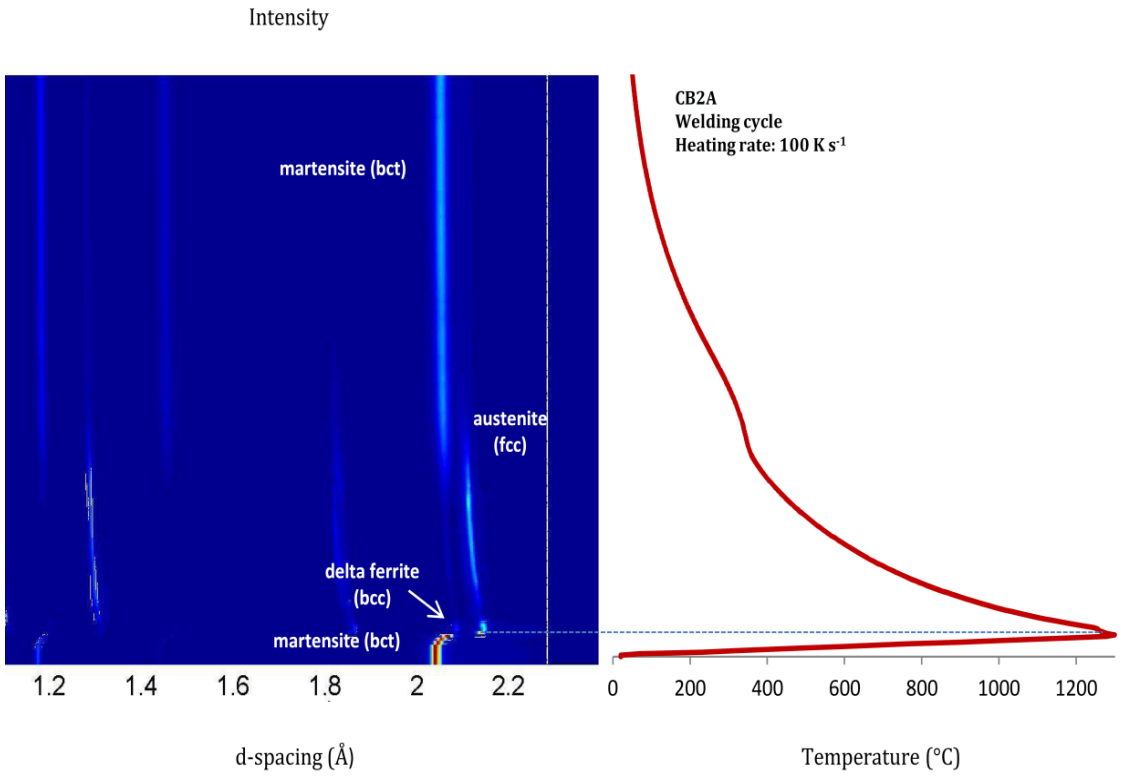


**Figure 32: Phase transformations in CB2A-Heat 145 with a fast heating rate of 100 K $s^{-1}$ by in-situ X-ray diffraction.**

In Figure 33, the progression of the phases in the in-situ XRD pattern during the whole simulated welding cycle of CB2A-Heat 145 is shown. In this graph, the bcc peaks of ferrite or martensite and the austenite peaks are shown. By using X-Ray diffraction technique a distinction between ferrite (α and δ) and martensite is not possible due to the similar lattice constants of body-centred cubic and body-centred tetragonal [40]. This graph provides an alternative visualisation of Figure 32 in three dimensions.

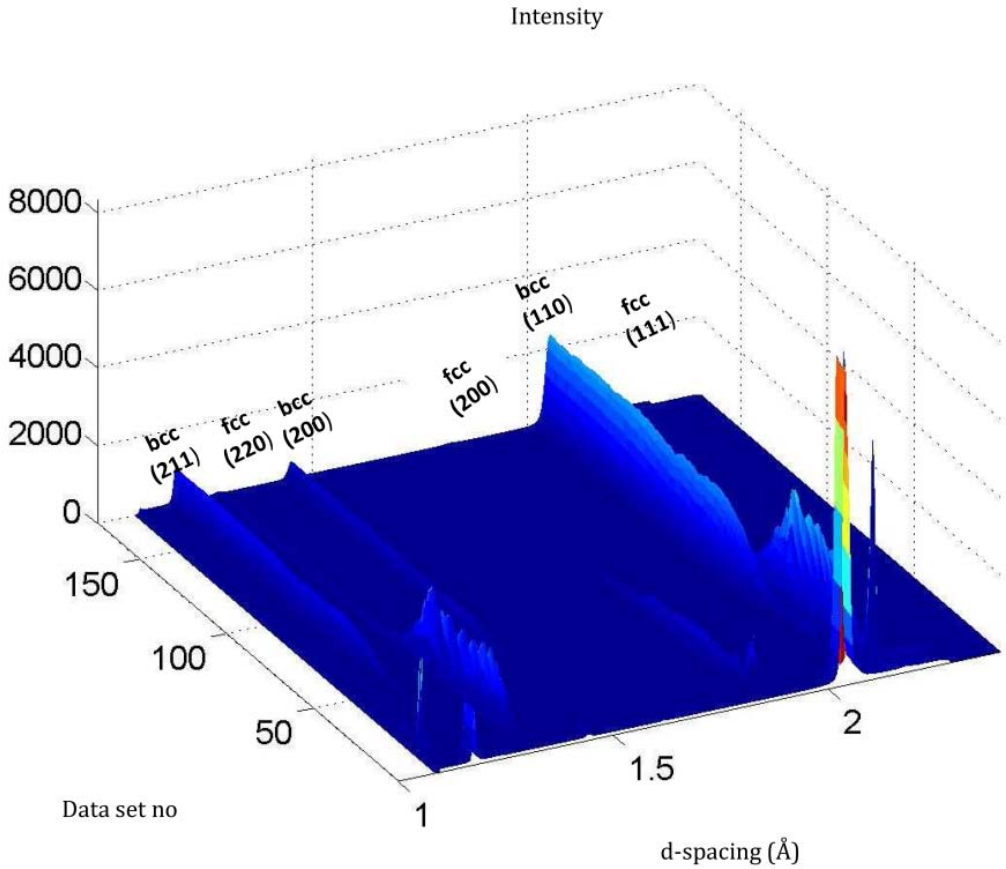


**Figure 33: 3D illustration of phase transformations in modified 9Cr-1Mo steel with a fast heating rate of 100 K $s^{-1}$ by in-situ X-ray diffraction.**

*Post-weld heat treatment after fast welding cycle*

After the fast welding cycle with a peak temperature of 1300°C, a heating rate of 100 K $s^{-1}$ and a cooling time of $t_{8/5=}$ 43 s the HAZ microstructure is post-weld heat treated to make sure the onset of the re-precipitation takes place.

In Figure 34, micrographs of the different stages of the post weld heat treatment are shown. The as-welded material consists of virgin martensite, retained delta ferrite and retained austenite. The XRD pattern at 19°C reveals no precipitates in the HAZ microstructure (see Figure 32(a)). When the temperature is increased to 531°C, the fcc peaks of the $M_{23}C_6$, especially the fcc (622), fcc (440) and fcc (422) are clearly observed, as shown in Figure 34(b). The X-ray diffraction pattern at 549°C shows weak precipitate peaks (Figure 34(c)), but heating of up to 580°C reveals that the intensity of the fcc peaks increases (Figure 34(d)). In contrast to the pattern at 580°C, the obtained XRD pattern after complete post-welding heat treatment exhibits a fully developed precipitate microstructure, as shown in Figure 34(e).

The final HAZ microstructure after post-weld heat treatment presents a tempered microstructure located with precipitates at the prior austenite grain boundaries and martensitic lath boundaries. Additionally, retained peaks of austenite are clearly observable.

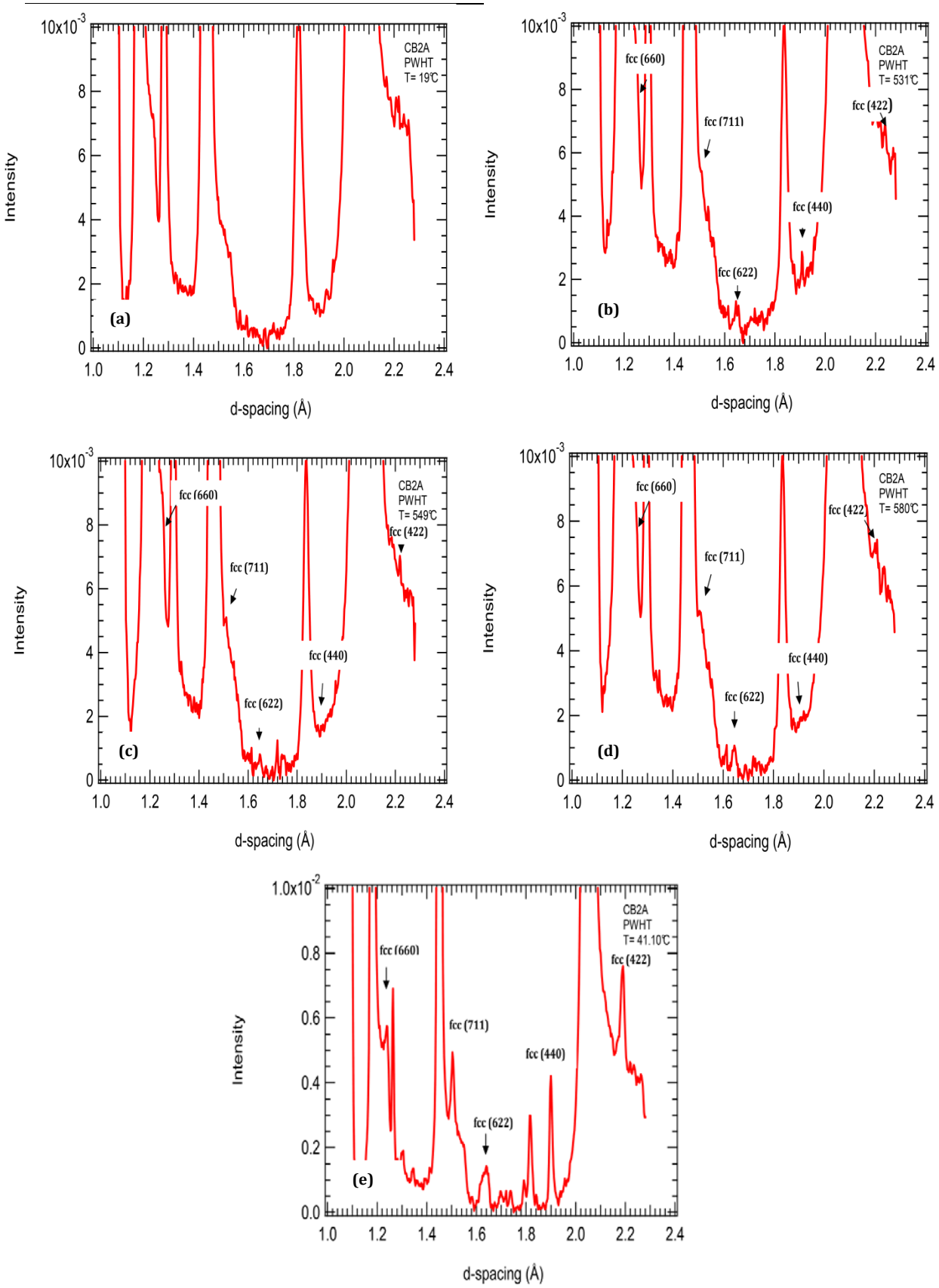


**Figure 34: In-situ X-ray diffraction pattern at different temperatures during PWHT (a) initial base material, (b) at 531°C with identified fcc peaks, (c) at 549°C with weak fcc peaks, (d) at 580°C with matured fcc peaks, (e) after complete PWHT with precipitates on mature stage.**

*Slow welding cycle with a heating rate of 10 K $s^{-1}$*

The initial base material of the slow welding cycle consists of a tempered martensitic microstructure, with bcc peaks and fcc peaks of the precipitates. Retained austenite peaks are also observed in some samples.

The graph in Figure 35 gives an overview of the whole phase transformations during the slow-welding cycle. In Figure 33, X-ray diffraction pattern at several temperatures are listed to present a more detailed overview.

The XRD pattern, at approximately 900°C indicates that the martensite begins to transform into austenite. The austenite onset point at 900°C for $A_{C1}$ and 1016°C for $A_{C3}$ is determined.

As shown in Figure 36(a), when heating up to 1016°C, the CB2A material consists completely of austenite. At 1165°C, a transformation of austenite into delta ferrite is visible. At an approximate peak temperature of 1300°C, ferrite and austenite peaks are visible (see Figure 36b). During cooling, the austenite starts to transform into martensite. The martensite start ($M_S$) temperature is about at 400°C. The martensite finish temperature ($M_F$) is determined at around 152°C. During welding at about 986°C, the intensity of the fcc peaks start to decrease and the complete $M_{23}C_6$ precipitates dissolve up to a temperature of approximately 1076°C. After the complete thermal welding treatment, the resulting HAZ microstructure consists of virgin martensite (bcc peaks), retained austenite and retained delta ferrite. The diffraction pattern after the welding is shown in Figure 36(c).

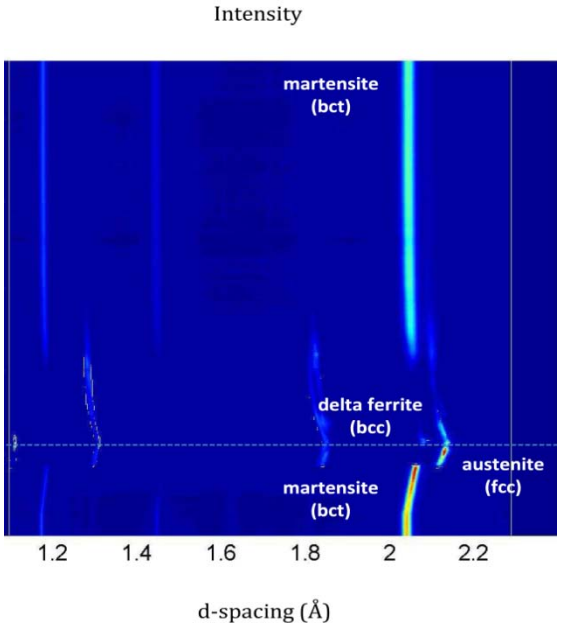


**Figure 35: Phase transformations in modified 9Cr-1Mo steel with a slow heating rate of 10 K $s^{-1}$ by in-situ X-ray diffraction.**

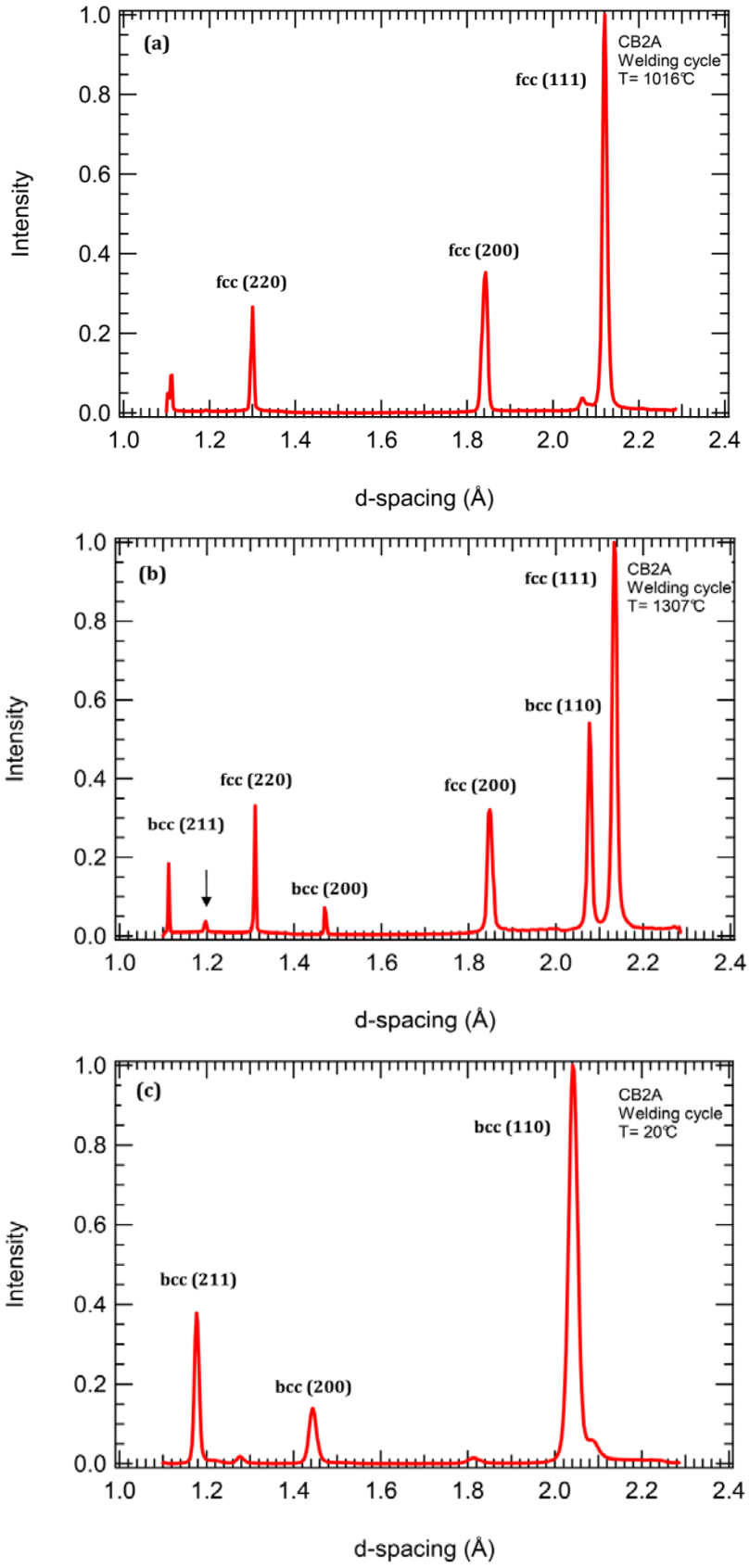


**Figure 36: In-situ X-ray diffraction patterns obtained of CB2A at different temperatures during slow welding cycle (10 K $s^{-1}$) (a) 1016°C on heating, (b) 1307°C on heating and (c) 20°C on cooling.**

### 5.2.4.2 NPM1

In the next sub-chapters, the obtained in-situ XRD measurement results in 9Cr-3W-3Co-VNbBN steels Heat 1 are summarised, and Table 18 gives an overview of the performed thermal cycles with the experimental conditions.

**Table 18: Summary of thermal cycles of Heat 1 by in-situ XRD.**

| Material | Peak temperature [°C] | Heating rate [K $s^{-1}$] | Cooling | Target |
|---|---|---|---|---|
| NPM1 (N2.1050)* | 1050 | 100 | $t_{8/5}$= 43 s | Welding cycle |
| NPM1 (N2.730)* | 730 | slow | - | PWHT |
| NPM1 (N4.930)* | 930 | 100 | $t_{8/5}$= 43 s | Welding cycle |
| NPM1 (N4.730)* | 730 | slow | - | PWHT |
| NPM1 (N5.1300)* | 1300 | 10 | 10 K $s^{-1}$ | Slow welding cycle |

*Fast welding cycle with a heating rate of 100 K $s^{-1}$*

The fast welding cycle is characterised by a heating rate of 100 K $s^{-1}$ to a peak temperature of 1050°C. The cooling time between 800°C and 500°C is 43 s.
The initial base material consists of a tempered martensitic microstructure, with face-centred cubic peaks of $M_{23}C_6$ on the prior austenite grain boundaries and martensite lath boundaries. The HAZ microstructure, at about 1050°C, is characterised by a dual phase region of martensite and austenite, because both body-centred cubic and face-centred cubic peaks are present. The martensite transformation into austenite passes very quickly due to the fast heating rate. Applying a fast heating rate does not allow to determine the phase transformations $A_{C1}$ and $A_{C3}$ on heating. Around a temperature of 1050°C, the $M_{23}C_6$ peaks are relatively weak as a result of the precipitates partial dissolution. During cooling at 426°C, the intensity of fcc starts to decrease. At this point, the austenite starts to transform into martensite. The martensite finish temperature is about 256°C. The simulated HAZ microstructure in the as-welded condition consists of martensite with weak fcc precipitate peaks and residual austenite.

*Post weld heat treatment after fast welding cycle*

The initial microstructure pattern (before heat treatment) shows bcc peaks of martensite and $M_{23}C_6$ fcc peaks. The observed fcc peaks are relatively weak, as the before applied welding cycle with a peak temperature of 1050°C causes partial dissolution. Additionally, after the applied post weld heat treatment a significant increase in the intensity of the precipitate peaks at 550°C is visible. An increase in the intensity indicates that the precipitates dissolve during welding re-precipitate.

*Fast welding cycle with a heating rate of 100 K $s^{-1}$*

The HAZ microstructure is simulated with heating rate of 100 K $s^{-1}$ and a low peak temperature of 930°C. Close to the peak temperature of around 930°C, the martensite starts to transform into austenite, as the diffraction pattern shows a dual phase of body-centred cubic peaks and face-centred cubic peaks. The precipitates in the sample remain unchanged due to the low temperature. The austenite finish temperature, however, is not reached. A temperature of 930°C is just below the austenite finish temperature $A_{C3}$. During cooling, the austenite phase starts to transform into martensite at a temperature of 430°C. Finish of the martensitic phase formation is achieved at 247°C. The weld-treated heat-affected zone microstructure exhibits a newly formed and tempered martensite. Furthermore, the microstructure in its as-welded state contains of undissolved precipitates.

*Post-weld heat treatment after a faster welding cycle*

The initial base material (before applying post-weld heat treatment) consists of predominantly body-centred cubic peaks and weak face-centred cubic peaks of $M_{23}C_6$. An increase of the fcc peaks is observed during post-weld heat treatment which indicates reprecipitation of the $M_{23}C_6$. The post-weld heat treatment doesn't cause any significant changes to the matrix.

*Slow welding cycle with a heating rate of 10 K $s^{-1}$*

The slower welding cycle is characterised by a peak temperature of 1300°C (with a holding time 3 s at the $T_p$) and a heating and cooling rate of 10 K $s^{-1}$.

The initial base material consists of body-centred cubic peaks of martensite, and on a larger scale, face-centred cubic peaks of $M_{23}C_6$ are visible, as shown in Figure 37(a). When heating to higher temperatures, it is observed that the d-spacing values of bcc increase due to thermal expansion. When heating up to 900°C, the obtained X-ray diffraction pattern reveals that the microstructure consists of bcc peaks and fcc peaks. At this $A_{C1}$ point, tempered martensite starts to transform into austenite, and the material is fully austenitised at around 1016°C ($A_{C3}$).

The XRD pattern in Figure 37(b) at 1016°C on heating shows that only face-centred cubic peaks of austenite are visible. The $M_{23}C_6$ chromium carbides start to dissolve at temperature of 956°C or slightly below, and the complete dissolution is reached at around 1076°C during heating. When heating to higher temperatures, the d-spacing values of fcc austenite increases until the delta formation begins at around 1265°C. The delta ferrite increases with higher temperatures, and the XRD pattern concludes at a peak temperature of 1295°C (see Figure 37(c)). This shows that there is a delta ferrite increase, contrary to those heated to 1265°C.

Cooling after a peak temperature of 1295°C shows that the intensity of the bcc delta ferrite peaks decrease. This indicates the transformation of delta ferrite into austenite. A further cooling down to 433°C shows that the bcc peaks reappear indicating the martensite start temperature. At this point, austenite transforms into martensite. The sample at 224°C consists only of bcc peaks of martensite (virgin), and this is the so called martensite finish temperature.

The HAZ microstructure of the welded NPM1 consists of freshly formed (virgin) martensite, retained delta ferrite and retained austenite. As mentioned before, a distinction between bcc and bct is not visible when using in-situ XRD. On cooling, delta ferrite doesn't transform totally into austenite and therefore weak bcc peaks never disappear. Due to this, delta ferrite remains in the sample after cooling to room temperature.

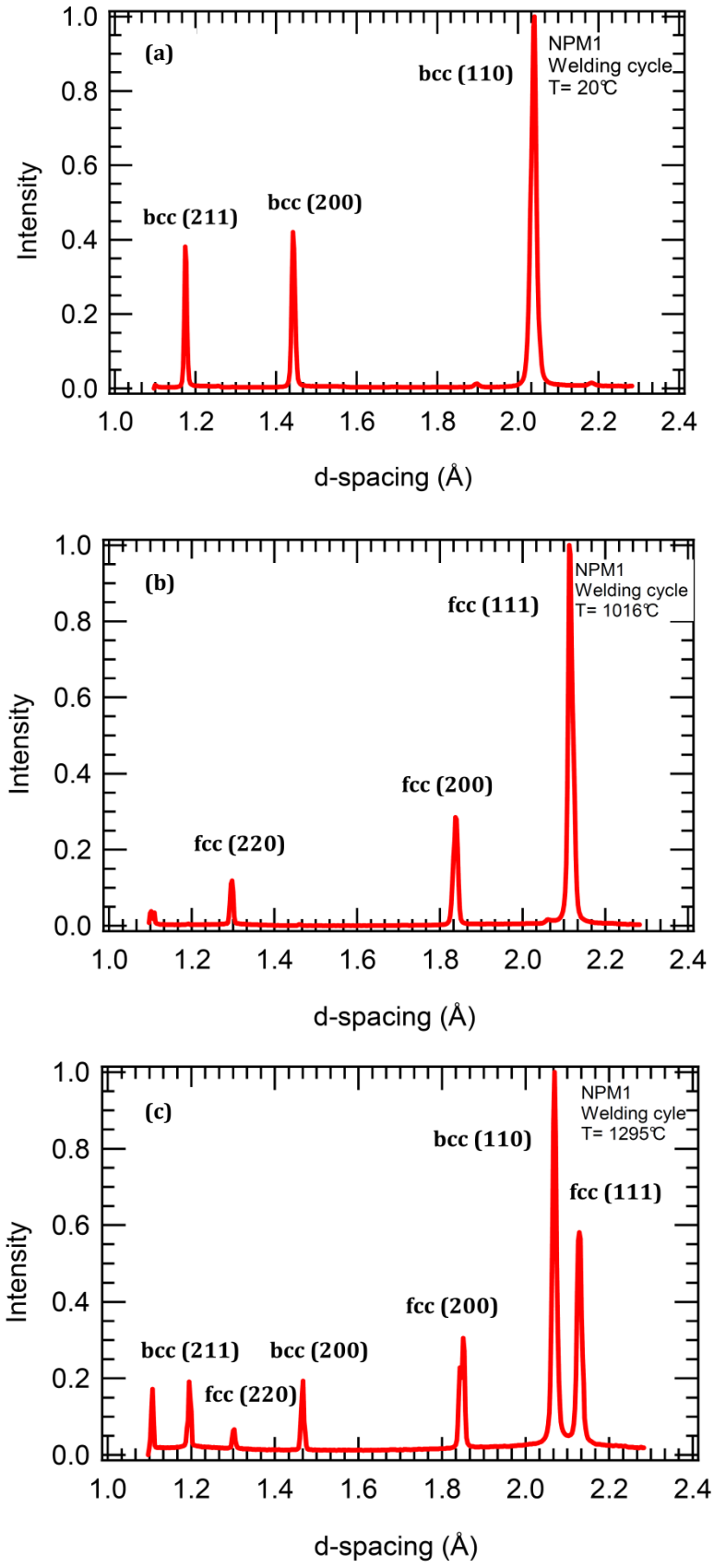


**Figure 37: In-situ X-ray diffraction patterns of NPM1 at several temperatures during the fast welding cycle(100 K $s^{-1}$) (a) initial base material at 20°C, (b) 1016°C on heating, (c) 1295°C on heating.**

### 5.2.4.3 NPM4

*Slow welding cycle with a peak temperature of 1300°C*

The welding cycle of the 9% Cr steel NPM4 is simulated with a heating rate of 10 K $s^{-1}$ up to a peak temperature of 1300°C, followed by a free cooling to room temperature. The initial material before heating exhibits a tempered martensitic microstructure. Heating up to 912°C shows that the tempered martensite starts to transform into austenite which indicates the $A_{C1}$. 1010°C possesses a complete microstructure of austenite, as the sample shows only bcc peaks. The precipitates completely dissolve between temperatures ranging from 1033°C to 1053°C. At 1170°C, the intensity of the ferrite peaks increases resulting in the onset of delta ferrite formation. On cooling, delta ferrite starts to transform into austenite, and the martensite start temperature is around 512°C. The received martensite phase finish temperature is around 273°C. In the as-welded condition, the HAZ microstructure is characterised by fresh formed martensite. The austenite phases however remain from the incomplete transformation of austenite into martensite.

*Slow welding cycle with a peak temperature of 1100°C*

By applying a heating rate of 10 K $s^{-1}$ and a peak temperature of 1100°C, the XRD pattern shows that martensite transforms into austenite at 899°C. The NPM4 material reaches a complete austenite microstructure at 1024°C, and this is the so called $A_{C3}$ point. At a peak temperature of 1100°C, face-centred cubic peaks of austenite are still present. On cooling, the start of the martensite formation and the martensite phase finish temperature is determined. The austenite phase begins to transform into martensite at around 439°C, and the end of formation is reached around 254°C during cooling. The microstructure after welding reveals a martensitic microstructure with retained austenite. The chromium carbides are completely dissolved in the matrix between temperatures of 1047°C and 1056°C.

### 5.2.4.4 Conclusions

*Phase transformations*

The initial base material for all used steels exhibits a martensitic microstructure with precipitates along the prior austenite grain boundaries and the martensite lath boundaries. The microstructure in the as-welded condition (high peak temperatures) of all 9-12% Cr steels consists of a martensitic microstructure with retained austenite and delta ferrite (δ). The two welding cycles with the lower peak temperatures 1050°C and 930°C, however, after performing the welding cycles, show a tempered martensitic microstructure with precipitates along the prior austenite grain boundaries and the martensite lath boundaries. The formation of delta ferrite is observed by heating it up to higher temperatures above $A_{C3}$. By applying a heating rate of 100 K $s^{-1}$, it becomes obvious that the austenite start and end temperature are not determined. Therefore the obtained phase transformation temperatures on heating during the slow welding cycle are listed in Table 19. On the basis of these data, a correlation of the results is observed. The austenite start and finish temperatures are within the same range for all steels. The martensite start and finish temperatures of NPM1 and NPM4 are higher than that of CB2A, as its higher carbon suppresses the martensite phase transformation temperatures. In Table 19, the obtained phase transformation temperatures during the performed welding cycles with different heating rates and peak temperatures are summarised.

**Table 19: Summary of phase transformation temperatures during welding cycles of the used three 9% Cr steels.**

| Specimen | Heating rate [K $s^{-1}$] | $T_P$ [°C] | $A_{C1}$ [°C] | $A_{C3}$ [°C] | $M_S$ [°C] | $M_F$ [°C] |
|---|---|---|---|---|---|---|
| CB2A (A8)* | 100 | 1300 | n.d.[5] | n.d.[5] | 410 | 150 |
| CB2A (A2)* | 10 | 1300 | 900 | 1016 | 400 | 152 |
| NPM1 (N2)* | 100 | 1050 | n.d.[5] | n.d.[5] | 426 | 256 |
| NPM1 (N2)* | 100 | 930 | n.d.[5] | n.d.[5] | 430 | 247 |
| NPM1 (N5)* | 10 | 1300 | 924 | 1076 | 433 | 224 |
| NPM4 (M1)* | 10 | 1300 | 912 | 1010 | 512 | 273 |
| NPM4 (M2)* | 10 | 1100 | 899 | 1024 | 439 | 254 |

[5] n.d. ..... not determinable due to the fast heating rate

*Precipitates behaviour*

In the used 9% Cr steels, the complete dissolution process of the $M_{23}C_6$ precipitates during the welding cycles with high peak temperatures is observed. Table 20 shows averages values and the associated standard deviations of the dissolution temperatures of the Cr carbides $M_{23}C_6$ during welding cycles are summarised. The NPM4 welding cycle have been performed using a free cooling in contrary to the other samples. In spite of that, no significant variation of dissolution temperatures is observed. The dissolution of precipitates leads to enrichment of the element carbon in the matrix and thus a suppression of the martensite start temperatures is observed. On the basis of these obtained results, the dissolution temperatures of 9Cr-3W-3Co-VNbBN and modified 9Cr-1Mo steels with the equal welding conditions are within the same range.

**Table 20: Summary of the dissolution temperatures of the precipitates during the welding cycles of the used three 9% Cr steels.**

| Specimen | Heating rate [K $s^{-1}$] | Peak temperature [°C] | Cooling | $M_{23}C_6$ dissolution temperature [°C] |
|---|---|---|---|---|
| CB2A (A8)* | 100 | 1300 | $t_{8/5}$ = 43 s | 1134 ± 46 |
| CB2A (A2)* | 10 | 1300 | 10 K $s^{-1}$ | 1061 ± 21 |
| NPM1 (N4)* | 10 | 1300 | 10 K $s^{-1}$ | 1061 ± 21 |
| NPM4 (M1)* | 10 | 1300 | free cooling | 1043 ± 14 |
| NPM4 (M2)* | 10 | 1100 | free cooling | 1051 ± 6 |

The post-weld heat treatment leads to a re-precipitation of the dissolved precipitates during welding along the prior austenite grain boundaries and martensite lath boundary. In CB2A, after the fast welding cycle, the $M_{23}C_6$ re-precipitates between 500°C and 530°C on heating during the post-weld heat treatment. By performing post weld heat treatment, the phases of matrix does not show significant changes.

# 6 Summary

In this present work, the microstructural evolution of the heat-affected zone (HAZ) in three 9% Cr steels has been investigated. Special attention has been paid to the precipitates' behaviour during thermal treatments and precipitates are known to be excellent creep contributors.

The *base material* of all three 9% Cr steels in their as-received condition, after austenisation and tempering, display a similar microstructure. This microstructure consists of tempered martensite, with precipitates along the prior austenite grain and martensite lath boundaries. The tempered martensitic microstructure, in the as-received state, is verified using modern techniques such as light-optical microscopy, scanning electron microscopy and in-situ X-ray diffraction with synchrotron radiation. In-situ X-ray diffraction shows that the detected face-centred cubic precipitates peaks are of type $M_{23}C_6$. The micro hardness of all three base materials is within the same range.

By using *in-situ X-ray diffraction (XRD)*, along with synchrotron radiation and *dilatometry*, an investigation was carried out on the phase transformations. The obtained phase transformation temperatures are within the same range for the 9% Cr steels within the same welding conditions. It is observed that the simulated welding cycles with higher heating rates, in contrast to slow heating rates, shift the phase transformation to higher temperatures. The phase transformation temperatures obtained from X-ray diffraction confirm the results from dilatometry.

The *dissolution process of* $M_{23}C_6$ during welding cycles at high temperatures is observed in all three 9% Cr steels. A decrease of the martensite start temperatures is observed due to the enrichment of the element carbon in the matrix, which was caused by the dissolution of the precipitates. The investigated dissolution temperatures of CB2A-Heat 145, NPM1 and NPM4 with the equal welding conditions, are within the same range.

Post-weld heat treatment leads to a *re-precipitation* of the dissolved precipitates during welding along the prior austenite grain boundaries and martensite lath boundary. This is verified by optical microscopy and in-situ X-ray diffraction.

The *formation of delta ferrite* is observed at higher temperatures. Delta ferrite, with its skeletal network-shape, is observed as a bright zone between the martensitic lath blocks and on the prior austenite grain boundaries in all three 9% Cr steels.

The *micro hardness* of the heat-affected zone for all three 9% Cr steels after welding is higher in comparison to the initial base materials when in their as-received condition (i.e. normalising and tempering). Post-weld heat treatment of the HAZ reduces the micro hardness values of the steels, relative to that of the base material.

# 7 References

[1] **Abe, F, et al. 2004.** Stabilization of martensitic microstructure in advanced 9Cr steel during creep at high temperature. *Materials Science and Engineering A.* 2004, Vol. 378, pp. 299-303.

[2] **Rapouch, J, Bystrianský, J und Svobodová, M. 2011.** Detection of structural changes in chromium martensitic steels using electrochemical methods. *METAL.* 2011.

[3] **Danielsen, H K. 2007.** *Z-phase in 9-12% Cr steels.* Technical University of Denmark : s.n., 2007. Doctoral Thesis.

[4] **Holzer, I. 2010.** *Modelling and Simulation of Strengthening in Complex Martensitic 9-12% Cr and a Binary Fe-Cu Alloy.* Graz University of Technology : s.n., 2010. Doctoral Thesis.

[5] **Golañski, G. 2010.** Effect of the heat treatment on the structure and properties GX12CrMoVNbN9-1 cast steel. *Archives of Materials Science and Engineering.* 2010, Vol. 46, Issue.2, pp. 88-97.

[6] **Sonderegger, B. 2005.** *Charakterisierung der Substruktur in modernen Kraftwerkstoffen mittels der EBSD Methode.* Graz University of Technology : s.n., 2005. Doctoral Thesis.

[7] *A synchrotron diffraction study of transformation behaviour in 9 Cr steel using simulated weld heataffected zone conditions.* **Santella, M, et al. 2007.** [ed.] 7th International Charles Parsons Turbine Conference. United Kingdom : s.n., 2007.

[8] **Plimon, S W. 2004.** *Simulation einer grosstechnischen Wärmebehandlung und begleitende mikrostrukturelle Untersuchung an einem modernen 9-12% Cr Stahl.* Graz University of Technology : s.n., 2004. Master Thesis.

[9] **Rojas, J D. 2011.** *9-12% Cr heat resistant steels: alloy design. TEM characterization of microstructure evolution and creep response at 650°C.* Ruhr University of Bochum : s.n., 2011. Doctoral Thesis.

[10] **Oñoro, J. 2006.** Martensite microstructure of 9–12%Cr steels weld metals. *Journal of Materials Processing Technology.* 2006, Vol. 180, Issues 1-3, pp. 137-142 .

[11] **Hald, J. 2008.** Microstructure and long-term creep properties of 9-12% Cr steels. *International Journal of Pressure Vessels and Piping.* 2008, Vol. 85, pp. 30-37.

[12] **Cipolla, L. 2010.** *Conversion of MX Nitrides to Modified Z-Phase in 9-12%Cr Ferritic Steels.* Technical University of Denmark : s.n., 2010. Doctoral Thesis.

[13] **Danielsen, H K and Hald, J. 2006.** Behaviour of Z phase in 9-12%Cr steels. *Energy Materials.* 2006, Vol. 1, No.1.

[14] *Z-phase strengthened Martensitic 9-12%Cr steels.* **Hald, J and Danielsen, H K. 2009.** [ed.] Symposium on Heat Resistant Steels and Alloys for High Efficiency USC Power Plants. Japan : s.n., 2009.

[15] **Danielsen, H K and Hald, J. 2009.** On the nucleation and dissolution process of Z-phase Cr(V.Nb)N in martensitic 12%Cr steels. *Materials Science and Engineering A.* 2009, Vol. 505, pp. 166-177.

[16] **Cipolla, L, et al. 2010.** Conversion of MX nitrides to Z-phase in a martensitic 12% Cr steel. *Acta Materialia.* 2010, Vol. 58, pp. 669-679.

[17] **Dimmler, G. 2003.** *Quantifizierung der Kriech- und Zeitstandfestigkeit von 9-12% Cr Stählen auf mikrostruktureller Basis.* Graz University of Technology : s.n., 2003. Doctoral Thesis.

[18] **Maile, K. 2007.** Evaluation of microstructural parameters in 9-12% Cr steels. *International Journal of Pressure Vessels and Piping.* 2007, Vol. 84, pp. 62-68.

[19] *Experimental and Numerical Study of Crack Growth in the Heat-Affected-Zone of a Ferritic Steel Weldment.* **Moskovic, R, O'Dowd, N and Flewitt, P. 2003.** [ed.] Transactions of the 17th International Conference on Structural Mechanics in Reactor Technology (SMiRT 17) Czech Republic: s.n., 2003.

[20] **Takagi, Y and Otsuki, S. 2004.** Creep-fatigue characteristics of partial repair welds and full repair welds on aged 2.25Cr-1Mo steel. *OMMI.* 2004, Vol. 3, Issue 1.

[21] **Mayr, P. 2007.** *Evolution of microstructure and mechanical properties of the heat-affected zone in B-containing 9% chromium steels.* Graz University of Technology : s.n., 2007. Doctoral Thesis.

[22] **2011.** ArcelorMittal. [Online] 2011. [Cited: October 2, 2011.] http://arcelormittal.com/fce/repository/PDF-technical-chapters/Prcat_Welding.pdf.

[23] **Magnusson, H. 2010.** *Creep modelling of particle strengthened steels.* Royal Institute of Technology, : s.n., 2010. Doctoral Thesis.

[24] **Wang, X, et al. 2009.** High-temperature creep properties of fine grained heataffected zone in P92 weldment. *Transactions of Nonferrous Metals Society of China.* 2009, Vol. 19, pp. 772-775.

[25] **Tabuchi, M, et al. 2004.** Improvement of type IV creep cracking resistance of 9Cr heat resisting steels by boron addition. *OMMI.* 2004, Vol. 3, Issue.3.

[26] **Muratoglu, M and Eroglu, M. 2011.** Effect of molybdenum on the intercritical heat-affected zone of the low carbon Cr-Mo steels. *Asian Transactions on Engineering.* 2011, Vol. 1, Issue.4.

[27] **Komizo, Y, Terasaki, H and Yonemura, M. 2005.** In-situ Observation of Steel Weld Solidification and Phase evolution using Synchrotron Radiation. *Transactions of JWRI.* 2005, Vol. 34, Issue 2.

[28] *In-Situ Observations of Phase Transformations During Welding of 1045 Steel using Spatially Resolved and Time Resolved X-Ray Diffraction.* **Elmer, J W, Palmer, T A and DebRoy, T. 2006.** [ed.] Welding and Advanced Solidification Processes XI Modeling of Casting. France : s.n., 2006.

[29] **Elmer, J W, Palmer, T A and Specht, E D. 2007.** In situ observations of sigma phase dissolution in 2205 duplex stainless steel using synchrotron X-ray diffraction. *Materials Science and Engineering A.* 2007, Vol. 459, pp. 151-157.

[30] **Schmoelzer, T, et al. 2011.** The Contribution of High-Energy X-Rays and Neutrons to Characterization and Development of Intermetallic Titanium Aluminides. *Advanced Engineering Materials.* 2011, Vol. 13, Issue 8, pp. 685–699.

[31] *Synchrotron X-rays for structural characterization of stainless steels.* **Hedström, P and Odén, M. 2008.** *[ed.] Proceedings of the 6th European Stainless Steel Conference. Finland : s.n., 2008.*

[32] COST | Home. *European Cooperation in Science and Technology.* [Online] [Cited: October 9, 2011.] http://www.cost.esf.org/.

[33] Bähr Thermoanalyse. [Online] [Cited: November 3, 2011.] http://www.baehr-thermo.de/Download/Uk/Dilatometer.pdf.

[34] *Axio Observer - Carl Zeiss.* [Online] [Cited: October 5, 2011.] http://www.zeiss.com/industry/axioobserver_brochure.pdf.

[35] **2011.** VEGA SEM - TESCAN, as. [Online] October 5, 2011. http://www.tescan.com/product.php?id_menu=20&id=32&name=VEGA+3+SB

[36] **Cerjak, H. 2008.** *Skriptum Werkstoffkunde. Institute for Materials Science and Welding, TU Graz,* 2008.

[37] *Advanced Techniques for In-Situ Monitoring of Phase Transformations During Welding Using Synchrotron-Based X-Ray Diffraction.* **Elmer, J W, et al. 2005.** [ed.] 7th International Trends in Welding. United States : s.n., 2005.

[38] **Vander Voort, G F.** *buehler.* [Online] [Cited: October 11, 2011.] http://www.buehler.com/application_support/MartensiteRetainedAusteniteIHApril2009.pdf.

[39 ] **Foroozmehr, F, Najafizadeh, A and Shafyei, A. 2011.** Effects of carbon content on the formation of nano/ultrafine grained low-carbon steel treated by martensite process. *Materials Science and Engineering A.* 2011, Vol. 528, Issue. 18, pp. 5754–5758.

[40] **Mayr, P, et al. 2008.** Direct observation of phase transformations in the simulated heat-affected zone of a 9Cr martensitic steel. *International Journal of Materials Research.* 2008, Vol. 99, pp. 381-384.

[41] *Private communication* with Professor **Mayr, P.**

[42] *Experience with 9Cr3W3CoVNbBN Base Material and Crosswelds at 650°C for Implementation in USC Power Plants.* **Mayr, P., et al. 2009.** [ed.] NIMS. Tsukuba, Japan : NIMS, 2009. 3rd Symposium on Heat Resistant Steels and Alloys for High Efficiency USC Power Plants 2009.

[42] **Magner, S H, et al. 2002.** A historical review of retained austenite and its measurement by X-ray diffraction. *Advances in Xray Analysis.* 2002, Vol. 45, Issue c, pp. 92-97.

[43] **Payares-ASPRINO, M C, Katsumoto, H and Liu, S. 2008.** Effect of martensite start and finish temperature on residual stress development in structural steel welds. *Welding Journal.* 2008, Vol. 87, No. 11, pp. 279-289.

[44] Sub-zero Treatment of Steels. *Technology/Processes/Equipment.* [Online] [Cited: October 10, 2011.] http://www.lindegas.de/international/web/lg/de/like35lgde.nsf/repositorybyalias/pdf_subzero_treatment/$file/Subzero_Treatment_of_Steels_en.pdf

[46 ] **Sadrawetz, F. 2010.** *Charakterisierung der Wärmeeinflusszone borlegierter 9 % Chromstähle.* Graz University of Technology : s.n., 2010. Master Thesis.

# Appendix

## A Optical Micrographs

*Appendix A shows further obtained optical micrographs of the base material and of the heat-affected zone. This section relates to chapters 5.1.1 and 5.2.2.*

## B Microhardness Results

*Appendix B is related to chapter 5.1.3 and show further hardness micrographs of the base material of the three 9% Cr steels.*

## C In-situ X-ray Diffraction

*Appendix C shows the X-ray diffraction pattern with the identified body-centred cubic peaks of the NPM4 and CB2A base materials. Furthermore the $Cr_{23}C_6$ reference with the data is shown. This part is related to chapter 5.1.4.*

# Appendix A: Optical micrographs of the base materials


**Figure 1: Base material CB2A.**


**Figure 2: Base material NPM1.**


**Figure 3: Base material NPM1.**


**Figure 4: Base material NPM4.**


**Figure 5: Base material NPM4.**


**Figure 6: Base material NPM4.**

# Appendix A: Optical micrographs of the heat-affected zone (HAZ)

## CB2A

*Fast welding cycle with a heating rate of 100 K $s^{-1}$ to a peak temperature of 1300°C and cooling time of $t_{8/5}$= 43 s*


**Figure 7: CB2A quenched at 1100°C.**


**Figure 8: CB2A quenched at 1165°C.**

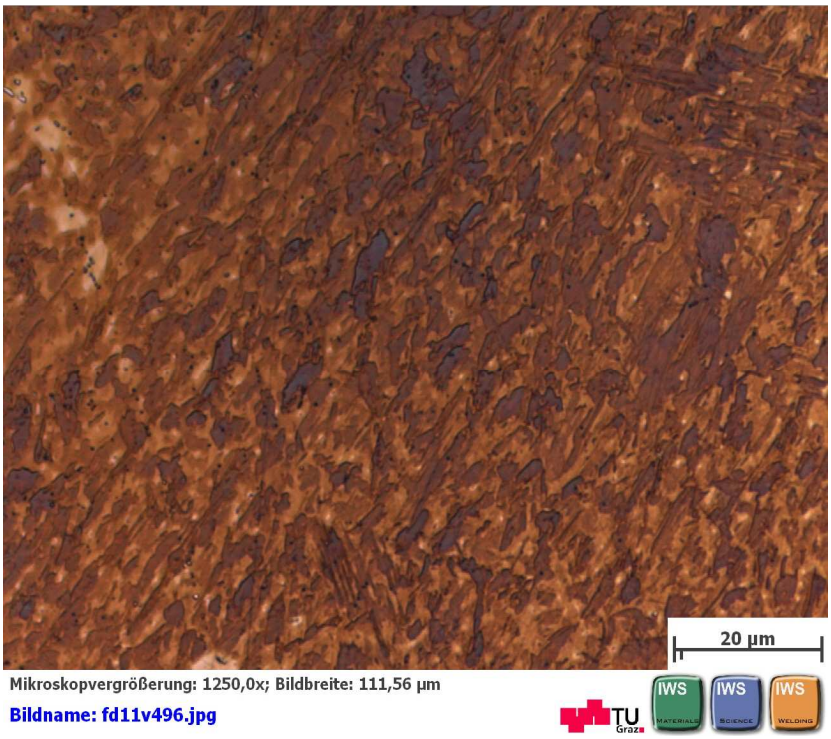


**Figure 9: CB2A quenched at 1195°C.**


**Figure 10: CB2A quenched at 1250°C.**


**Figure 11: CB2A quenched at 1300°C.**

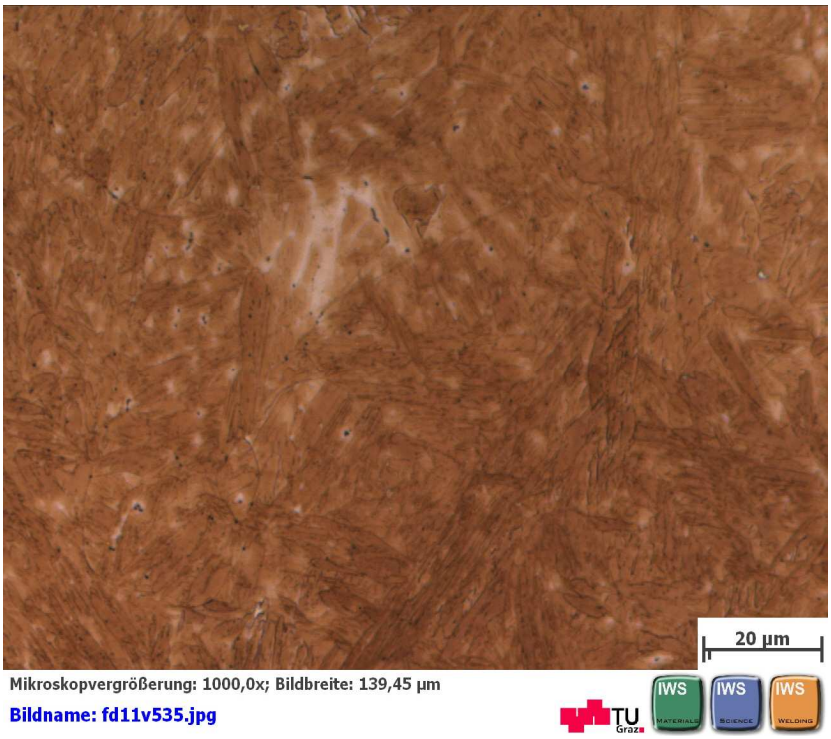


**Figure 12: CB2A in the as-welded condition.**

*PWHT after fast welding cycle*

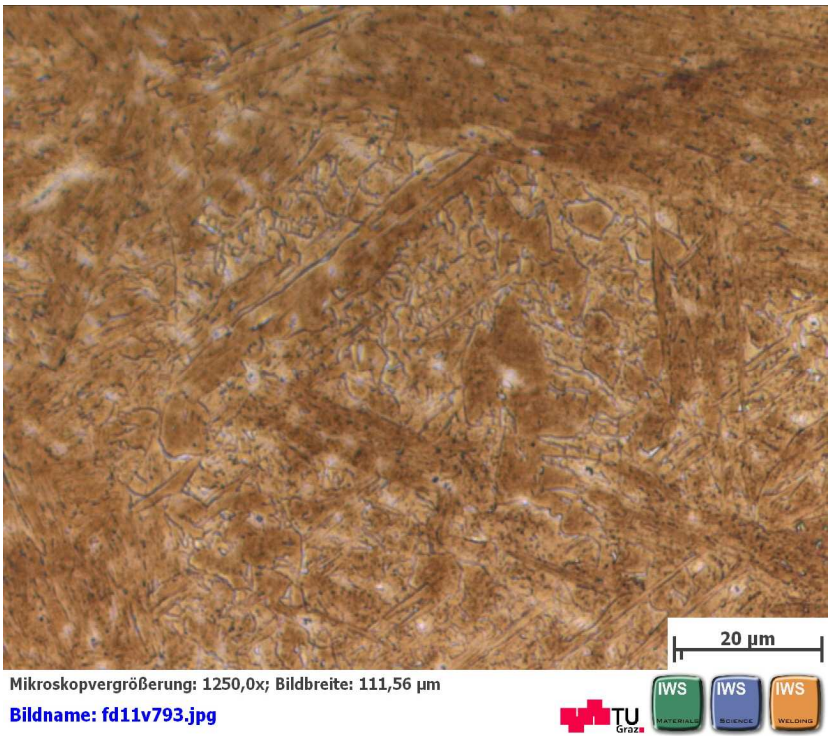


**Figure 13: CB2A quenched at 500°C.**

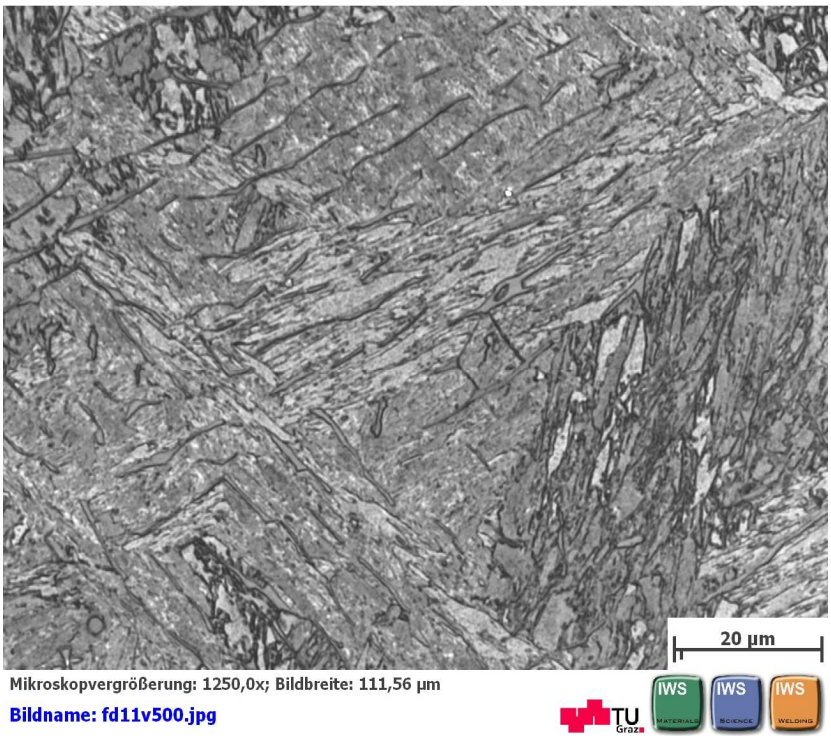


**Figure 14: CB2A quenched at 580°C.**

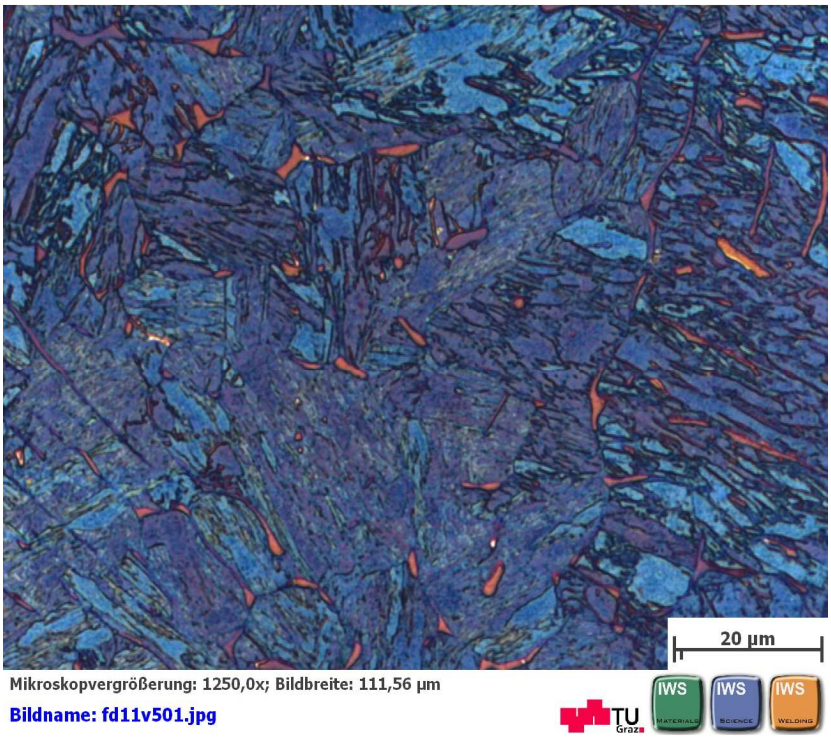


**Figure 15: CB2A quenched at 580°C.**


**Figure 16: CB2A quenched at 580°C.**

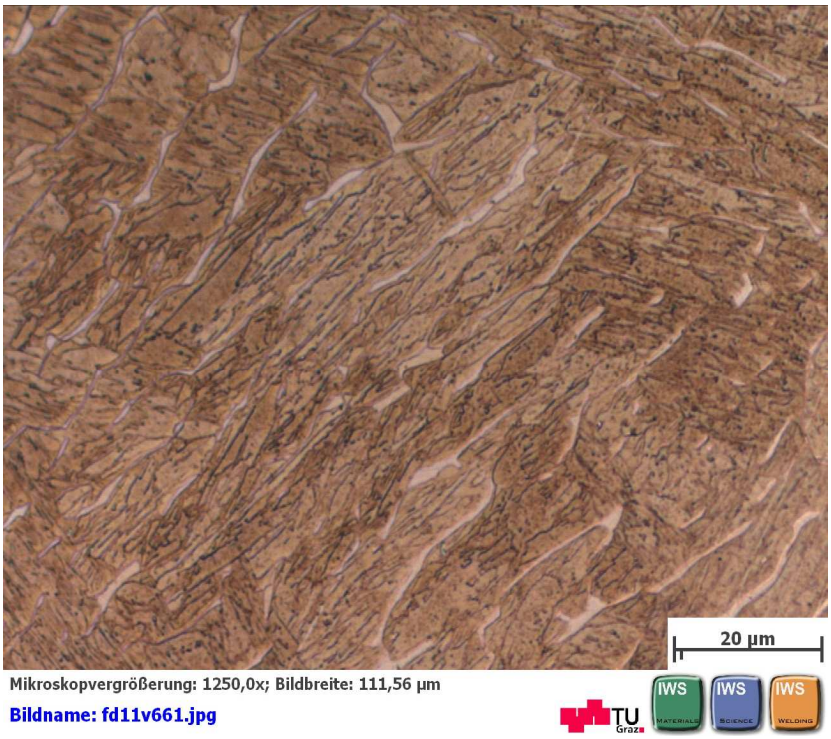


**Figure 17: CB2A quenched at 580°C.**


**Figure 18: CB2A quenched at 600°C.**


**Figure 19: CB2A quenched at 650°C.**


**Figure 20: CB2A quenched at 730°C.**


**Figure 21: CB2A after PWHT.**

*Slow welding cycle with a heating and cooling rate of 10 K $s^{-1}$ and with a peak temperature of 1300°C*


**Figure 22: CB2A quenched at 925°C.**


**Figure 23: CB2A quenched at 1046°C.**


**Figure 24: CB2A quenched at 1076°C.**

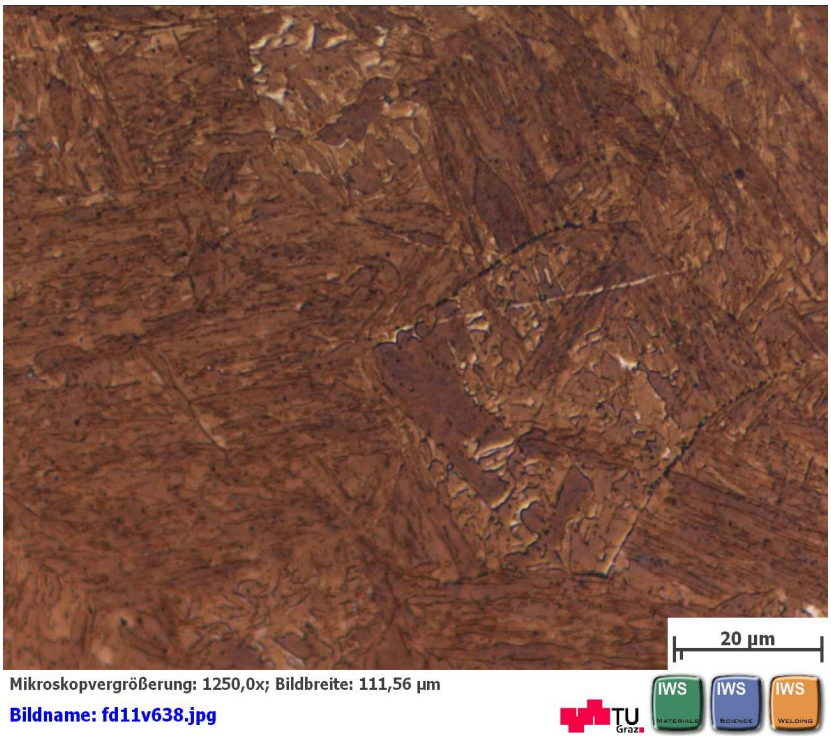


**Figure 25: CB2A quenched at 1165°C.**


**Figure 26: CB2A quenched at 1196°C.**

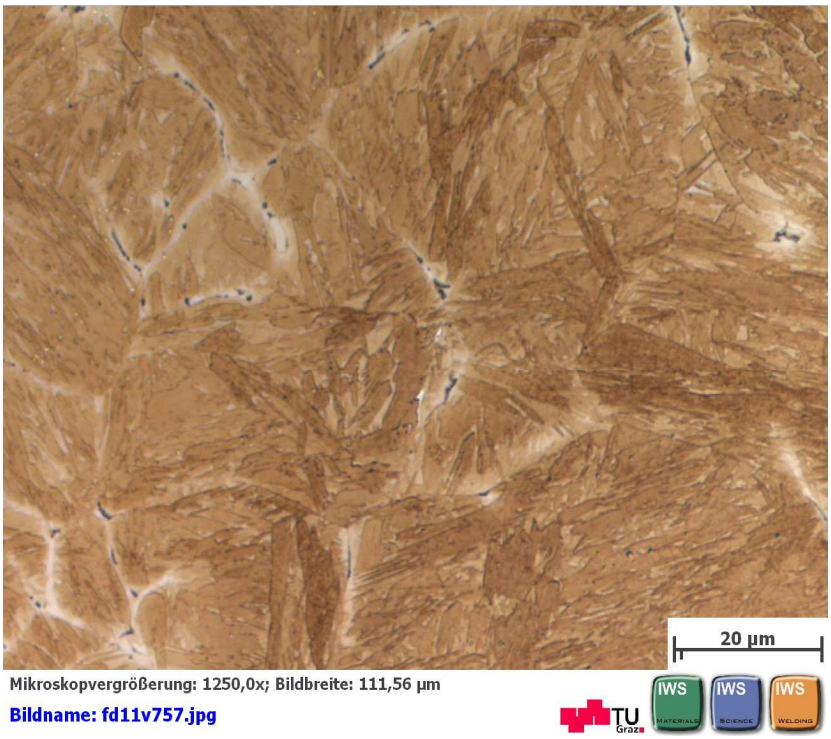


**Figure 27: CB2A in the as-welded condition.**


**Figure 28: CB2A in the as-welded condition.**

**NPM1**

*Fast welding cycle with a heating rate of 100 K $s^{-1}$ to a peak temperature of 1050°C and cooling time of $t_{8/5}$= 43 s*

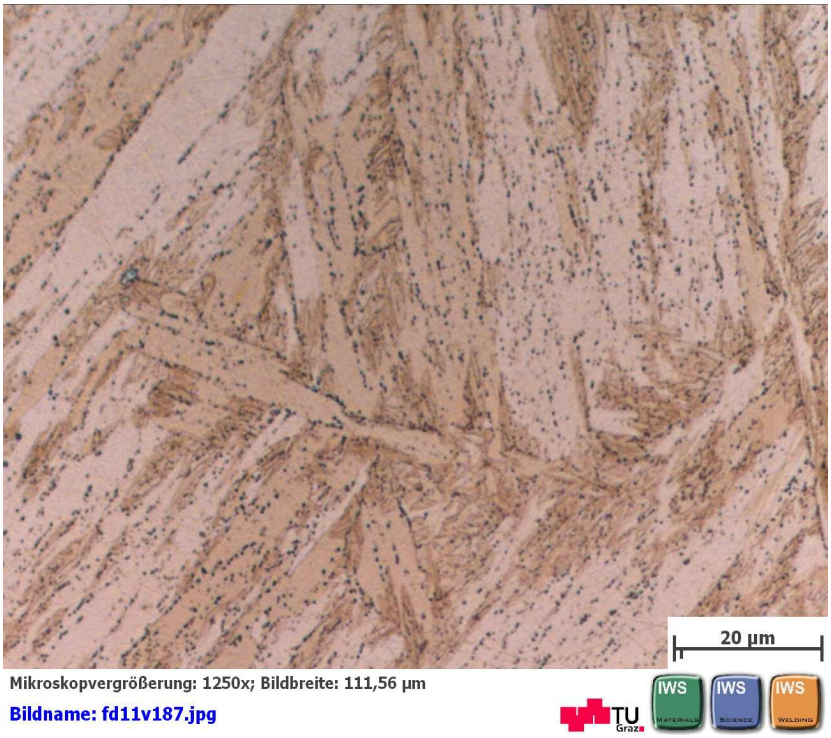


**Figure 29: NPM1 quenched at 950°C.**


**Figure 30: NPM1 quenched at 980°C.**


**Figure 31: NPM1 quenched at 1050°C.**


**Figure 32: NPM1 quenched at 1050°C.**


**Figure 33: NPM1 in the as-welded condition.**

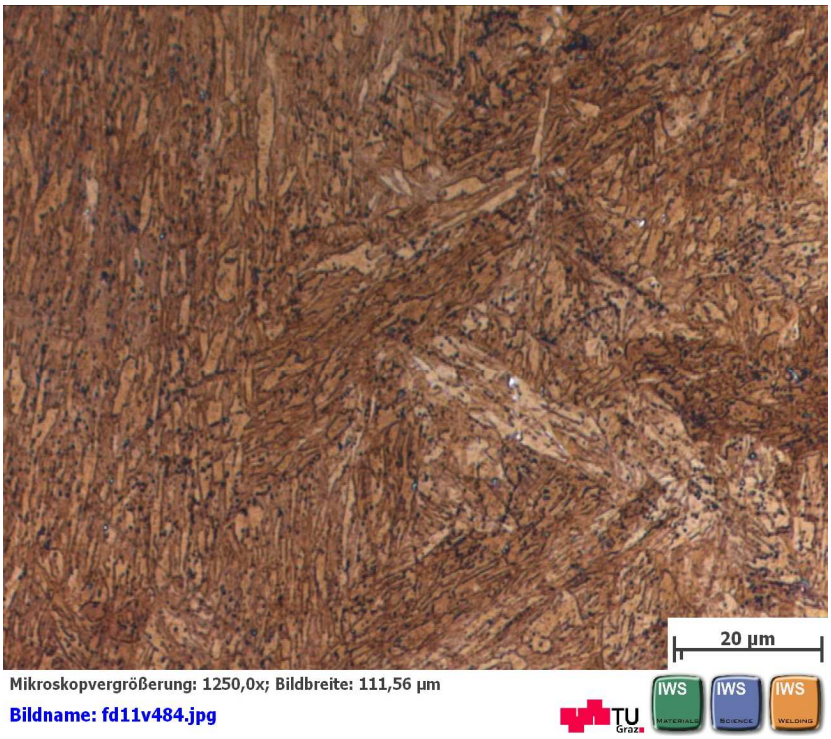


**Figure 34: NPM1 in the as-welded condition.**

*PWHT after fast welding cycle*

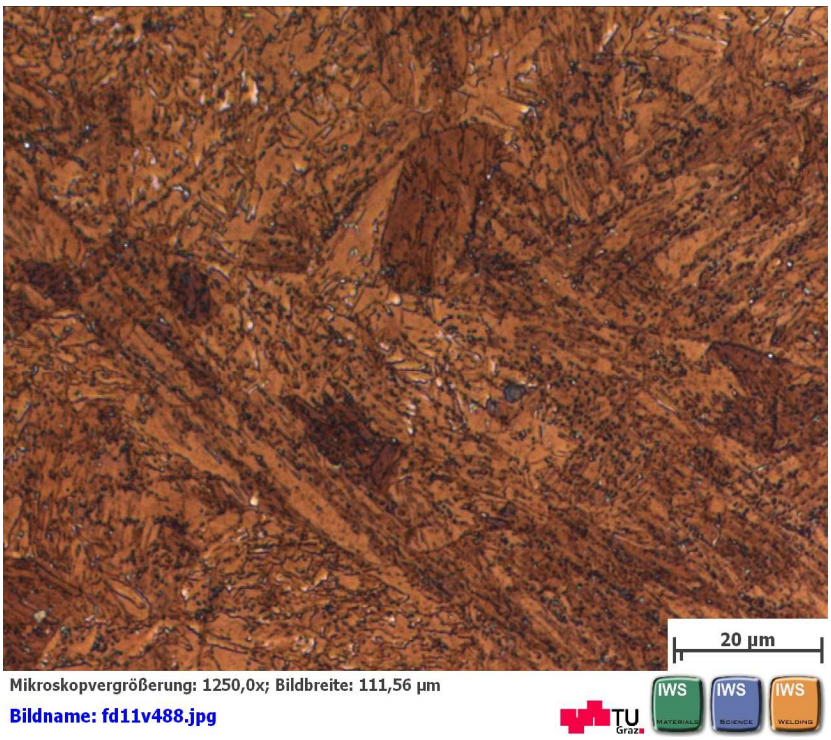


**Figure 35: NPM1 quenched at 517°C.**


**Figure 36: NPM1 quenched at 566°C.**


**Figure 37: NPM1 quenched at 650°C.**


**Figure 38: NPM1 quenched at 650°C.**

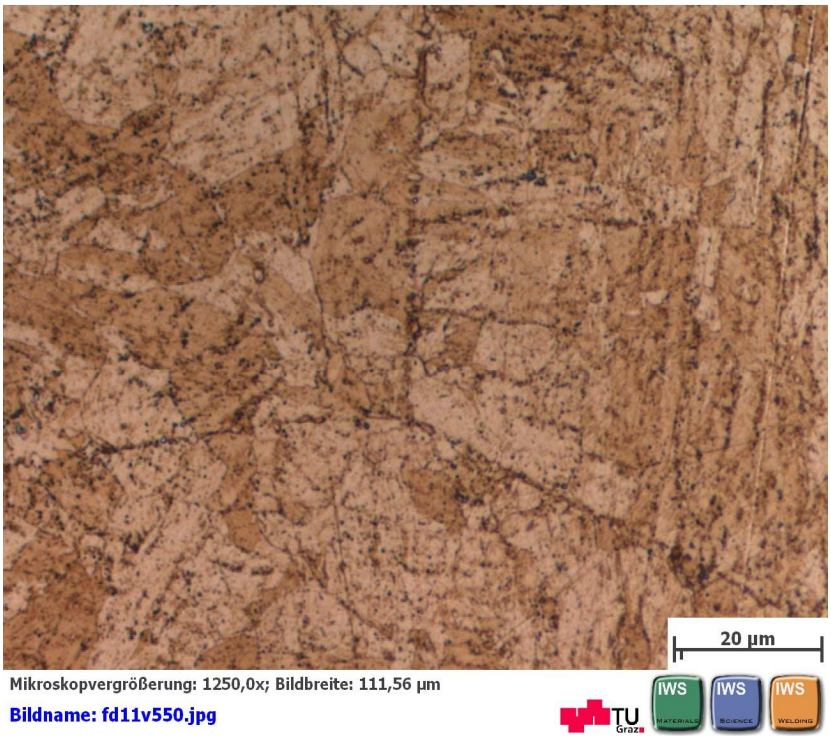


**Figure 39: NPM1 quenched at 730°C.**


**Figure 40: NPM1 quenched at 730°C.**

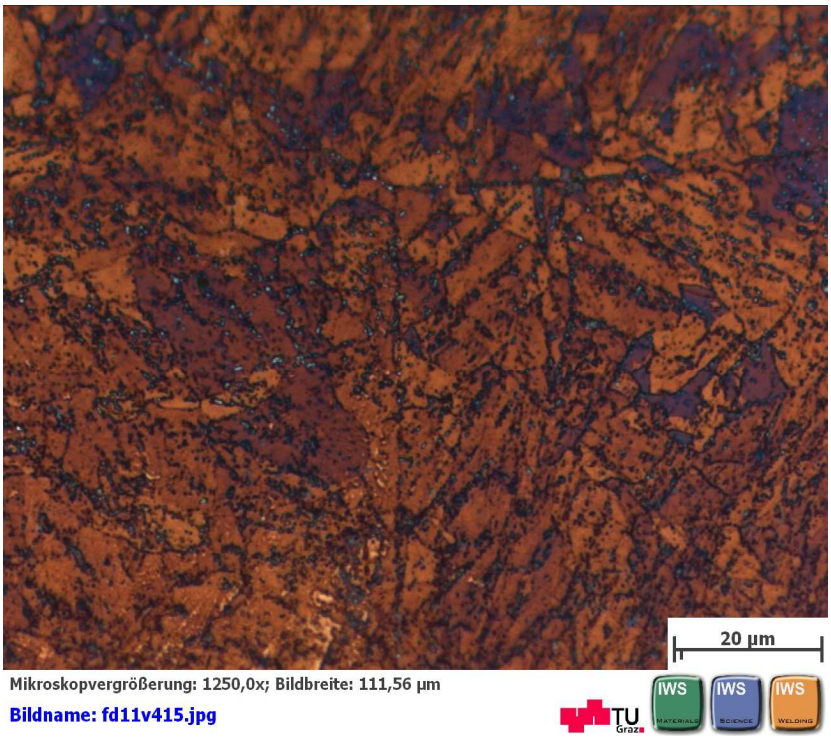


**Figure 41: NPM1 after PWHT.**


**Figure 42: NPM1 after PWHT.**

*Slow welding cycle with a heating and cooling rate of 10 K $s^{-1}$ and with a peak temperature of 1300°C*


**Figure 43: NPM1 quenched at 1046°C.**


**Figure 44: NPM1 quenched at 1166°C.**

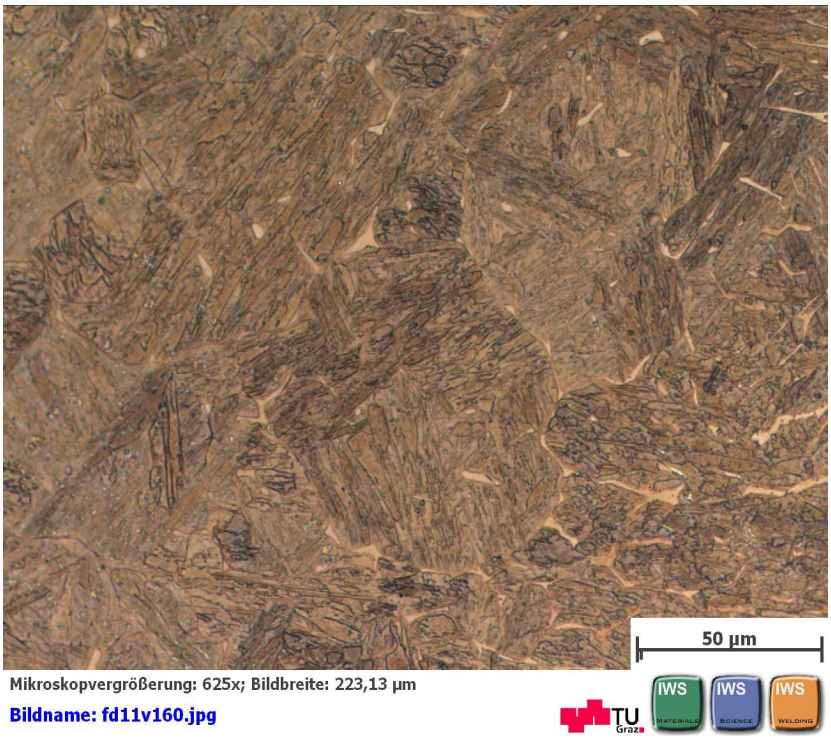


**Figure 45: NPM1 in the as-welded condition.**

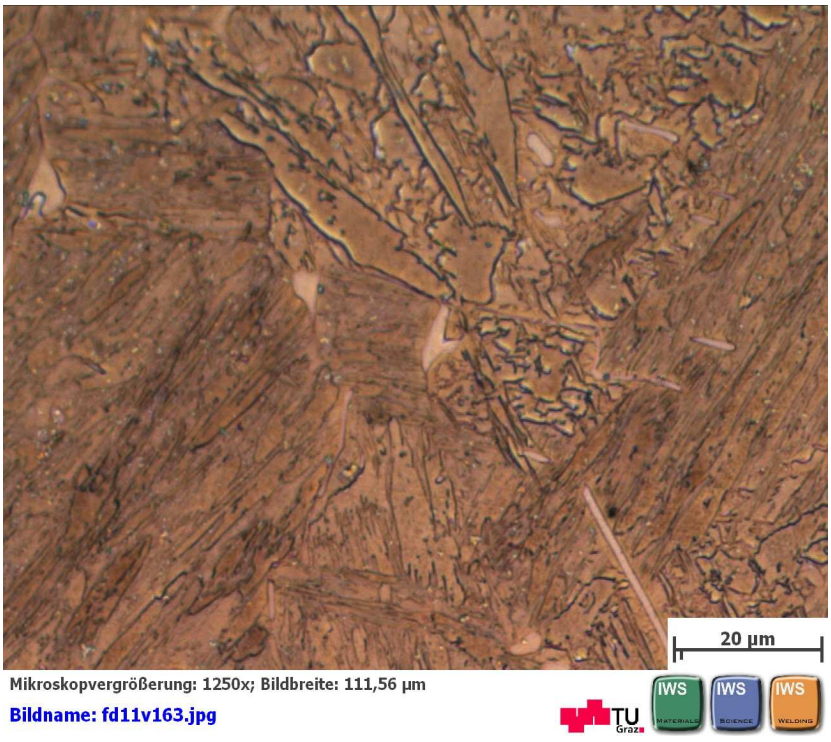


**Figure 46: NPM1 in the as-welded condition.**

**NPM4**

*Slow welding cycle with a heating of 10 K $s^{-1}$. a peak temperature of 1300°C and free cooling to room temperature*


**Figure 47: NPM4 quenched at 900°C.**


**Figure 48: NPM4 quenched at 1100°C.**


**Figure 49: NPM4 quenched at 1100°C.**

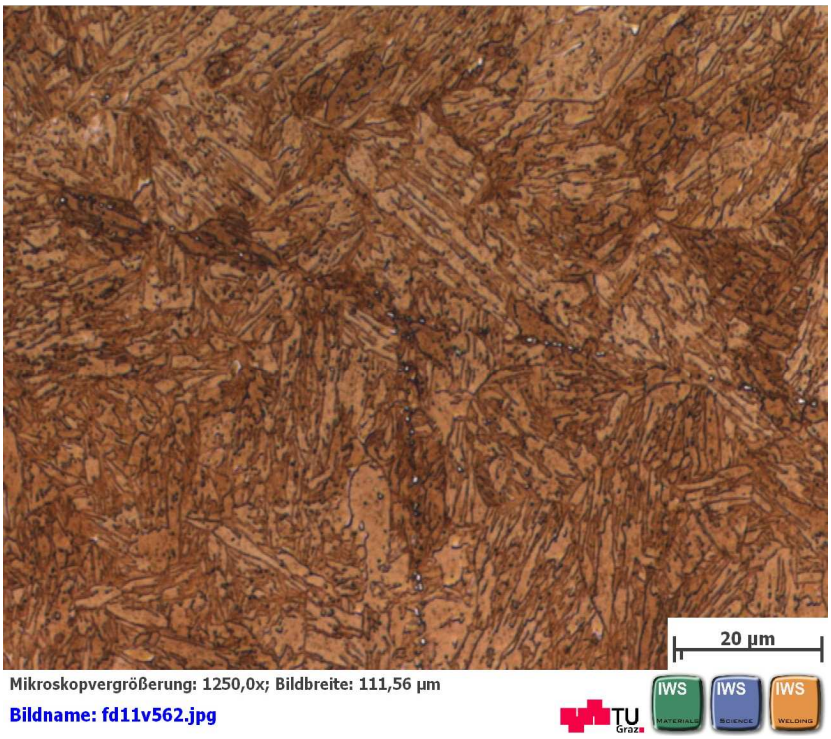


**Figure 50: NPM4 quenched at 1100°C.**


**Figure 51: NPM4 quenched at 1200°C.**

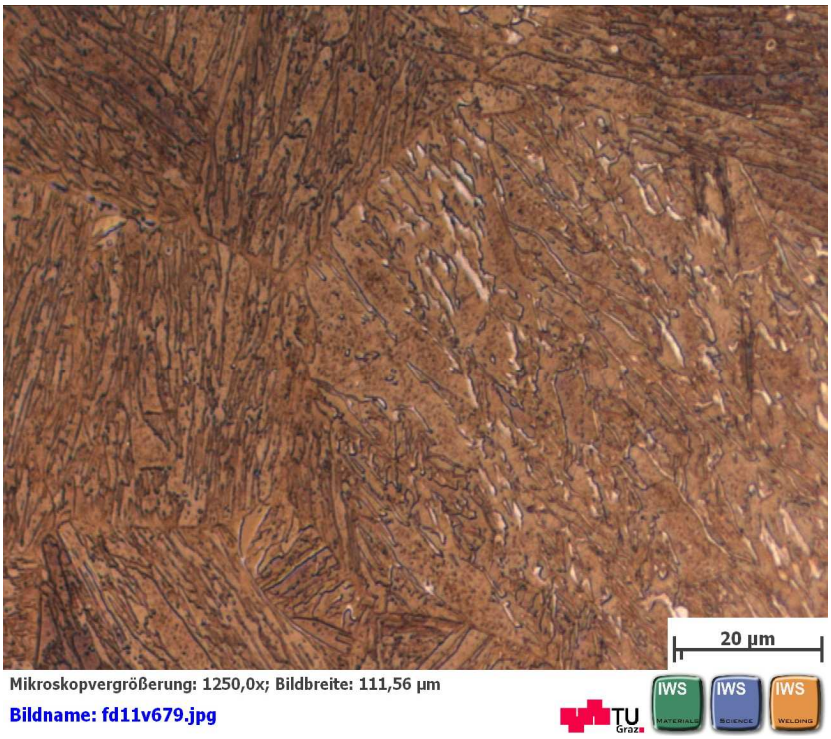


**Figure 52: NPM4 quenched at 1200°C.**


**Figure 53: NPM4 in the as-welded condition.**

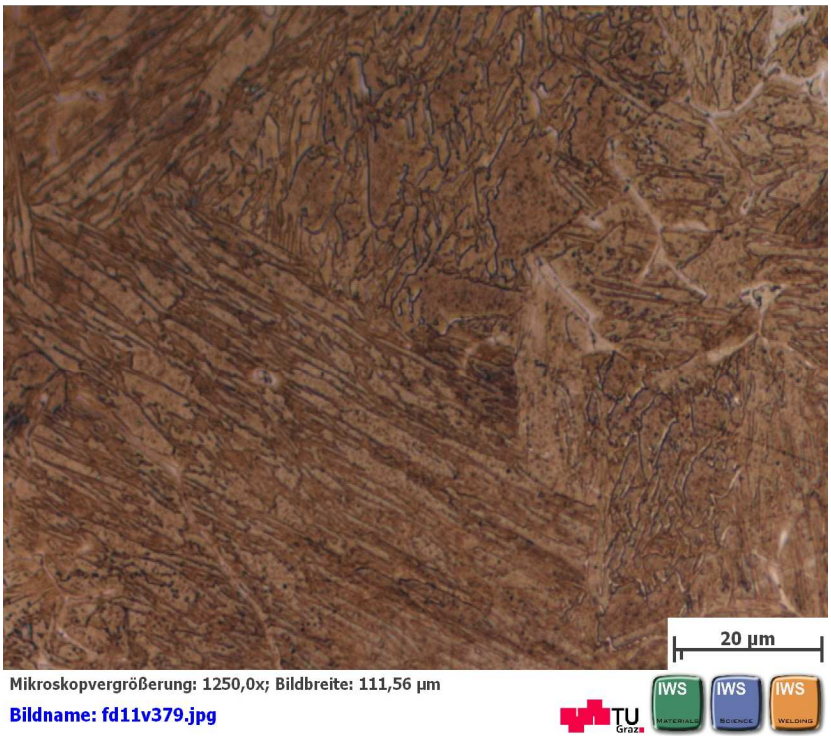


**Figure 54: NPM4 in the as-welded condition.**

## Appendix B: Hardness micrographs of the base materials

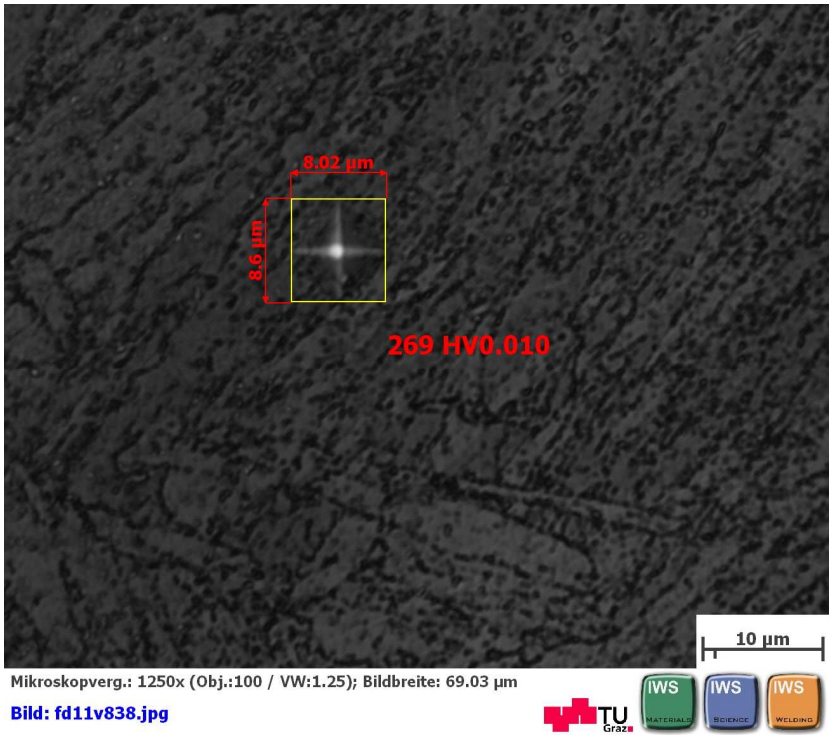


**Figure 55: Hardness micrograph of CB2A in the as-received condition.**

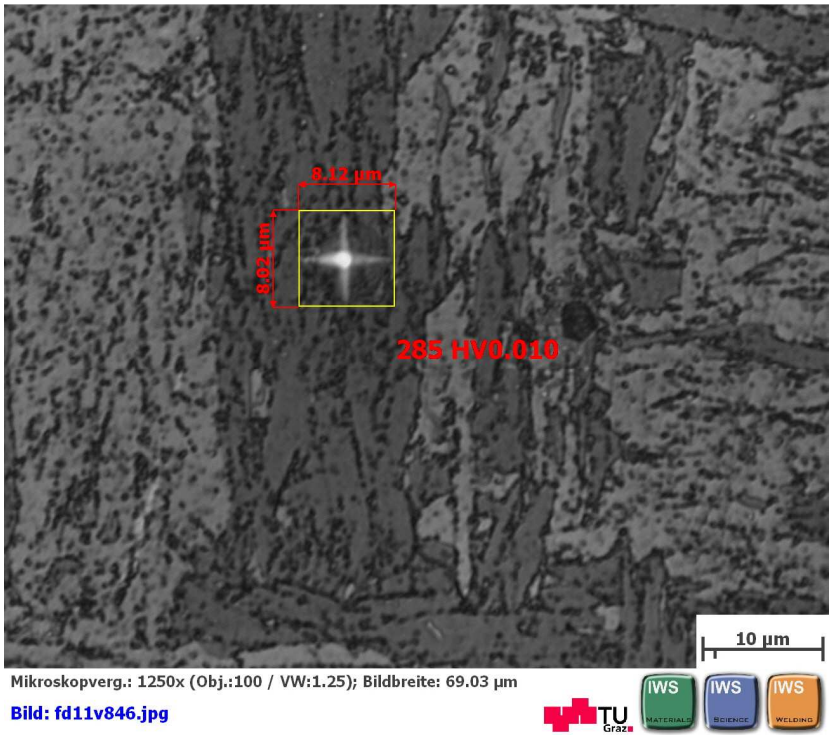


**Figure 56: Hardness micrograph of NPM1 in the as-received condition.**

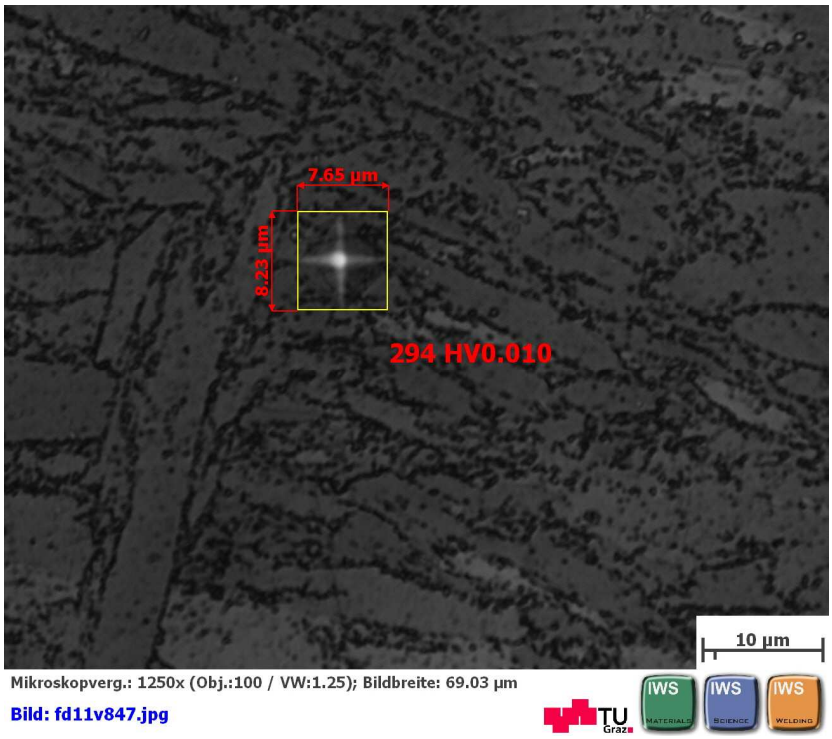


**Figure 57: Hardness micrograph of NPM1 in the as-received condition.**

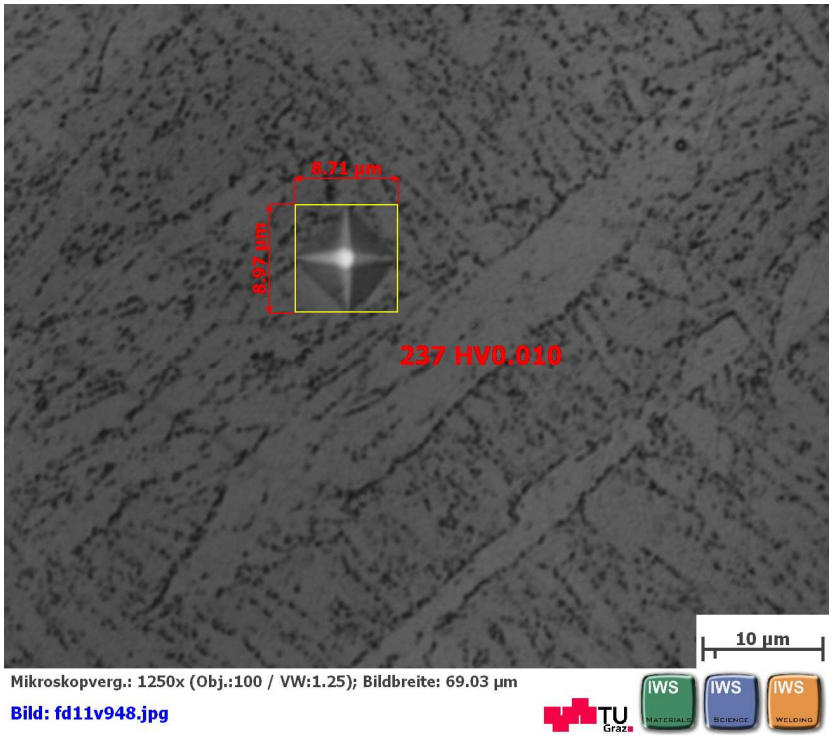


**Figure 58: Hardness micrograph of NPM1 in the as-received condition.**

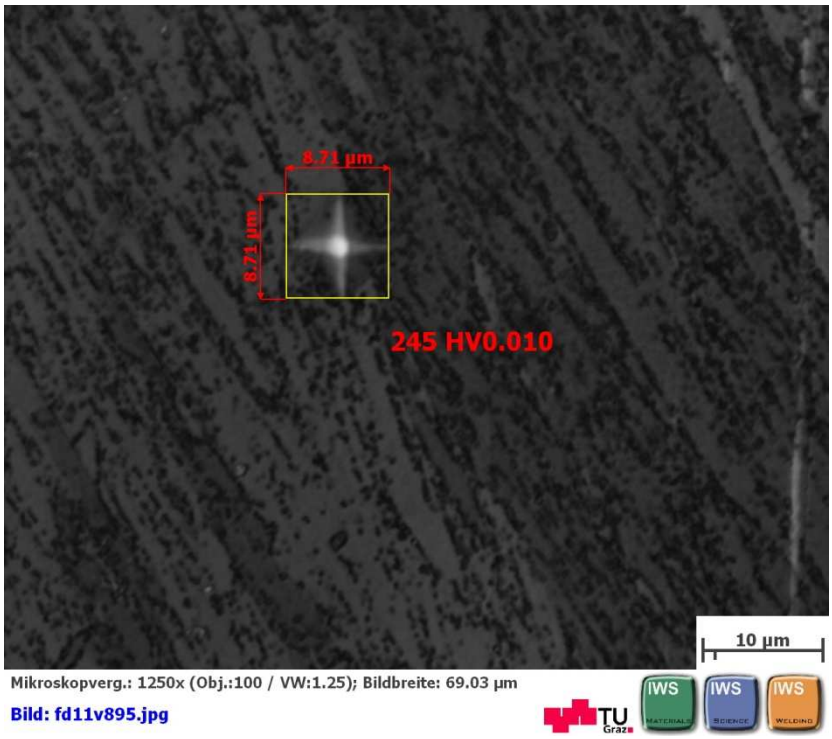


**Figure 59: Hardness micrograph of NPM4 in the as-received condition.**

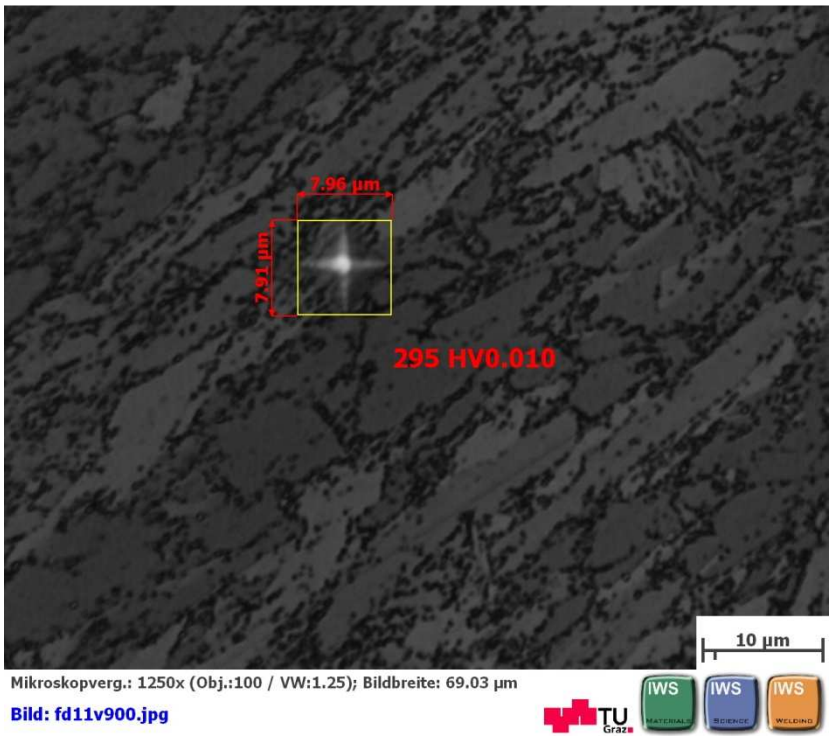


**Figure 60: Hardness micrograph of NPM4 in the as-received condition.**

## Appendix C: Base material characterisation by in-situ X-ray diffraction

The X-ray diffraction results obtained show that the base material consists of body-centred cubic peaks and these are characterised by lattice planes α(200). α(211) and α(111).
In Figure 57 and 58 the X-ray diffraction pattern with the identified bcc peaks of the base material of NPM4 and CB2A are shown.

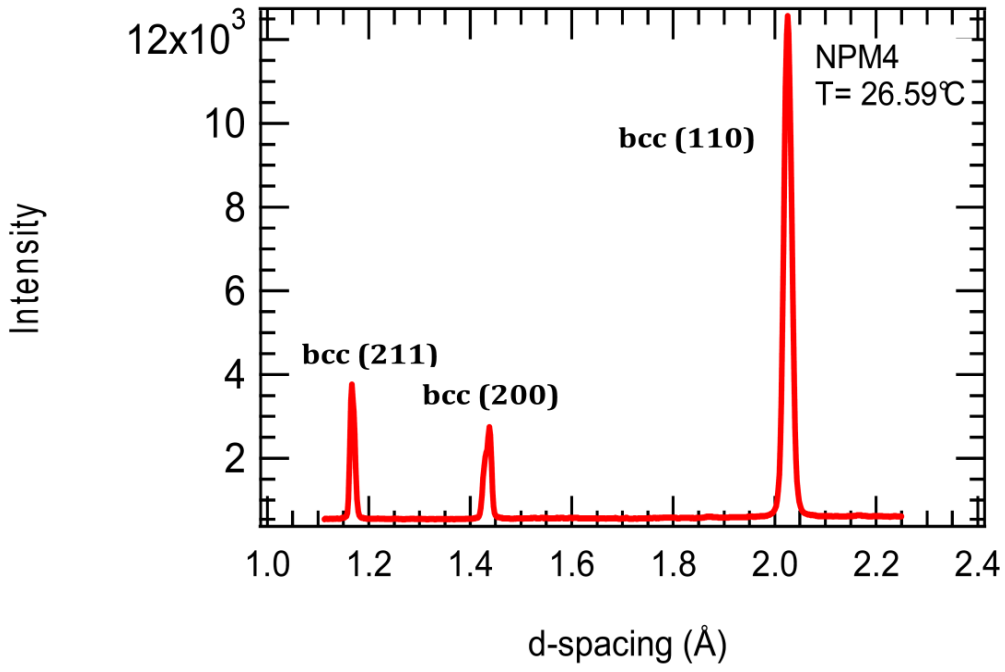


**Figure 61: The resulting X-ray diffraction pattern of the base material of NPM4 with the identified base-centred cubic ferrite peaks.**

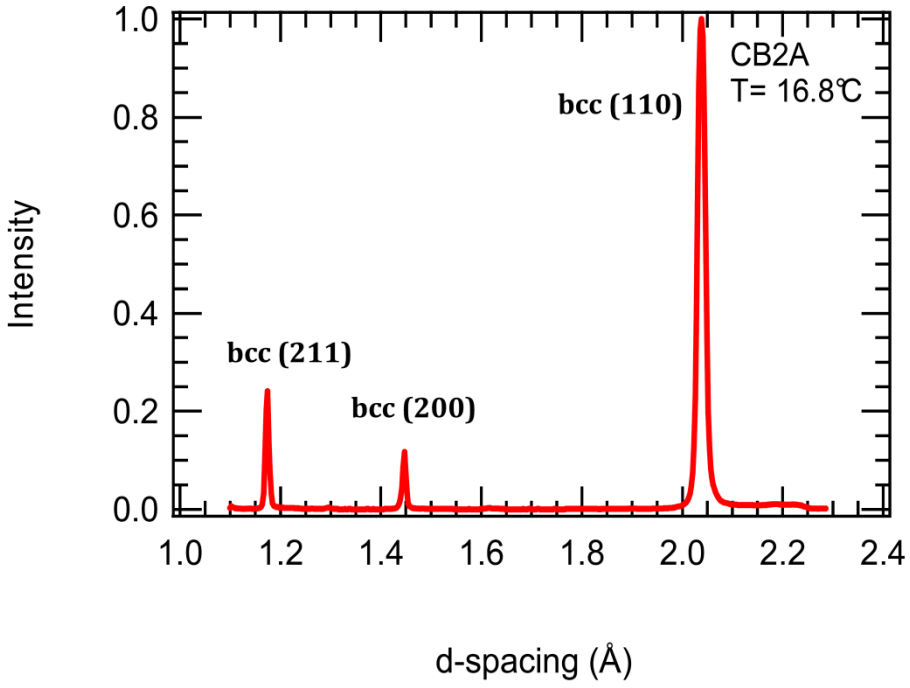


**Figure 62: The resulting X-ray diffraction pattern of the base material of CB2A with the identified base-centred cubic ferrite peaks.**

## Reference pattern of $Cr_{23}C_6$

| 2THETA | D | H | K | L | MULT | I(%) | F | A | B |
|---|---|---|---|---|---|---|---|---|---|
| 3.851 | 6.14878 | 1 | 1 | 1 | 8 | 1.23 | 36.26 | 36.26 | 0 |
| 4.447 | 5.325 | 2 | 0 | 0 | 6 | 0.14 | 16.55 | -16.55 | 0 |
| 6.291 | 3.76534 | 2 | 2 | 0 | 12 | 0.83 | 39.72 | -39.72 | 0 |
| 7.378 | 3.2111 | 3 | 1 | 1 | 24 | 3.16 | 64.23 | 64.23 | 0 |
| 7.706 | 3.07439 | 2 | 2 | 2 | 8 | 2.13 | 95.38 | 95.38 | 0 |
| 8.901 | 2.6625 | 4 | 0 | 0 | 6 | 7.22 | 234.07 | -234.07 | 0 |
| 9.701 | 2.44328 | 3 | 3 | 1 | 24 | 1.54 | 58.97 | -58.97 | 0 |
| 9.954 | 2.38141 | 4 | 2 | 0 | 24 | 35.4 | 289.61 | -289.61 | 0 |
| 10.907 | 2.17392 | 4 | 2 | 2 | 24 | 46.37 | 362.96 | 362.96 | 0 |
| 11.571 | 2.04959 | 3 | 3 | 3 | 8 | 100 | 978.96 | 978.96 | 0 |
| 11.571 | 2.04959 | 5 | 1 | 1 | 24 | 68.11 | 466.44 | 466.44 | 0 |
| 12.6 | 1.88267 | 4 | 4 | 0 | 12 | 38.92 | 542.63 | 542.63 | 0 |
| 13.18 | 1.80018 | 5 | 3 | 1 | 48 | 46.03 | 308.48 | -308.48 | 0 |
| 13.368 | 1.775 | 6 | 0 | 0 | 6 | 18.26 | 557.25 | 557.25 | 0 |
| 13.368 | 1.775 | 4 | 4 | 2 | 24 | 4.34 | 135.83 | 135.83 | 0 |
| 14.095 | 1.68391 | 6 | 2 | 0 | 24 | 3.78 | 133.59 | 133.59 | 0 |
| 14.617 | 1.62411 | 5 | 3 | 3 | 24 | 4.97 | 158.84 | 158.84 | 0 |
| 14.787 | 1.60555 | 6 | 2 | 2 | 24 | 13.16 | 261.36 | -261.36 | 0 |
| 15.448 | 1.5372 | 4 | 4 | 4 | 8 | 0.49 | 90.81 | -90.81 | 0 |
| 15.926 | 1.4913 | 5 | 5 | 1 | 24 | 0 | 5.15 | 5.15 | 0 |
| 15.926 | 1.4913 | 7 | 1 | 1 | 24 | 0.81 | 69.74 | 69.74 | 0 |
| 16.083 | 1.47689 | 6 | 4 | 0 | 24 | 1.16 | 84.21 | 84.21 | 0 |
| 16.694 | 1.42317 | 6 | 4 | 2 | 48 | 0 | 0.09 | -0.09 | 0 |
| 17.139 | 1.38651 | 5 | 5 | 3 | 24 | 0.19 | 36.17 | 36.17 | 0 |
| 17.139 | 1.38651 | 7 | 3 | 1 | 48 | 0.18 | 24.95 | 24.95 | 0 |
| 17.856 | 1.33125 | 8 | 0 | 0 | 6 | 6.99 | 458.58 | 458.58 | 0 |
| 18.273 | 1.3011 | 7 | 3 | 3 | 24 | 0.26 | 45.5 | 45.5 | 0 |
| 18.41 | 1.2915 | 8 | 2 | 0 | 24 | 3.12 | 157.83 | -157.83 | 0 |
| 18.41 | 1.2915 | 6 | 4 | 4 | 24 | 5.98 | 218.45 | -218.45 | 0 |
| 18.949 | 1.25511 | 6 | 6 | 0 | 12 | 24.08 | 637.8 | 637.8 | 0 |
| 18.949 | 1.25511 | 8 | 2 | 2 | 24 | 8.41 | 266.45 | 266.45 | 0 |
| 19.343 | 1.22976 | 7 | 5 | 1 | 48 | 14.45 | 252.02 | 252.02 | 0 |
| 19.343 | 1.22976 | 5 | 5 | 5 | 8 | 5.04 | 364.51 | 364.51 | 0 |
| 19.473 | 1.22164 | 6 | 6 | 2 | 24 | 0.69 | 78.36 | -78.36 | 0 |
| 19.984 | 1.19071 | 8 | 4 | 0 | 24 | 8.38 | 280.22 | -280.22 | 0 |
| 20.359 | 1.16899 | 7 | 5 | 3 | 48 | 4.49 | 147.71 | -147.71 | 0 |
| 20.359 | 1.16899 | 9 | 1 | 1 | 24 | 5.87 | 238.82 | -238.82 | 0 |
| 20.483 | 1.16201 | 8 | 4 | 2 | 48 | 1 | 70.12 | 70.12 | 0 |
| 20.97 | 1.13529 | 6 | 6 | 4 | 24 | 1.28 | 114.76 | 114.76 | 0 |
| 21.329 | 1.11642 | 9 | 3 | 1 | 48 | 4.42 | 153.34 | 153.34 | 0 |
| 21.914 | 1.08696 | 8 | 4 | 4 | 24 | 21.88 | 495.23 | 495.23 | 0 |
| 22.258 | 1.07037 | 7 | 5 | 5 | 24 | 0.15 | 41.41 | 41.41 | 0 |
| 22.258 | 1.07037 | 9 | 3 | 3 | 24 | 10.46 | 347.55 | 347.55 | 0 |

| | | | | | | | | | |
|---|---|---|---|---|---|---|---|---|---|
| 22.258 | 1.07037 | 7 | 7 | 1 | 24 | 0.44 | 71.47 | 71.47 | 0 |
| 22.372 | 1.065 | 8 | 6 | 0 | 24 | 1.27 | 121.91 | -121.91 | 0 |
| 22.372 | 1.065 | 10 | 0 | 0 | 6 | 0.42 | 140.01 | 140.01 | 0 |
| 22.82 | 1.04432 | 8 | 6 | 2 | 48 | 0.12 | 27.48 | -27.48 | 0 |
| 22.82 | 1.04432 | 10 | 2 | 0 | 24 | 0.03 | 18.05 | 18.05 | 0 |
| 23.152 | 1.02957 | 9 | 5 | 1 | 48 | 0.48 | 54.41 | 54.41 | 0 |
| 23.152 | 1.02957 | 7 | 7 | 3 | 24 | 0.03 | 19.9 | 19.9 | 0 |
| 23.261 | 1.0248 | 10 | 2 | 2 | 24 | 0.07 | 29.85 | 29.85 | 0 |
| 23.261 | 1.0248 | 6 | 6 | 6 | 8 | 2.94 | 333.2 | 333.2 | 0 |
| 24.014 | 0.99312 | 9 | 5 | 3 | 48 | 2.16 | 120.28 | -120.28 | 0 |
| 24.12 | 0.98883 | 8 | 6 | 4 | 48 | 0.76 | 71.68 | -71.68 | 0 |
| 24.12 | 0.98883 | 10 | 4 | 0 | 24 | 2.32 | 176.76 | -176.76 | 0 |
| 24.539 | 0.97221 | 10 | 4 | 2 | 48 | 3.2 | 149.34 | 149.34 | 0 |
| 24.848 | 0.96028 | 11 | 1 | 1 | 24 | 2.55 | 190.69 | 190.69 | 0 |
| 24.848 | 0.96028 | 7 | 7 | 5 | 24 | 1.79 | 160.06 | 160.06 | 0 |
| 25.356 | 0.94134 | 8 | 8 | 0 | 12 | 1.56 | 215.07 | 215.07 | 0 |
| 25.657 | 0.93049 | 9 | 7 | 1 | 48 | 2.09 | 125.95 | -125.95 | 0 |
| 25.657 | 0.93049 | 11 | 3 | 1 | 48 | 1.15 | 93.4 | -93.4 | 0 |
| 25.657 | 0.93049 | 9 | 5 | 5 | 24 | 3.47 | 229.7 | -229.7 | 0 |
| 25.756 | 0.92696 | 8 | 8 | 2 | 24 | 0.73 | 105.93 | 105.93 | 0 |
| 25.756 | 0.92696 | 10 | 4 | 4 | 24 | 0.95 | 120.68 | 120.68 | 0 |
| 26.15 | 0.91323 | 10 | 6 | 0 | 24 | 0.8 | 112.47 | 112.47 | 0 |
| 26.15 | 0.91323 | 8 | 6 | 6 | 24 | 0.2 | 55.94 | 55.94 | 0 |
| 26.442 | 0.90332 | 9 | 7 | 3 | 48 | 1.81 | 120.56 | 120.56 | 0 |
| 26.442 | 0.90332 | 11 | 3 | 3 | 24 | 0.09 | 37.74 | 37.74 | 0 |
| 26.539 | 0.90009 | 10 | 6 | 2 | 48 | 1.66 | 115.94 | -115.94 | 0 |
| 26.923 | 0.8875 | 12 | 0 | 0 | 6 | 0.71 | 217.13 | 217.13 | 0 |
| 26.923 | 0.8875 | 8 | 8 | 4 | 24 | 0 | 0.74 | -0.74 | 0 |
| 27.207 | 0.8784 | 11 | 5 | 1 | 48 | 0.88 | 86.31 | 86.31 | 0 |
| 27.207 | 0.8784 | 7 | 7 | 7 | 8 | 0.09 | 68.79 | 68.79 | 0 |
| 27.301 | 0.87542 | 12 | 2 | 0 | 24 | 0.16 | 52.35 | -52.35 | 0 |
| 27.675 | 0.86383 | 10 | 6 | 4 | 48 | 0.14 | 34.47 | 34.47 | 0 |
| 27.675 | 0.86383 | 12 | 2 | 2 | 24 | 0.03 | 21.86 | -21.86 | 0 |
| 27.952 | 0.85543 | 9 | 7 | 5 | 48 | 0.05 | 20.31 | 20.31 | 0 |
| 27.952 | 0.85543 | 11 | 5 | 3 | 48 | 0.03 | 17.56 | -17.56 | 0 |
| 28.409 | 0.84196 | 12 | 4 | 0 | 24 | 4.11 | 275.24 | 275.24 | 0 |
| 28.679 | 0.83417 | 9 | 9 | 1 | 24 | 0.62 | 108.03 | -108.03 | 0 |
| 28.769 | 0.83163 | 12 | 4 | 2 | 48 | 0.76 | 84.8 | -84.8 | 0 |
| 28.769 | 0.83163 | 8 | 8 | 6 | 24 | 1.15 | 147.13 | -147.13 | 0 |
| 28.769 | 0.83163 | 10 | 8 | 0 | 24 | 0.02 | 18.33 | -18.33 | 0 |
| 29.126 | 0.82167 | 10 | 8 | 2 | 48 | 1.99 | 138.74 | 138.74 | 0 |
| 29.39 | 0.81443 | 9 | 9 | 3 | 24 | 7.43 | 382.2 | 382.2 | 0 |
| 29.39 | 0.81443 | 13 | 1 | 1 | 24 | 1.23 | 155.69 | 155.69 | 0 |
| 29.39 | 0.81443 | 11 | 7 | 1 | 48 | 1.86 | 135.09 | 135.09 | 0 |
| 29.39 | 0.81443 | 11 | 5 | 5 | 24 | 1.54 | 173.81 | 173.81 | 0 |
| 29.478 | 0.81205 | 10 | 6 | 6 | 24 | 0 | 5.4 | 5.4 | 0 |
| 29.827 | 0.80277 | 12 | 4 | 4 | 24 | 1.02 | 143.97 | -143.97 | 0 |